

REPORT DOCUMENTATION PAGE						Form Approved OMB No. 0704-0188		
valid OMB control number. PLEASE DO NOT RETURN YOUR FORM TO THE ABOVE ADDRESS.								
1. REPORT DATE (DD-MM-YYYY) 24/07/02		2. REPORT TYPE FINAL TECHNICAL		3. DATES COVERED (From - To) 8/15/97 - 2/14/02				
4. TITLE AND SUBTITLE A New Macro-Micro Approach for Modeling Adaptive Composites				5a. CONTRACT NUMBER				
				5b. GRANT NUMBER F49620-97-1-0419				
				5c. PROGRAM ELEMENT NUMBER				
6. AUTHOR(S) Aditi Chattopadhyay Robert P. Thornburgh				5d. PROJECT NUMBER				
				5e. TASK NUMBER				
				5f. WORK UNIT NUMBER				
7. PERFORMING ORGANIZATION NAME(S) AND ADDRESS(ES) Arizona State University Dept. of Mechanical and Aerospace Engineering Tempe, Arizona 85287-6106				8. PERFORMING ORGANIZATION REPORT NUMBER XAA 0039/TE				
9. SPONSORING / MONITORING AGENCY NAME(S) AND ADDRESS(ES) Air Force Office of Dean Mook Scientific Research 801 North Randolph Street Room 732 Arlington, VA 22203-1977				10. SPONSOR/MONITOR'S ACRONYM(S) AFOSR				
				11. SPONSOR/MONITOR'S REPORT NUMBER(S)				
12. DISTRIBUTION / AVAILABILITY STATEMENT Unlimited								
13. SUPPLEMENTARY NOTES								
14. ABSTRACT The objective of this research was to develop a comprehensive model for accurately and efficiently modeling smart composite structures including the effects of composite damage. First, a new, efficient method for modeling smart structures with piezoelectric devices was developed. The coupled model simultaneously solves for the mechanical and electrical response of the system using mechanical displacements and electrical displacements. The developed theory utilizes a refined higher order displacement field that accurately captures the transverse shear deformation in moderately thick laminates. The model was then extended to include internal damage in the form of delamination and matrix cracking. When delamination is present, the sublaminates are modeled as individual plates and continuity is enforced at the interfaces. Matrix cracking was modeled as a reduction in laminate stiffness using parameters determined using finite element analysis of a representative crack. Finally, the simultaneous optimization of both mechanical and electrical parameters in an adaptive structural system was studied. This study demonstrated how multidisciplinary optimization techniques, such as the Kreisselmeier-Steinhauser function, can be utilized to optimize both structural and electrical aspects of an adaptive structural system. Results have show that the developed model is capable of accurately modeling both the mechanical and electrical response of adaptive structures.								
15. SUBJECT TERMS composites, adaptive structures, piezoelectric actuators, delamination, matrix cracking								
16. SECURITY CLASSIFICATION OF:			17. LIMITATION OF ABSTRACT		18. NUMBER OF PAGES		19a. NAME OF RESPONSIBLE PERSON	
a. REPORT U	b. ABSTRACT U	c. THIS PAGE U	UU		152		Aditi Chattopadhyay	
						19b. TELEPHONE NUMBER (include area code) (480) 965-9342		

ABSTRACT

The development of smart structures technology has coincided with the increased use of composite materials in structural design. Composite laminates have forms of damage that are not found in other materials, specifically delamination and transverse matrix cracking. An in-depth understanding of the effects of damage on smart composite structures is necessary for predicting not only the life of the structure, but also for modeling any method to be used for damage detection. The objective of this research was to develop a comprehensive model for accurately and efficiently modeling smart composite structures including the effects of composite damage.

First, a new, efficient method for modeling smart structures with piezoelectric devices was developed. The coupled model simultaneously solves for the mechanical and electrical response of the system using mechanical displacements and electrical displacements. The developed theory utilizes a refined higher order displacement field that accurately captures the transverse shear deformation in moderately thick laminates.

The model was then extended to include internal damage in the form of delamination and matrix cracking. When delamination is present, the sublaminates are modeled as individual plates and continuity is enforced at the interfaces. Matrix cracking was modeled as a reduction in laminate stiffness using parameters determined using finite element analysis of a representative crack.

Finally, the simultaneous optimization of both mechanical and electrical parameters in an adaptive structural system was studied. This study demonstrates how multidisciplinary optimization techniques, such as the Kreisselmeier-Steinhauser function, can be utilized to optimize both structural and electrical aspects of an adaptive structural system. Optimization of piezoelectric actuator placement and electrical circuitry was performed on passive electrical damping systems.

Results show that the developed model is capable of accurately modeling both the mechanical and electrical response of adaptive structures. These results show that traditional uncoupled piezoelectric modeling techniques do not take into account many electrical effects, resulting in significant errors in the sensor response predicted for transient loads. The developed model provides the ability to predict the effect of composite damage on the behavior of adaptive structures and to model potential methods to be used for damage detection.

TABLE OF CONTENTS

	Page
LIST OF TABLES	x
LIST OF FIGURES	xi
CHAPTER	
1. INTRODUCTION	1
1.1. Piezoelectric materials	2
1.2. Delamination	6
1.3. Matrix cracking.....	8
1.4. Optimization	11
2. OBJECTIVES	13
3. PIEZOELECTRIC ADAPTIVE STRUCTURES MODELING.....	15
3.1. Linear coupled piezoelectric-mechanical theory	16
3.1.1. Constitutive relations	16
3.1.2. Use of material properties.....	20
3.1.3. Equations of motion.....	23
3.1.4. Refined higher order laminate theory	24
3.1.5. Finite element formulation	27
3.1.6. Electrical equations.....	35
3.1.7. Boundary Conditions	37
3.1.8. System reduction	38
3.2. Results and Verification	40
3.2.1. Finite Element Verification	40
3.2.2. Passive Electrical Damping	43

CHAPTER	Page
3.3. Transient Analysis	51
3.3.1. Newton-Raphson Method	52
3.3.2. Results	54
3.3.3. Experimental comparison	64
4. DELAMINATION MODELING IN COMPOSITE LAMINATES.....	75
4.1. Modeling.....	75
4.1.1. Higher Order Theory with Delamination.....	76
4.1.2. Continuity Conditions.....	77
4.1.3. Delamination Crack Tip Singularity.....	79
Dynamic Contact	82
4.2.1. Contact Stiffness	83
4.2.2. Discontinuous Time-Integration Technique	84
4.3. Results	88
5. EFFECT OF MATRIX CRACKING.....	99
5.1. Matrix Crack Modeling	99
5.1.1. Effective Laminate Stiffness.....	100
5.1.2. Finite Element Analysis of a Representative Crack	106
5.2. Bimodularity Effects.....	114
5.3. Results	117
5.3.1. Stiffness Reduction	118
Plate Vibration with Matrix Cracking.....	123

CHAPTER	Page
6. ADAPTIVE STRUCTURE OPTIMIZATION.....	127
6.1. Problem Formulation / Description	128
6.2. Optimization Technique	129
6.3. Results for optimal passive damping systems	132
7. CONCLUDING REMARKS.....	143
REFERENCES.....	145

LIST OF TABLES

Table		Page
3.1	Finite element convergence.....	40
3.2	Stress and displacement comparison for an isotropic simply supported plate	41
3.3	Stress and displacement comparison for an orthotropic plate	42
3.4	Natural frequencies computed using finite element model compared with exact results.....	43
3.5	Material properties from experiments of Hagood and Von Flotow	44
3.6	List of material properties used for transient analysis.....	55
3.7	Material properties for experimental comparison	65
4.1	Properties of carbon-epoxy laminae.....	88
4.2	Comparison of the natural frequencies (Hz) for a delaminated composite plate predicted by the present model with experimental data	89
5.1	Material properties used for matrix cracking comparison.....	118

LIST OF FIGURES

Figure	Page
3.1 Plate geometry and coordinate system	15
3.2 Top view of cantilevered plate with driving and shunted piezoceramic pairs.	44
3.3 Added damping to the first mode of the cantilevered plate for untuned resistance shunting	45
3.4 Analytical strain for first mode actuation of cantilevered plate with shunted piezoceramic pair open, shunted and optimally tuned and damped.	46
3.5 Analytical strain for first mode actuation of cantilevered plate with tuned shunt circuit and varying resistance	47
3.6 Hagood's experimental results for first mode actuation of cantilevered plate with tuned shunt circuit and varying resistance.....	48
3.7 Strain for first mode actuation of the modified cantilevered plate with tuned shunt circuit and varying resistance	48
3.8 Frequency response for aluminum plate with mode 2 damped.....	49
3.9 Two mode damping circuit	50
3.10 Frequency response for aluminum plate with modes 1 and 2 damped	51
3.11 Cantilever plate layout	54
3.12 Tip displacement for $[0^\circ, 90^\circ]_{4s}$ laminate ($L/h=142$) under $1\mu s$ impulse loading.....	55
3.13 Sensor output for $[0^\circ, 90^\circ]_{4s}$ laminate ($L/h=142$) under $1\mu s$ impulse loading	56
3.14 Tip displacement for $[0^\circ, 90^\circ]_{4s}$ laminate ($L/h=142$) under $5\mu s$ impulse loading.....	57
3.15 Sensor output for $[0^\circ, 90^\circ]_{4s}$ laminate ($L/h=142$) under $5\mu s$ impulse loading	58
3.16 Tip displacement for $[0^\circ, 90^\circ]_{4s}$ laminate ($L/h=28.4$) under $1\mu s$ impulse loading	59
3.17 Tip displacement for $[0^\circ, 90^\circ]_{4s}$ laminate under impulse loading	60
3.18 Sensor charge flow for $[0^\circ, 90^\circ]_{4s}$ laminate under impulse loading	61

Figure	Page
3.19 Plate displacement at $t=73.95 \mu s$ during impulse tip loading	61
3.20 Electric displacement at $t=60.45 \mu s$ during impulse loading	62
3.21 Longitudinal strain at the plate surface on both ends of the PZT patch.....	62
3.22 Sensor output for $[0^\circ, 90^\circ]_{4s}$ laminate under impulse loading.....	63
3.23 Experimental setup and plate geometry for transient analysis.....	64
3.24 Input voltage used to simulate impulse loading	66
3.25 Sensor charge flow for input frequencies of (a) 10kHz, (b) 25kHz and (c) 50kHz	69
3.26 Sensor voltage for input frequencies of (a) 1kHz, (b) 10kHz and (c) 25kHz	70
3.27 Predicted response for 10kHz input frequency	71
3.28 Predicted response for 25kHz input frequency	71
3.29 Uncoupled response for 25kHz input frequency.....	72
3.30 Frequency domain comparison between coupled and uncoupled models for 25kHz input frequency	72
3.31 Comparison of classical and higher order plate theories for 25kHz input frequency ..	73
3.32 Predicted response for 1kHz input frequency	73
3.33 Predicted response for 10kHz input frequency	74
4.1 Relationship between the finite element mesh of the sublaminates and the undelaminated regions of the plate.....	76
4.2 Cantilevered beam for crack tip analysis	79
4.3 Deformed shape of the finite element meshes with and without the crack tip singularity	80
4.4 Error from neglect of crack tip singularity.....	81
4.5 Error from neglect of crack tip singularity for varying delamination locations.....	82
4.6 Description of the time domain with jumps in the displacement variable	85

Figure	Page
4.7 Time history for a delaminated plate under free response from a static load.....	91
4.8 Displacement of upper and lower sublaminates for a delaminated $[0^\circ, 90^\circ]_{2s}$ plate under free response.....	91
4.9 First bending and twisting modes for the undelaminated $[0^\circ, 90^\circ]_{2s}$ cantilevered plate	92
4.10 First bending and twisting modes for the $[0^\circ, 90^\circ]_{2s}$ cantilevered plate with 2 in. delamination	92
4.11 Natural frequencies for a cantilevered $[0, 90]_{2s}$ laminate with delamination at varying ply interfaces, $L/h = 125$	94
4.12 Natural frequencies for a cantilevered $[45, -45]_{2s}$ laminate with delamination at varying ply interfaces, $L/h = 125$	94
4.13 Natural frequencies for a cantilevered $[0, 45]_{2s}$ unbalanced laminate with varying delamination locations, $L/h = 125$	94
4.14 Natural frequencies for a cantilevered $[0, 90]_{2s}$ with $L/h = 25$	95
4.15 Displacement of the sublaminates during impulse loading for a plate with a 2 in. delamination at interface 3	95
4.16 Comparison of PZT output voltage during impulse loading for a plate with a 2 in. delamination at interface 3	96
4.17 Displacement of the sublaminates during impulse loading for a $[0^\circ, 90^\circ]_{2s}$ laminate with a 2 in. delamination at interface 2	97
4.18 Comparison of PZT output voltage during impulse loading for a $[0^\circ, 90^\circ]_{2s}$ laminate with a 2 in. delamination at interface 2	98
5.1 Assumed geometry for cracked composite plate.....	100
5.2 Higher order stress distribution on the crack face.....	102

Figure	Page
5.3 Representative matrix crack used to compute damage parameters	107
5.4 Geometry of perpendicular plane used for the finite element analysis	108
5.5 Finite element mesh for representative crack.....	108
5.6 Serendipity (a) and crack tip (b) finite elements used to analyze representative matrix crack	110
5.7 Natural frequency for mode 2 inflection point location for $[0,90_2]_{2s}$ glass-epoxy laminate	115
5.8 Natural frequency for mode 3 inflection point location for $[0,90_2]_{2s}$ glass-epoxy laminate	116
5.9 Stiffness loss of graphite-epoxy $[0,90_2]_s$ laminate	119
5.10 Stiffness loss of glass-epoxy $[0,90_3]_s$ laminate.....	120
5.11 Normalized extensional stiffness of glass-epoxy $[0,90_3]_s$ laminate	121
5.12 Extensional stiffness loss of $[0,\pm 45]_s$ glass-epoxy laminate.	122
5.13 Reduction in shear modulus of $[0,90_2]_s$ graphite-epoxy laminate	123
5.14 Effect of matrix cracking on natural frequencies for a $[0,90_2]_{2s}$ glass-epoxy cantilever plate	124
5.15 Natural frequency of a delaminated graphite-epoxy $[0,90_2]_{2s}$ cantilever plate	125
6.1 Configuration for the cantilevered plate prior to optimization.....	131
6.2 Frequency response curves for a cantilever plate with and without passive damping circuits	133
6.3 Frequency response curve for the optimal passive damping design using mode 1	135
6.4 Frequency response curve for the optimal passive damping design using mode 2	135
6.5 Frequency response curve for the optimal passive damping design using mode 3	136
6.6 Frequency response curve for the optimal passive damping design using mode 4	136

Figure	Page
6.7	Optimized actuator location for passive damping of the first vibration mode137
6.8	Optimized actuator location for passive damping of the second vibration mode137
6.9	Optimized actuator location for passive damping of the third vibration mode138
6.10	Optimized actuator location for passive damping of the fourth vibration mode138
6.11	Position of the actuators on the simply supported plate before and after optimization for two actuators and three modes139
6.12	Frequency response curves for a simply supported plate both undamped and with two actuators140
6.13	Position of the actuators on the simply supported plate before and after optimization for two actuators and three modes, including optimization of ply orientation141
6.14	Frequency response curves for the undamped initial design of a simply supported plate and optimal design including two actuators and optimized ply orientations ..142

1. Introduction

So-called "smart" or "adaptive" structures are structural systems that utilize distributed sensors and actuators in order to monitor or improve structural response. A common use of the smart structures concept is the use of piezoelectric sensors, actuators and a control system in order to control vibration in the structure. This concept can also be used to reduce the noise that is transmitted through a structure. In another application of adaptive structures technology, smart materials are being used to induce shape changes in structures, such as wings or helicopter rotors. This would allow designers to be able to control the lift distribution over a surface and improve aerodynamic efficiency.

The development of smart structures technology has coincided with the increased use of composite materials in structural design. Composite structures are becoming increasingly popular in both aerospace and other systems due to the benefit of reduced weight for given strength and stiffness requirements. However composite laminates have forms of damage that are not found in other materials, specifically delamination and transverse matrix cracking. Both of these forms of damage occur when the composite is subjected to fatigue, over-loading, or low-velocity impact. These forms of damage do not cause catastrophic failure of the structure, but they do affect the way in which it responds to applied loads. Methods are being developed which use smart materials to detect and localize damage within a composite structure. However, limitations in modeling techniques of adaptive structures has caused reliance on empirical data for the development of damage detection methods.

Modeling of smart structures has traditionally been based on simplified models that generally focus only on the aspects that are of interest to a single engineering discipline. Structural models generally treat electronics as "black boxes" and electronics designers generally ignore the structure all together. However, smart structures rely on materials that cross many

engineering disciplines and accurate modeling is not possible unless it includes the interdisciplinary aspects of these materials. In addition, the response of a structure is not constant over time. Environmental changes and structural damage affect the response of a smart structural system. An in-depth understanding of the effects of damage on smart composite structures is necessary for predicting not only the life of the structure, but also for modeling any method to be used for damage detection. If smart materials are to be increasingly used, then significant improvements in modeling must be made so that all of these issues can be addressed. More accurate models will improve the efficiency of the control system, potentially reducing its weight and power consumption.

1.1. Piezoelectric materials

Piezoelectric materials are one of the most commonly used smart materials. Piezoelectric materials create electricity when pressure is applied to them and deform when exposed to an electric field. These two behaviors are known as the direct effect and converse effect, respectively, and each has its own governing equation. There are both ceramic and polymer forms of piezoelectric materials. The most commonly used piezoceramic is lead zirconate titanate (PZT). Piezoceramics can generate moderate forces and have excellent frequency response, but are heavier than most structural materials and are rather brittle. Piezoelectric films, such as Polyvinylidene Fluoride (PVDF), are lightweight and flexible, but can only induce small forces in a structure.

The traditional use of piezoelectric materials in structural applications is to take thin sheets of material and coat each side with an electrically conductive metal electrode. This essentially creates a capacitor with the piezoelectric material acting as a dielectric. When voltage is applied across the electrodes an electric field is created within the piezoelectric material,

inducing deformation. When the piezoelectric material is subjected to mechanical strain, an electric field is induced within the material and an electrical signal is generated. Thus the same device can be used as an actuator or a sensor depending on the electronics connected to it. By either bonding the device to the surface of a structure or embedding it within the structure it is then possible to apply localized forces or measure local strain.

Piezoelectric actuators are often used to control the dynamic response of structures, however the dynamic response of the structure is modified by the addition of these actuators. The PZT or other piezoelectric material adds additional stiffness to the structure, but this stiffness is dependent upon the electrical circuitry attached to each PZT. This can be easily seen in the simple comparison between actuators that are open circuited and ones which are shorted out. Under structural deflection potential energy is stored in the PZT in the form of mechanical strain and also electrical potential similar to a capacitor. When the PZT is shorted out by having its electrodes connected, electrical potential can no longer be stored. This reduction in the systems ability to store energy results in a reduction in the effective stiffness of the system. The magnitude of this reduction is dependent on the piezoelectric material's dielectric permittivity, or capacitance, relative to its piezoelectric properties. In more practical examples this coupling is encountered in the interaction between the structural stiffness and the electrical potential resulting from a combination of mechanical and electrical loading. When piezoelectric constants are experimentally determined the PZT is usually unconstrained. When applied to a structure the PZT is no longer able to deform to its unconstrained shape when a voltage is applied. This change in the strain field causes a reduction in the electrical potential stored in the PZT and, thus, a smaller actuation force than predicted using an uncoupled theory based on the unconstrained piezoelectric constants. For this reason piezoelectric manufacturers often list free and clamped, as well as shorted and open circuited, material properties for PZT. However a PZT mounted to a flexible structure is neither free nor clamped, so arbitrary use of the manufacturer values can lead

to analytic errors during structural modeling. If the piezoelectric-mechanical coupling were to be taken into account then these separate parameters would not be required.

The modeling of piezoelectric materials has been well understood for some time (Tiersten, 1969), but only recently have researcher began to model structures with piezoelectric devices attached to them. Beams with surface bonded actuators were the first to be examined. These beams were modeled using a uniform strain model by Crawley and de Luis (1987), and then with Euler-Bernoulli beam theory by Crawley and Anderson (1989). Twisting of beams using piezoelectric patches was modeled by Park, Walz and Chopra (1996).

A model for anisotropic plates with piezoelectric actuators covering the entire surface was developed by Crawley and Lazarus (1991). Their model used a classical plate theory and Rayleigh-Ritz analysis. Classical plate theory was used by Wang and Rogers (1991) to determine the equivalent force and moment induced by finite-length piezoelectric actuators on composite laminates. A finite element formulation for plates with distributed actuators and sensors was later developed by Detwiler, Shen and Venkayya (1995).

One thing that all of these methods have in common is that they all use an uncoupled approach to solving for the structural response. In an uncoupled approach only one of the governing equations associated with either the direct effect or converse effect is solved. In modeling an actuator, this is made possible by assuming that the electric field in the piezoelectric material is a known constant value. This, of course, leads to two separate models for the structure, depending on whether the piezoelectric patch is being used as an actuator or as a sensor. It also leads to inaccuracies in the results, since the exact transfer of energy between electrical and mechanical is assumed and not solved for.

Although methods using the coupled piezoelectric equations have been known for a long time (Tiersten, 1967, 1969), they have not been used extensively in modeling smart structures. In coupled approaches the mechanical and electrical response (both direct and converse effects) are

simultaneously solved for. This method was first used in the modeling of beams by Hagood, Chung and Flotow (1990). A general two-way coupled theory was introduced in the hybrid plate theory developed by Mitchell and Reddy (1995). In this model a mathematical description of the electric potential was assumed and could be solved for simultaneous with mechanical displacements. This model was extended to a refined higher-order plate theory and coupled to the thermal field by Chattopadhyay, Li and Gu (1999). The description of the electrical potential was then improved by using a third order function of the through-the-thickness coordinate Zhou, Chattopadhyay and Gu (2000). This model allowed for conservation of charge across the PZT and showed the interaction of bending strains with the electrical field within the piezoelectric material. The disadvantage of these models is that additional degrees of freedom are added to the system to describe the distribution of electrical potential (and thus the electric field) within each piezoelectric device. The number of degrees of freedom increases with the PZT area and level of finite element mesh refinement. Also, the resulting system of equations is no longer symmetric positive definite, which adds to the computational time.

A description of the electrical interaction with the structure also allows numerous other applications such as modeling of passive electrical damping systems and self-sensing actuators, as well as analytical determination of power consumption. Passive electrical damping is a technique in which a tuned electrical circuit is used to damp vibration in a structure by dissipating energy as heat in a resistor. Optimal circuit parameters for damping of a particular vibrational mode were determined by Hagood and Flotow (1991). Wu (1996, 1998) has developed an alternate damping circuit and addressed damping of multiple modes. Kahn and Wang (1994) and Tsai and Wang (1996, 1999) have demonstrated combined active-passive control circuits. Others (Agnes, 1994; Hagood and Crawley, 1991) have examined the application of passive damping circuits on real practical structures. Self-sensing actuators have been examined by Anderson and Hagood (1994) using coupled equations similar to those used in this work. By measuring both

voltage and charge flow they have showed that it is possible to simultaneously use a piezoelectric patch as an actuator and a sensor. However, all of these elegant electrical models relied on a comparatively simple description of the strain field in the piezoelectric material and analytical modeling of specific structures contained noticeable errors as a result of the approximations used. If accurate structural models could be coupled with these electrical concepts then very useful and accurate design tools could be developed.

1.2. Delamination

Delamination occurs when a region of composite material becomes debonded from the layers below it. A considerable amount of research effort has been expended in the understanding and modeling of this failure process. However, the vast majority of this work has focused on the initiation and propagation of delamination under static and fatigue loading, and also the effect on the laminate's load carrying capability. Delamination also affects the dynamic characteristics of a composite structure, but these affects are subtler and have been less studied.

A number of investigations into modeling vibration in delaminated composite laminates have been made. Delamination of a composite beam was first modeled by Ramkumar, Kulkarni and Pipes (1979), but their model predicted a severe drop in the natural frequencies which was inconsistent with experimental results. An experimental investigation on the effects of delamination on vibration properties was performed by Lee, Sun and Liu (1987) and Grady and Meyn (1989). Beams were further studied using classical laminate theory, including bending-extension coupling, by a number of other researchers (Wang, et al., 1982; Mujumdar and Suryanarayan, 1988; Tracy and Pardo, 1989; Shen and Grady, 1992). Composite plates have also been modeled, first by Yin and Jane (1988) and later by a number of other authors (Zak, et al., 2000;). Plates with multiple delaminations have been modeled by Ju, et al. (1994) and Wang

and Lin (1995). The effect of local thickening was studied by Hou and Jeronimidis (1999). Most recently, nonlinear vibration was studied by Lu, Lestari and Hanagud (2001).

Most of these methods used classical plate theory, but others have used more complex models. Transverse shear has been included by a number of authors (Kardomateas and Schmueser, 1988; Pavier and Clarke, 1996). Three-dimensional models (Yang and He, 1994) have been shown to provide accurate results, but with computational expense. Layer-wise theories (Barbero and Reddy, 1991) have also been used, but the computational effort can be quite large for thick laminates with a large number of layers. A refined higher order theory was developed by Chattopadhyay and Gu (1994), and it has been shown to be efficient and provide accurate solutions (Chattopadhyay and Gu, 1997, 1999).

The effect of contact between the sublaminates during plate vibration has been ignored in most works. This contact will alter the local response of the structure in the region of the delamination, particularly at high frequencies, as shown by Kwon and Aygunes (1996), but the effect on the global response has not been studied. The contact between the sublaminates makes the response a nonlinear problem. This nonlinearity can be overcome by using time-integration methods. However, the sudden impact of the sublaminates creates oscillations in analytical response that will destabilize most numerical methods. Kwon and Aygunes used the method proposed by Hughes, et al. (1976) which attempts to conserve momentum during the impact. A discontinuous time-integration method proposed by Cho and Kim (1999a,b) has also been used to treat the contact between the sublaminates. This method allows discontinuity to be incorporated into time-integration without having any other constraints enforced on the nodes during contact and release, and it also has been shown to be more stable than other methods.

Delamination modeling in adaptive structures has received surprisingly little attention. Authors studying damage detection have generally relied on experimental results rather than accurate laminate models. Cao, et al. (1998) investigated the effect of piezoelectric actuators on

delamination growth. Delamination modeling and detection using the refined higher order laminate theory has also been studied (Chattopadhyay, Nam and Dragomir-Daescu, 1999; Chattopadhyay and Dragomir-Daescu, 1999). There exists a need for accurate modeling techniques for delaminated composites that includes piezoelectric modeling.

1.3. Matrix cracking

Matrix cracking is a common form of damage in composite laminates and results from a variety of conditions including low-velocity impact, fatigue, and excessive loading. Transverse matrix cracking occurs in a composite with a relatively brittle matrix, such as epoxy. The composite fibers fail at higher strains than the epoxy, so that when the structure is over-loaded or subjected to impact cracks initially form in the matrix. These cracks generally form through the width of each lamina along the fiber direction. Because most of the structural load is carried by the fibers, the cracks in the matrix do not result in catastrophic failure of the structure. However, the matrix cracks do cause a reduction in the overall stiffness of the structure. Matrix cracks can open under load, thus creating an increase in the perceived strains of a laminate and a reduction in the effective stiffness. In engineering design it is often assumed that once matrix cracking has initiated, the lamina with cracks is no longer capable of carrying load. This technique is known as the ply discount method. However, the cracked layer is, in reality, still carrying some of the load, and the reduction in laminate stiffness will be a function of crack density. Being able to accurately describe the changes in structural behavior allows designers to predict the effects of localized damage on static and dynamic characteristics. Also, the modeling of matrix cracking is necessary for the development of smart composite structures capable of detecting damage.

A large amount of research has been conducted on developing models capable of describing the effects of transverse matrix cracking on the stiffness of composite laminates.

Highsmith and his co-authors (1981, 1982) were among the first to examine matrix cracking. They used a shear lag model that assumes that the stresses applied the laminate transfer to the cracked layer from adjacent layers via shear deformation of a thin boundary layer, call the shear transfer region. The model is relatively simple and gives good correlation with experimental data provided the thickness of the shear transfer region can be determined. Unfortunately it is difficult to systematically determine this thickness for an arbitrary laminate. This model was later improved by Lim and Hong (1989), and used to predict shear stiffness by Tsai and Daniel (1992).

Another method for analysis of matrix cracking is the self-consistent scheme utilized by Laws, Dvorak and Hejazi (1983) and Dvorak (1985). This model estimates the degraded stiffness of a single layer with stacked cracks based on the reduction for a body with randomly distributed microcracks or inclusions with identical shape and size. The resulting degraded stiffness components for each layer are then substituted into the laminate model to give the overall laminate stiffness.

Aboudi (1987) has looked at a unit cell representing a laminate with parallel cracks and expanded the displacements using Legendre polynomials. The degraded stiffness was calculated from the elastic energy stored in the cracked body. The disadvantage of this method is that higher order Legendre polynomials are required for good accuracy (Herakovich, et al., 1988).

The principle of minimum complementary energy was used to explicitly calculate ply stresses and the degraded stiffness by Hashin (1985, 1986, 1987). This method is very accurate for laminates with ply stacking sequence of the form $[0_p, 90_q]_s$. However it is very difficult to extend this method to other laminate configurations, because of the cumbersome nature of the complementary strain energy associated with assumed stress functions and traction boundary conditions.

Others have predicted the degraded stiffness using the internal state variable (ISV) concept. This was originally proposed by Vakulenko and Kachanov (1971). Allen et al.

(1987a,b) have used this scheme specifically for transverse matrix cracks. A simple method for determining the ISV was developed by Lee and Allen (1989) for predicting the lower bounds of degraded axial and shear moduli. This method was extended to include damage evolution (Allen et al., 1991, 1997), curved matrix cracks (Allen et al., 1988) and estimate the upper bounds on the degraded stiffness (Allen and Lee, 1990; Lee, et al., 1991). This work was paralleled by Talreja (1985, 1986, 1989, 1992) who used a similar approach in the study of the effects and evolution of matrix cracks.

Another modeling method using damage mechanics to describe the reduction in laminate stiffness was developed by Gudmundson and Ostlund (1992) and improved by Gudmundson and Zang (1993). In this method the reduction in stiffness is calculated based closed form fracture mechanics solutions for uniform distributions of cracks. In order to apply closed form solutions it is assumed that the cracks are in an infinite homogeneous medium. This method gives reasonable results, but the accuracy is dependent upon the specific laminate material and lay-up. This method was extended to address the effect on bending stiffness by Adolfsson and Gudmundson (1997). This is noteworthy since most models are applicable only to pure extension, and only a few address the changes in matrix crack behavior under bending loads (Makins and Adali, 1991; Smith and Ogin, 1999). This method can also estimate the reduction in transverse shear stiffness.

Less work has been reported on applying the available models to actual structures and addressing the complications created by crack closure. Kim, Atluri and Loewy (1998) have looked at the effects of matrix cracking on flutter for composite plates. Crack closure is of particular concern for plates under bending where cracks will open and close depending upon the deformed shape. Under compression the matrix cracks will close, creating a change in laminate stiffness. This essentially results in a bimodular material with different stiffness for tension and compression. Bimodularity is a phenomenon not exclusive to matrix cracking. Many materials such as kevlar-rubber composites exhibit this behavior and the vibration of bimodular plates has

been well studied (Bert, et al., 1981; Reddy, 1982; Wu, Jing and Cheng, 1989; Tseng and Bai, 1993). This work makes use of some of these bimodular methods in the study of plates with matrix cracks.

1.4. Optimization

Once one is able to model a system, such as an adaptive structural system, the next logical consideration is how to optimize that system for maximum performance. Optimization of adaptive structures is a popular area of study, but only a limited amount of work has been done on simultaneously optimizing both structural and electrical aspects of a system. A common application of the electrical interaction with the structural deformation is in the design of passive electrical damping systems. The work by Hagood and Flotow (1991) and Wu (1996, 1998) has addressed optimal electrical parameters for passive damping circuits. Research by Tsai and Wang (1996) has made use of optimization techniques to choose electrical parameters in order to maximize control authority.

However, in all of these works, although significant effort was made in addressing the electrical aspects of the damping systems, very simple structural models were used that do not take into account the complex state of strain that may exist in the piezoelectric patches. In addition, the placement of the piezoelectric patch has not been considered concurrently with the design of the electrical system. Much of the work available in the literature has addressed the vibration of cantilevered beams and plates where a piezoelectric patch located near the root can be effective in controlling all of the lower order modes. Structures with other boundary conditions, where optimal location varies for each mode and are not intuitively obvious have not been examined in detail.

In this work it is demonstrated how multidisciplinary optimization (MDO) techniques can be utilized to optimize both structural and electrical aspects of an adaptive structural system. To simultaneously optimize multiple performance requirements, the Kreisselmeier-Steinhauser (K-S) function approach (Wren, 1989; Sethi and Striz, 1997) is used. The K-S technique is a multiobjective optimization procedure that combines all the objective functions and the constraints to form a single unconstrained composite function to be minimized. Then an unconstrained solver is used to locate the minimum of the composite function. The advantage of this method is that it does not rely on arbitrary weight factors to combine multiple objective functions although they can be used in cases where a designer wishes to emphasize specific design criteria (Rajadas, Jury and Chattopadhyay, 2000).

Optimization of an integrated structural and electrical system involves both discrete and continuous variables. Gradient based methods are generally ineffective in the optimization of discrete variables and nongradient based techniques such as genetic algorithms (GA) and simulated annealing (SA) can be computationally very expensive (Belegundu and Chandrupatla, 1999). A hybrid method (Seeley, Chattopadhyay and Brei, 1996) has been developed that uses a discrete search combined with a gradient based technique for the continuous design variables. The use of this technique provides significant improvement in computational efficiency over traditional discrete searches by using a combinatorial search algorithm that allows the use of gradients for the continuous variables, while using a discrete search technique for the discrete design variables. The optimization method used in this work is very similar to the hybrid method of Seeley, with the major difference being that the discrete search and the gradient based search are more independent due to the nature of this particular problem. Since, the present model assumes that only the electrical components to be continuous parameters the gradient based search essentially amounts to finding the optimal set of electrical components for a give structural configuration.

2. Objectives

The overall objective of this research is to develop a comprehensive model for accurately and efficiently modeling smart composite structures for practical aerospace applications under a variety of loads and environmental conditions. First a new, efficient method for modeling smart structures with piezoelectric devices is developed. The coupled model simultaneously solves for the mechanical and electrical response of the system using mechanical displacements and electrical displacements. The developed theory utilizes a refined higher order displacement field that accurately captures the transverse shear deformation in moderately thick laminates. The model is validated using a combination of experimental data and solutions to known problems.

The model is then extended to include internal damage in the form of delamination and matrix cracking. When delamination is present the sublaminae are modeled as individual plates and continuity reinforced at the interfaces. Matrix cracking is modeled as a reduction in laminate stiffness using parameters determined using finite element analysis of a representative crack. The developed approach is then correlated with experimental results. The effect of damage on the response of a smart structural system is then examined.

Finally, the simultaneous optimization of both mechanical and electrical parameters in an adaptive structural system is studied. The objective of this work is to demonstrate how multidisciplinary optimization (MDO) techniques can be utilized to optimize both structural and electrical aspects of an adaptive structural system. To simultaneously optimize multiple performance requirements, the Kreisselmeier-Steinhauser (K-S) function approach is used. Optimization of piezoelectric actuator placement and electrical circuitry is performed on passive electrical damping systems.

The following are the principle objectives for this research.

1. Development of an efficient coupled model for simultaneous modeling of mechanical and electrical response in an adaptive structural system.
2. Development of a unified method for modeling the effects of delamination on the static and dynamic response of smart composite structures.
3. Development of a model for predicting the reduction in plate stiffness caused by transverse matrix cracking, and a method for describing its effects on the structural response of smart composites.
4. Analysis of the effects of combined damage on smart structural response (both static and dynamic) using the developed procedure.
5. Demonstrate the use of optimization techniques in the simultaneous optimization of mechanical and electrical components in a smart structural system.

3. Piezoelectric adaptive structures modeling

In this chapter a coupled piezoelectric-mechanical model is developed in order to accurately and efficiently model both the mechanical and electric response of an adaptive structural system. Unlike other techniques that solve only one of the coupled piezoelectric equations, the developed model simultaneously solves both of the coupled equations. This ensures that the model accurately describes the transfer of energy between mechanical and electrical and that the model will be applicable regardless of whether the piezoelectric device is being used as a sensor or actuator. Unlike other models, the developed theory ensures conservation of charge and accurately predicts the electrical response of the system. Since the electrical response of the system is considered, any system using piezoelectric materials can be modeled other than just the tradition sensor and actuator applications. These systems include passive electrical damping circuits and self-sensing actuators.

A less frequently used form of the coupled constitutive relations is shown to be advantageous for analysis for adaptive structures and is used to develop a linear model. A refined higher order laminate theory is used to model the mechanical displacement field, thus making the model capable of capturing the effects of transverse shear in moderately thick laminate constructions. Additional equations are then included to model the attached electrical circuitry. The resulting model is verified using experimental data, and the importance of solving the coupled system is illustrated in the transient analysis of adaptive structural systems.

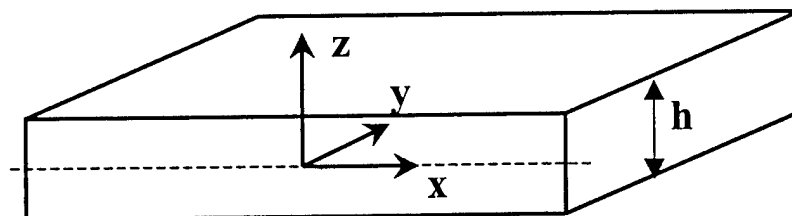


Fig. 3.1. Plate geometry and coordinate system.

3.1. Linear coupled piezoelectric-mechanical theory

The model developed in this section is based on solving the response for a laminated composite plate with embedded or surface bonded actuators. A two-dimension plate theory is used for computational efficiency. The plate geometry is illustrated in Figure 3.1. The global x- and y- coordinates are assumed to be oriented in the plane of the plate, and the z- axis is perpendicular to the plane of the plate. The plate is a composite laminate composed of orthotropic laminae. The material 1- and 2- axes are assumed to be parallel to the plane of the plate, and the material 3- axis is oriented parallel with the global z- axis.

3.1.1. Constitutive relations

The construction of a model for smart composite laminates starts with the formulation of the constitutive relations (IEEE, 1987). Traditionally these are expressed as a function of the components of strain (S_{ij}) and electric field (E_i) as follows

$$T_{ij} = c_{ijkl}^E S_{kl} - e_{kij} E_k \quad (3.1)$$

$$D_i = e_{ikl} S_{kl} + \chi_{ik}^S E_k \quad (3.2)$$

where T_{ij} is the stress tensor, D_i is the electric displacement, and c_{ijkl}^E , e_{kij} and χ_{ik}^S are elastic, piezoelectric and dielectric constants for the material. The superscript, E , in the elastic constant reflects that the elastic constants used are those measured in the absence of any electric field within the piezoelectric material. Likewise, the superscript, S , in the dielectric constant represents those constants measured while the piezoelectric material is subjected to zero strain. The electric field is generally thought of as being derived from the gradient of a scalar electric potential, ϕ as follows

$$E_i = -\phi_{,i} \quad (3.3)$$

When piezoelectric materials are used in adaptive structural systems they are usually in the form of relatively thin layers that are either embedded in or bonded to the surface of the host structure. The upper and lower surfaces are usually each covered with an electrically conducting electrode in order to apply or sense changes in voltage, while the sides generally remain unelectroded. Based on this typical configuration structural modeling has traditionally uncoupled the constitutive relations by assuming that the electric field through the thickness of the piezoelectric device is directly proportional to the voltage on the electrodes divided by the material thickness. Having made this assumption, Eq. (3.1) can directly solved for in order to predict the response of the structure in the presence of an applied voltage. This has often been referred to as the converse effect. In a similar manner, Eq. (3.2), known as the direct effect, can be directly solved for in order to give the charge flow into or out of the piezoelectric device in the presence of an applied strain. This allows the piezoelectric sensor to give an estimate of the local strain in the host structure.

While the uncoupled approximation gives convenient estimates concerning the response of an adaptive structural system, it ignores some key physical principles of piezoelectric materials. First, the uncoupled approach ignores the nature in which energy is transformed from electric to mechanical and vice versa. When a voltage is applied to the electrodes of an actuator, an electric field is induced which in turns creates strain in the host structure. However, the strain in the piezoelectric material also influences the electric field, as shown in Eq. (3.2). Thus, the electric field in the actuator is dependent on the stiffness of the host structure, which is not captured by the uncoupled assumptions.

Another aspect not addressed by the uncoupled approach is conservation of charge. Physics requires that the electric displacement vector, D_i , satisfy the electric equation for an insulator

$$D_{i,i} = 0 \quad (3.4)$$

This equation is simply a mathematical representation of the conservation of charge within the material. For the case of the piezoelectric device with electrodes on the upper and lower surfaces, it implies that the electric displacement be constant through the thickness of the device. This is very important, in that Eq. (3.2) now shows that when the strain varies through the thickness, such as during plate bending, then the electric field must also vary through the thickness in order to maintain constant electric displacement. This also implies that the uncoupled modeling approach results in differing amounts of charge on the upper and lower electrodes, which is a violation of the conservation of charge principle. This has been resolved by some authors by solving the coupled equations, but making the electric potential, and in turn the electric field, higher order functions of the through the thickness coordinate to match the displacement and strain fields in the structure. However, such an approach can lead to numerous additional degrees of freedom to describe the electric potential. Another drawback of such an approach is that the resulting system matrices in finite element implementation are not symmetric. This results in a sizable increase in the computational effort required to solve the system of equations when compared to the original host structure whose finite element equations result in a symmetric positive definite system.

Equations (3.1) and (3.2) are not the only way to describe a piezoelectric material. The following forms are all equally valid

$$T_{ij} = c^D_{ijkl} S_{kl} - h_{kij} D_k \quad (3.5a)$$

$$E_i = -h_{ikl} S_{kl} + \beta^S_{ik} D_k \quad (3.5b)$$

or

$$S_{ij} = s^E_{ijkl} T_{kl} + d_{kij} E_k \quad (3.6a)$$

$$D_i = d_{ikl} T_{kl} + \chi^T_{ik} E_k \quad (3.6b)$$

or

$$S_{ij} = s^D_{ijkl} T_{kl} + g_{kij} D_k \quad (3.7a)$$

$$E_i = -g_{ikl} T_{kl} + \beta^T_{ik} D_k \quad (3.7b)$$

While each form of the coupled piezoelectric equations has advantages in certain cases, the form using the mechanical strain and the electric displacement, Eqs. (3.5a, 3.5b), are best suited to adaptive structural modeling. The reason for this is that standard finite element solutions for the mechanical response of structures utilize displacements to provide strain, and specifying electric displacement as an in-plane variable inherently satisfies conservation of charge. Also, the resulting system of equations is symmetric allowing for improved computational efficiency. It is also worth noting that when the piezoelectric device is used as an actuator, the applied voltage is introduced in a manner very similar to how external forces and pressures are applied to the structure.

The constitutive relations can be expressed in matrix form as

$$\sigma = c^D \varepsilon - h^T D \quad (3.8a)$$

$$E = -h \varepsilon + \beta^S D \quad (3.8b)$$

where the stress and strain have been expressed as follows

$$\sigma = \begin{Bmatrix} \sigma_1 \\ \sigma_2 \\ \sigma_3 \\ \sigma_4 \\ \sigma_5 \\ \sigma_6 \end{Bmatrix} = \begin{Bmatrix} T_{11} \\ T_{22} \\ T_{33} \\ T_{23} \\ T_{31} \\ T_{12} \end{Bmatrix} \quad (3.9)$$

$$\varepsilon = \begin{Bmatrix} \varepsilon_1 \\ \varepsilon_2 \\ \varepsilon_3 \\ \varepsilon_4 \\ \varepsilon_5 \\ \varepsilon_6 \end{Bmatrix} = \begin{Bmatrix} S_{11} \\ S_{22} \\ S_{33} \\ 2S_{23} \\ 2S_{31} \\ 2S_{12} \end{Bmatrix} \quad (3.10)$$

The nature of the matrices formed by the elastic, piezoelectric and dielectric constants is very much dependent on nature and orientation of the piezoelectric crystal. Structural analysis is simplified by the assuming that the piezoelectric device possesses a minimum amount of symmetry, making it at least orthorhombic. This means that the material is assumed to have three mutually perpendicular crystal axes with the polar axis oriented in the out-of-plane direction. This assumption is not very restrictive, in that almost all piezoelectric patches used in adaptive structural systems fall in this category. It also assumed that the entire upper and lower surfaces are covered by perfectly conducting electrodes and that the sides are unelectroded. This is the typical configuration for piezoelectric devices and results in the requirement that the in-plane components of the electric displacement be uniformly zero at all locations.

$$\mathbf{D}_1 = \mathbf{D}_2 = 0 \quad (3.11)$$

3.1.2. Use of material properties

The components of the elastic, piezoelectric and dielectric matrices must be derived from experimental data. Although the matrices in Eqs. (3.8a,b) can be measured directly, the values usually measured and provided by manufacturers are the independent constants that make up the components the form of the constitutive relations from Eqs. (3.6a,b). In matrix form these equations are expressed as

$$\varepsilon = \mathbf{s}^E \sigma + \mathbf{d}^T \mathbf{E} \quad (3.12a)$$

$$\mathbf{D} = \mathbf{d}\sigma + \chi^T \mathbf{E} \quad (3.12b)$$

As a result of the orthorhombic assumption the elastic, piezoelectric and dielectric matrices take the forms

$$\mathbf{s}^E = \begin{bmatrix} \frac{1}{Y_1^E} & \frac{-\nu_{12}^E}{Y_2^E} & \frac{-\nu_{12}^E}{Y_3^E} & 0 & 0 & 0 \\ \frac{-\nu_{12}^E}{Y_1^E} & \frac{1}{Y_2^E} & \frac{-\nu_{12}^E}{Y_3^E} & 0 & 0 & 0 \\ \frac{-\nu_{12}^E}{Y_1^E} & \frac{-\nu_{12}^E}{Y_2^E} & \frac{1}{Y_3^E} & 0 & 0 & 0 \\ 0 & 0 & 0 & \frac{1}{G_{23}^E} & 0 & 0 \\ 0 & 0 & 0 & 0 & \frac{1}{G_{31}^E} & 0 \\ 0 & 0 & 0 & 0 & 0 & \frac{1}{G_{12}^E} \end{bmatrix} \quad (3.13)$$

$$\mathbf{d} = \begin{bmatrix} 0 & 0 & 0 & 0 & d_{15} & 0 \\ 0 & 0 & 0 & d_{24} & 0 & 0 \\ d_{31} & d_{32} & d_{33} & 0 & 0 & 0 \end{bmatrix} \quad (3.14)$$

$$\chi = \begin{bmatrix} \chi_{11} & 0 & 0 \\ 0 & \chi_{22} & 0 \\ 0 & 0 & \chi_{33} \end{bmatrix} \quad (3.15)$$

and all of the unknown coefficients are those typically determined from experimental data. Thus, in order to determine the matrix coefficients in the form of the equations expressed in Eqs. (3.8a,b) a transformation is required. This aspect of piezoelectric materials is often not discussed by authors, but is extremely important in order develop an accurate set of system matrices. The transformation is complicated by the fact that most two-dimensional structural models make the assumption of plane stress. The refined higher order laminate theory discussed later in this work also results in the out-of-plane stress being zero, or

$$\sigma_3 = 0 \quad (3.16)$$

It is very important to properly address this since the piezoelectric coefficient, d_{33} , is typically very large. Ignoring the effect of Eq. (3.16) on the piezoelectric behavior will result in material coefficients that are very inaccurate. Correct transformation of results in the following equations for determining the coefficients for the matrices in Eqs. (3.8a,b) from the typical material properties available.

$$c_{11}^D = \frac{Y_1^E (\chi_{33}^T - Y_2^E d_{32}^2)}{\Delta} \quad (3.17a)$$

$$c_{22}^D = \frac{Y_2^E (\chi_{33}^T - Y_1^E d_{31}^2)}{\Delta} \quad (3.17b)$$

$$c_{12}^D = \frac{Y_1^E (Y_2^E d_{31} d_{32} + \nu_{21}^E \chi_{33}^T)}{\Delta} \quad (3.17c)$$

$$c_{21}^D = \frac{Y_2^E (Y_1^E d_{31} d_{32} + \nu_{12}^E \chi_{33}^T)}{\Delta} = c_{12}^D \quad (3.17d)$$

$$c_{44}^D = \frac{G_{23}^E \chi_{22}^T}{\chi_{22}^T - d_{24}^2 G_{23}^E} \quad (3.17e)$$

$$c_{55}^D = \frac{G_{31}^E \chi_{11}^T}{\chi_{11}^T - d_{15}^2 G_{31}^E} \quad (3.17f)$$

$$c_{66}^D = G_{12}^E \quad (3.17g)$$

$$\beta_{11}^S = \frac{1}{\chi_{11}^T - d_{15}^2 G_{31}^E} \quad (3.18a)$$

$$\beta_{22}^S = \frac{1}{\chi_{22}^T - d_{24}^2 G_{23}^E} \quad (3.18b)$$

$$\beta_{33}^S = \frac{1 - \nu_{12}^E \nu_{21}^E}{\Delta} \quad (3.18c)$$

$$h_{31} = \frac{Y_1^E (\nu_{21}^E d_{32} + d_{31})}{\Delta} \quad (3.19a)$$

$$\mathbf{h}_{32} = \frac{Y_2^E (\nu_{11}^E d_{31} + d_{32})}{\Delta} \quad (3.19b)$$

$$\mathbf{h}_{15} = \frac{d_{15} G_{31}^E}{\chi_{11}^T - d_{15}^2 G_{31}^E} \quad (3.19c)$$

$$\mathbf{h}_{24} = \frac{d_{24} G_{23}^E}{\chi_{22}^T - d_{24}^2 G_{23}^E} \quad (3.19d)$$

where

$$\Delta = \chi_{33}^T (1 - \nu_{12}^E \nu_{21}^E) - Y_1^E d_{31}^2 - Y_2^E d_{32}^2 - \nu_{12}^E d_{31} d_{32} Y_2^E - \nu_{21}^E d_{31} d_{32} Y_1^E \quad (3.20)$$

All other coefficients are zero or are not used by the refined higher order laminate theory.

3.1.3. Equations of motion

The conservation of energy within piezoelectric material is described by the electric enthalpy, which is typically expressed in terms of strain and electric field as

$$H = \frac{1}{2} c_{ijkl}^E S_{ij} S_{kl} - e_{kij} E_k S_{ij} - \frac{1}{2} \chi_{ij}^S E_i E_j \quad (3.21)$$

Note that this is different from the total potential energy, which is

$$U = \frac{1}{2} c_{ijkl}^E S_{ij} S_{kl} + \frac{1}{2} \chi_{ij}^S E_i E_j \quad (3.22)$$

Since the formulation used in this work is based on strain and electric displacement, an alternate form of the electric enthalpy must be used

$$H = \frac{1}{2} c_{ijkl}^D S_{ij} S_{kl} - h_{kij} D_k S_{ij} + \frac{1}{2} \beta_{ij}^S D_i D_j \quad (3.23)$$

or in matrix form

$$\mathbf{H}(\boldsymbol{\varepsilon}, \mathbf{D}) = \frac{1}{2} \boldsymbol{\varepsilon}^T \mathbf{c}^D \boldsymbol{\varepsilon} - \mathbf{D}^T \mathbf{h} \boldsymbol{\varepsilon} + \frac{1}{2} \mathbf{D}^T \boldsymbol{\beta}^S \mathbf{D} \quad (3.24)$$

The equations of motion can be formulated using a variational approach and Hamilton's Principle in a manner similar to that proposed by Tiersten (1967). The variational principle between times t_0 and t , for the piezoelectric body of volume V can be written as follows

$$\delta\Pi = 0 = \int_{t_0}^t \int_V \left[\delta \left(\frac{1}{2} \rho \dot{\mathbf{u}}^T \dot{\mathbf{u}} \right) - \delta \mathbf{H}(\boldsymbol{\varepsilon}, \mathbf{D}) \right] dV dt + \int_{t_0}^t \delta \mathbf{W} dt \quad (3.25)$$

where the first term represents the kinetic energy, the second term the electric enthalpy and $\delta \mathbf{W}$ is the total virtual work done on the structure. The terms \mathbf{u} and ρ correspond to the mechanical displacement and density, respectively. The work done by body forces (\mathbf{f}_B), surface tractions (\mathbf{f}_S) and electrical potential (ϕ) applied to the surface of the piezoelectric material can be expressed by

$$\delta \mathbf{W} = \int_V \delta \mathbf{u}^T \mathbf{f}_B dV + \int_S \delta \mathbf{u}^T \mathbf{f}_S dS + \int_S \delta \mathbf{D}^T \phi dS \quad (3.26)$$

Equations (3.24-26) provide the equations of motion for the piezoelectric body. To solve them, the assumptions about the properties and orientation of the piezoelectric device described in the previous sections are utilized to simplify the system.

3.1.4. Refined higher order laminate theory

A refined higher order laminate theory, originally developed by Reddy (1984, 1997), is used to model the mechanical displacement field. The refined higher order theory assumes a parabolic distribution of transverse shear strain, thus providing accurate estimation of transverse shear stresses for moderately thick constructions with little increase in computational effort. This makes the higher order theory more accurate than the classical plate theory, which neglects the presence of transverse shear, and more convenient than the first order shear deformation theory, which requires a shear correction factor to be known.

The laminate is assumed to be a plate structure composed of an arbitrary number of orthotropic lamina arranged with varying orientations. The coordinate system for the plate is

taken to be with the x-y plane parallel to the plane of the plate and the z coordinate normal to the plane of the plate measured from the center of thickness. The theory starts with a general, third order displacement field as follows

$$\mathbf{u}_1 = u + z\psi_{x1} + z^2\psi_{x2} + z^3\psi_{x3} \quad (3.27a)$$

$$\mathbf{u}_2 = v + z\psi_{y1} + z^2\psi_{y2} + z^3\psi_{y3} \quad (3.27b)$$

$$\mathbf{u}_3 = w \quad (3.27c)$$

The variable z represents the location with respect to the midplane of the plate, and h is the total plate thickness. This displacement field is then simplified by imposing the stress free boundary conditions on the free surfaces.

$$\sigma_4\left(\pm\frac{h}{2}\right) = \sigma_5\left(\pm\frac{h}{2}\right) = 0 \quad (3.28)$$

Since the laminate is orthotropic, this implies that the transverse shear strains are zero on the upper and lower surfaces of the laminate.

$$\varepsilon_4\left(\pm\frac{h}{2}\right) = \frac{\partial \mathbf{u}_2}{\partial z}\left(\pm\frac{h}{2}\right) + \frac{\partial \mathbf{u}_3}{\partial y}\left(\pm\frac{h}{2}\right) = 0 \quad (3.29a)$$

$$\varepsilon_5\left(\pm\frac{h}{2}\right) = \frac{\partial \mathbf{u}_1}{\partial z}\left(\pm\frac{h}{2}\right) + \frac{\partial \mathbf{u}_3}{\partial x}\left(\pm\frac{h}{2}\right) = 0 \quad (3.29b)$$

Thus, substituting Eqs. (3.27a-c) into Eqs. (3.29a,b) yields the following

$$\psi_{x2} = \psi_{y2} = 0 \quad (3.30a)$$

$$\psi_{x3} = \frac{-4}{3h^2}\left(\psi_{x1} + \frac{\partial w}{\partial x}\right) \quad (3.30b)$$

$$\psi_{y3} = \frac{-4}{3h^2}\left(\psi_{y1} + \frac{\partial w}{\partial y}\right) \quad (3.30c)$$

In order to simplify the resulting equation the following change of variables is made

$$\psi_x = \psi_{x1} + \frac{\partial w}{\partial x} \quad (3.31a)$$

$$\psi_y = \psi_{y1} + \frac{\partial w}{\partial y} \quad (3.31b)$$

The refined displacement field now takes the following form

$$\mathbf{u}_1 = u + z \left(\psi_x - \frac{\partial w}{\partial x} \right) - \frac{4z^3}{3h^2} \psi_x \quad (3.32a)$$

$$\mathbf{u}_2 = v + z \left(\psi_y - \frac{\partial w}{\partial y} \right) - \frac{4z^3}{3h^2} \psi_y \quad (3.32b)$$

$$\mathbf{u}_3 = w \quad (3.32c)$$

where u , v , and w are the displacements of the midplane and ψ_x and ψ_y are the rotations of the normal at $z=0$ about the $-y$ and $-x$ axes, respectively. Note that u , v , w , ψ_x and ψ_y are all functions of the x and y coordinates only. The coupled piezoelectric-mechanical theory can easily be developed using other plate theories, but the chosen plate model affects the constraints imposed on the delamination boundaries developed later in this paper. The ψ_x and ψ_y values can be thought of as quantifying the amount of transverse shear present in the laminate, and if they are assumed to be zero the classical plate theory is obtained.

The linear form of the strains are then determined by differentiating the displacements, resulting in the following relations

$$\epsilon_{1L} = \frac{\partial \mathbf{u}_1}{\partial x} = \frac{\partial u}{\partial x} + z \left(\frac{\partial \psi_x}{\partial x} - \frac{\partial^2 w}{\partial x^2} \right) - \frac{4z^3}{3h^2} \frac{\partial \psi_x}{\partial x} \quad (3.33a)$$

$$\epsilon_{2L} = \frac{\partial \mathbf{u}_2}{\partial y} = \frac{\partial v}{\partial y} + z \left(\frac{\partial \psi_y}{\partial y} - \frac{\partial^2 w}{\partial y^2} \right) - \frac{4z^3}{3h^2} \frac{\partial \psi_y}{\partial y} \quad (3.33b)$$

$$\epsilon_{3L} = \frac{\partial \mathbf{u}_3}{\partial z} = 0 \quad (3.33c)$$

$$\epsilon_{4L} = \frac{\partial \mathbf{u}_2}{\partial z} + \frac{\partial \mathbf{u}_3}{\partial y} = \psi_y - \frac{4z^2}{h^2} \psi_y \quad (3.33d)$$

$$\epsilon_{5L} = \frac{\partial \mathbf{u}_1}{\partial z} + \frac{\partial \mathbf{u}_3}{\partial x} = \psi_x - \frac{4z^2}{h^2} \psi_x \quad (3.33e)$$

$$\epsilon_{6L} = \frac{\partial \mathbf{u}_1}{\partial y} + \frac{\partial \mathbf{u}_2}{\partial x} = \frac{\partial u}{\partial y} + \frac{\partial v}{\partial x} + z \left(\frac{\partial \psi_x}{\partial y} + \frac{\partial \psi_y}{\partial x} - 2 \frac{\partial^2 w}{\partial x \partial y} \right) - \frac{4z^3}{3h^2} \left(\frac{\partial \psi_x}{\partial y} + \frac{\partial \psi_y}{\partial x} \right) \quad (3.33f)$$

3.1.5. Finite element formulation

To solve the equations of motion for the coupled system a finite element solution method is used. This method is chosen in order to allow relatively easy modeling of a variety of structural geometries. Since the coupled approach that is being used solves for both mechanical and electric aspects of the coupled system, the finite element method used to solve these equations must address both the mechanical and electric variables in order to be effective.

3.1.5.1 Mechanical relations

By using the refined higher order displacement field, the equations of motion can be simplified by the reduction of the mechanical displacements and strains to the variables u , v , w , ψ_x and ψ_y . The displacement vector, \mathbf{u} , can be written as follows

$$\mathbf{u} = \begin{Bmatrix} \mathbf{u}_1 \\ \mathbf{u}_2 \\ \mathbf{u}_3 \end{Bmatrix} = \mathbf{B}_u \mathbf{u}_{u1} \quad (3.34)$$

where

$$\mathbf{u}_{u1} = \left[u \quad \psi_x \quad v \quad \psi_y \quad w \quad \frac{\partial w}{\partial x} \quad \frac{\partial w}{\partial y} \right]^T \quad (3.35)$$

$$\mathbf{B}_u = \begin{bmatrix} 1 & z - \frac{4z^3}{3h^2} & 0 & 0 & 0 & -z & 0 \\ 0 & 0 & 1 & z - \frac{4z^3}{3h^2} & 0 & 0 & -z \\ 0 & 0 & 0 & 0 & 1 & 0 & 0 \end{bmatrix} \quad (3.36)$$

Since the laminae in the plate are all assumed to be orthotropic the in-plane strains and the transverse shear strains can be decoupled and treated independently from one another. As a result of the plane stress assumption, the out-of-plane strain, ϵ_3 , is ignored. This simplifies the assembly process slightly and gives two separate strain vectors. The in-plane linear strain vector, ϵ_{iL} , and the out-of-plane strain vector, ϵ_{oL} , are defined as follows

$$\epsilon_{iL} = \begin{Bmatrix} \epsilon_{1L} \\ \epsilon_{2L} \\ \epsilon_{6L} \end{Bmatrix} = \mathbf{B}_{iL} \mathbf{u}_{u2} \quad (3.37)$$

$$\epsilon_{oL} = \begin{Bmatrix} \epsilon_{4L} \\ \epsilon_{5L} \end{Bmatrix} = \mathbf{B}_{oL} \mathbf{u}_{u1} \quad (3.38)$$

where

$$\mathbf{u}_{u2} = \left[\frac{\partial u}{\partial x} \quad \frac{\partial u}{\partial y} \quad \frac{\partial \psi_x}{\partial x} \quad \frac{\partial \psi_x}{\partial y} \quad \frac{\partial v}{\partial x} \quad \frac{\partial v}{\partial y} \quad \frac{\partial \psi_y}{\partial x} \quad \frac{\partial \psi_y}{\partial y} \quad \frac{\partial^2 w}{\partial x^2} \quad \frac{\partial^2 w}{\partial y^2} \quad \frac{\partial^2 w}{\partial x \partial y} \right]^T \quad (3.39)$$

$$\mathbf{B}_{iL} = \begin{bmatrix} 1 & 0 & z - \frac{4z^3}{3h^2} & 0 & 0 & 0 & 0 & 0 & -z & 0 & 0 \\ 0 & 0 & 0 & 0 & 0 & 1 & 0 & z - \frac{4z^3}{3h^2} & 0 & -z & 0 \\ 0 & 1 & 0 & z - \frac{4z^3}{3h^2} & 1 & 0 & z - \frac{4z^3}{3h^2} & 0 & 0 & 0 & -2z \end{bmatrix} \quad (3.40)$$

$$\mathbf{B}_{OL} = \begin{bmatrix} 0 & 1 - \frac{4z^2}{h^2} & 0 & 0 & 0 & 0 & 0 \\ 0 & 0 & 0 & 1 - \frac{4z^2}{h^2} & 0 & 0 & 0 \end{bmatrix} \quad (3.41)$$

As stated earlier the in-plane components of the electric displacement are known to be zero at all locations, thus only the out-of-plane electric displacement, D_3 , is left as an unknown. Substitution of Eqs. (3.34,37,38) into the equations of motion, Eqs. (3.24-26), yields the following system of equations

$$\begin{aligned} \int_0^t \int \left[\delta \mathbf{u}_{u1}^T \mathbf{B}_u^T \rho \mathbf{B}_u \ddot{\mathbf{u}}_{u1} + \delta \mathbf{u}_{u2}^T \mathbf{B}_{IL}^T \mathbf{c}_I^D \mathbf{B}_{IL} \mathbf{u}_{u2} + \delta \mathbf{u}_{u1}^T \mathbf{B}_{OL}^T \mathbf{c}_O^D \mathbf{B}_{OL} \mathbf{u}_{u1} \right. \\ \left. - \delta \mathbf{u}_{u2}^T \mathbf{B}_{IL}^T \mathbf{h}^T \mathbf{D}_3 - \delta \mathbf{D}_3 \mathbf{h} \mathbf{B}_{IL} \mathbf{u}_{u2} + \delta \mathbf{D}_3 \beta_{33}^S \mathbf{D}_3 \right] dV dt = \\ \int_0^t \left[\int \delta \mathbf{u}_{u1}^T \mathbf{B}_u^T \mathbf{f}_B dV + \int_S \left\{ \delta \mathbf{u}_{u1}^T \mathbf{B}_u^T \mathbf{f}_S + \delta \mathbf{D}_3 \phi \right\} dS + \delta \mathbf{u}_{u1}^T \mathbf{B}_u^T \mathbf{f}_P \right] dt \end{aligned} \quad (3.42)$$

Since all unknowns are functions of the in-plane coordinates, x and y , only, integration through the thickness is performed. It should be noted that the integration between the lower and lower surfaces, z_L and z_U , actually must involve a summation of integrations over each individual lamina, since the material properties can not be assumed to be constant through the thickness of the plate. First, the inertia term can be reduced to

$$\int_{z_L}^{z_U} \mathbf{B}_u^T \rho \mathbf{B}_u dz = \mathbf{L}_u^T \bar{\mathbf{I}} \mathbf{L}_u \quad (3.43)$$

where

$$\bar{\mathbf{I}} = \begin{bmatrix} \mathbf{I}_0 & \mathbf{I}_1 & \mathbf{I}_3 \\ \mathbf{I}_1 & \mathbf{I}_2 & \mathbf{I}_4 \\ \mathbf{I}_3 & \mathbf{I}_4 & \mathbf{I}_6 \end{bmatrix} \quad (3.44)$$

$$\mathbf{I}_i = \begin{bmatrix} 1 & 0 & 0 \\ 0 & 1 & 0 \\ 0 & 0 & 1 \end{bmatrix} \int_{z_L}^{z_U} \rho z^i dz \quad (3.45)$$

$$\mathbf{L}_u = \begin{bmatrix} 1 & 0 & 0 & 0 & 0 & 0 & 0 \\ 0 & 0 & 1 & 0 & 0 & 0 & 0 \\ 0 & 0 & 0 & 0 & 1 & 0 & 0 \\ 0 & 1 & 0 & 0 & 0 & -1 & 0 \\ 0 & 0 & 0 & 1 & 0 & 0 & -1 \\ 0 & 0 & 0 & 0 & 0 & 0 & 0 \\ 0 & \frac{-4}{3h^2} & 0 & 0 & 0 & 0 & 0 \\ 0 & 0 & 0 & \frac{-4}{3h^2} & 0 & 0 & 0 \\ 0 & 0 & 0 & 0 & 0 & 0 & 0 \end{bmatrix} \quad (3.46)$$

Next, the body force can be reduced by assuming that the local force is proportional the local density, as is generally the case for inertial loading.

$$\mathbf{f}_B = \rho \hat{\mathbf{f}}_B \quad (3.47)$$

Thus, the body force term becomes

$$\int_{-L}^U \mathbf{B}_u^T \mathbf{f}_B dz = \mathbf{L}_u^T \bar{\mathbf{I}} \hat{\mathbf{f}}_B \quad (3.48)$$

where

$$\bar{\mathbf{I}} = \begin{bmatrix} \mathbf{I}_0 \\ \mathbf{I}_1 \\ \mathbf{I}_3 \end{bmatrix} \quad (3.49)$$

Through-the-thickness integration of the strain potential energy terms yield

$$\int_{-L}^U \mathbf{B}_{IL}^T \mathbf{c}_I^D \mathbf{B}_{IL} dz = \mathbf{L}_{IL}^T \mathbf{C}_I \mathbf{L}_{IL} \quad (3.50)$$

$$\int_{-L}^U \mathbf{B}_{OL}^T \mathbf{c}_O^D \mathbf{B}_{OL} dz = \mathbf{L}_{OL}^T \mathbf{C}_O \mathbf{L}_{OL}$$

where

$$\mathbf{C}_I = \begin{bmatrix} \mathbf{C}_I^0 & \mathbf{C}_I^1 & \mathbf{C}_I^3 \\ \mathbf{C}_I^1 & \mathbf{C}_I^2 & \mathbf{C}_I^4 \\ \mathbf{C}_I^3 & \mathbf{C}_I^4 & \mathbf{C}_I^6 \end{bmatrix} \quad (3.51)$$

$$C_1^i = \int_L^U c_1^D z^i dz \quad (3.52)$$

$$C_o = \begin{bmatrix} C_o^0 & C_o^2 \\ C_o^2 & C_o^4 \end{bmatrix} \quad (3.53)$$

$$C_o^i = \int_L^U c_o^D z^i dz \quad (3.54)$$

$$L_{IL} = \begin{bmatrix} 1 & 0 & 0 & 0 & 0 & 0 & 0 & 0 & 0 & 0 & 0 \\ 0 & 0 & 0 & 0 & 0 & 1 & 0 & 0 & 0 & 0 & 0 \\ 0 & 1 & 0 & 0 & 1 & 0 & 0 & 0 & 0 & 0 & 0 \\ 0 & 0 & 1 & 0 & 0 & 0 & 0 & 0 & -1 & 0 & 0 \\ 0 & 0 & 0 & 0 & 0 & 0 & 0 & 1 & 0 & -1 & 0 \\ 0 & 0 & 0 & 1 & 0 & 0 & 1 & 0 & 0 & 0 & -2 \\ 0 & 0 & \frac{-4}{3h^2} & 0 & 0 & 0 & 0 & 0 & 0 & 0 & 0 \\ 0 & 0 & 0 & 0 & 0 & 0 & 0 & \frac{-4}{3h^2} & 0 & 0 & 0 \\ 0 & 0 & 0 & \frac{-4}{3h^2} & 0 & 0 & \frac{-4}{3h^2} & 0 & 0 & 0 & 0 \end{bmatrix} \quad (3.55)$$

$$L_{OL} = \begin{bmatrix} 0 & 1 & 0 & 0 & 0 & 0 & 0 \\ 0 & 0 & 0 & 1 & 0 & 0 & 0 \\ 0 & \frac{-4}{h^2} & 0 & 0 & 0 & 0 & 0 \\ 0 & 0 & 0 & \frac{-4}{h^2} & 0 & 0 & 0 \end{bmatrix} \quad (3.56)$$

Through-the-thickness integration of the piezoelectric coupling terms yield

$$\int_L^U \mathbf{B}_{IL}^T \mathbf{h}^T \mathbf{D}_3 dz = \mathbf{L}_{IL}^T \mathbf{P}^T \mathbf{D}_3 \quad (3.57)$$

where

$$\mathbf{P} = [\mathbf{P}_0 \quad \mathbf{P}_1 \quad \mathbf{P}_3] \quad (3.58)$$

$$\mathbf{P}_i = \int_L^U \mathbf{h} z^i dz \quad (3.59)$$

$$\mathbf{h} = [h_{31} \quad h_{32} \quad 0] \quad (3.60)$$

Through-the-thickness integration of the electric potential energy terms yields

$$\int_{z_L}^{z_U} \mathbf{D}_3 \beta_{33}^S \mathbf{D}_3 dz = \mathbf{D}_3 \mathbf{D}_3 \beta_{33}^S t_{pzt} \quad (3.61)$$

where t_{pzt} is the thickness of the piezoelectric layer. The displacement vectors in Eqs. (3.35) and (3.39) can be expressed using a finite element interpolation from the nodal vector, \mathbf{u}_e .

$$\mathbf{u}_{u1} = \mathbf{N}_{u1}(x, y) \mathbf{u}_e \quad (3.62)$$

$$\mathbf{u}_{u2} = \mathbf{N}_{u2}(x, y) \mathbf{u}_e \quad (3.63)$$

The finite element scheme developed in this work uses linear interpolation of the variables u , v , ψ_x and ψ_y , and a Hermit cubic polynomial function for the out of plane displacement, w . This results in seven mechanical degrees-of-freedom per node, u , v , ψ_x , ψ_y , w , $\partial w/\partial x$, and $\partial w/\partial y$.

3.1.5.2 Electric displacement

Now that the mechanical displacements have been reduced via finite elements to nodal degrees of freedom, it is now necessary to address the distribution of electric displacement. Since electrodes cover the entire in-plane surfaces of the piezoelectric layer, the electric displacement can be described as the charge per unit area on the electrodes.

$$\mathbf{D}_3 = \frac{\partial q}{\partial A} \quad (3.64)$$

where q is the amount of positive charge on the lower electrode and A is the surface area of the PZT electrode. There are two possible methods for treating the distribution of electric displacement across the piezoelectric layer. The most general method is to use a finite element interpolation, and relate the distribution to the electric displacement at a given set of nodes. The electric displacement then becomes

$$\mathbf{D}_3 = \mathbf{N}_q(x, y) \mathbf{D}_e \quad (3.65)$$

where \mathbf{D}_e , is the nodal electrical displacement and $\mathbf{N}_q(x,y)$ is the interpolation matrix. Integrating over the area of the plate using Gauss quadrature on each of the finite elements yields gives the governing equations for the coupled theory.

$$\delta \Pi_u = \delta \mathbf{u}_e^T \int_{t_0}^t (-\mathbf{M}_u \ddot{\mathbf{u}}_e - \mathbf{K}_{uu} \mathbf{u}_e - \mathbf{K}_{uD} \mathbf{D}_e + \mathbf{F}_u) dt = 0 \quad (3.66a)$$

$$\delta \Pi_D = \delta \mathbf{D}^T \int_{t_0}^t (-\mathbf{K}_{Du} \mathbf{u}_e - \mathbf{K}_{DD} \mathbf{D}_e + \mathbf{F}_D) dt = 0 \quad (3.66b)$$

where \mathbf{M}_u is the structural mass matrix, the matrix \mathbf{K}_{uu} is the mechanical stiffness matrix, \mathbf{K}_{DD} is the electrical stiffness matrix, and \mathbf{K}_{uD} and \mathbf{K}_{Du} are the stiffness matrices due to piezoelectric-mechanical coupling. The vectors \mathbf{F}_u and \mathbf{F}_D are the force vectors due to mechanical and electrical loading. These matrices and vectors are defined as follows

$$\mathbf{M}_u = \sum_{i=1}^{ngp} \sum_{j=1}^{ngp} w_i w_j |\mathbf{J}| \mathbf{N}_{u1}^T \mathbf{L}_u^T \bar{\mathbf{I}} \mathbf{L}_u \mathbf{N}_{u1} \quad (3.67)$$

$$\mathbf{K}_{uu} = \sum_{i=1}^{ngp} \sum_{j=1}^{ngp} w_i w_j |\mathbf{J}| \left\{ \mathbf{N}_{u2}^T \mathbf{L}_{IL}^T \mathbf{C}_I \mathbf{L}_{IL} \mathbf{N}_{u2} + \mathbf{N}_{u1}^T \mathbf{L}_{OL}^T \mathbf{C}_O \mathbf{L}_{OL} \mathbf{N}_{u1} \right\} \quad (3.68a)$$

$$\mathbf{K}_{uD} = - \sum_{i=1}^{ngp} \sum_{j=1}^{ngp} w_i w_j |\mathbf{J}| \mathbf{N}_{u2}^T \mathbf{L}_{IL}^T \mathbf{P}^T \mathbf{N}_q \quad (3.68b)$$

$$\mathbf{K}_{Du} = \mathbf{K}_{uD}^T = - \sum_{i=1}^{ngp} \sum_{j=1}^{ngp} w_i w_j |\mathbf{J}| \mathbf{N}_q^T \mathbf{P} \mathbf{L}_{IL} \mathbf{N}_{u2} \quad (3.68c)$$

$$\mathbf{K}_{DD} = \sum_{i=1}^{ngp} \sum_{j=1}^{ngp} w_i w_j |\mathbf{J}| \mathbf{N}_q^T \mathbf{N}_q \beta_{33}^S t_{pzt} \quad (3.68d)$$

$$\mathbf{F}_u = \mathbf{N}_{u1}^T \mathbf{B}_u^T \mathbf{f}_p + \sum_{i=1}^{ngp} \sum_{j=1}^{ngp} w_i w_j |\mathbf{J}| \left\{ \mathbf{N}_{u1}^T \mathbf{L}_u^T \bar{\mathbf{I}} \hat{\mathbf{f}}_B + \mathbf{N}_{u1}^T \mathbf{B}_u^T \mathbf{f}_s \right\} \quad (3.69a)$$

$$\mathbf{F}_D = \sum_{i=1}^{ngp} \sum_{j=1}^{ngp} w_i w_j |\mathbf{J}| \mathbf{N}_q^T \boldsymbol{\phi} \quad (3.69b)$$

where ngp is the number of gauss points used and w_i and w_j are the gauss point weights. The value A_e represents the area of each element and is necessary for converting electric displacement to total charge.

The result system of equations can be expressed in matrix form as

$$\begin{bmatrix} \mathbf{M}_u & \mathbf{0} \\ \mathbf{0} & \mathbf{0} \end{bmatrix} \begin{Bmatrix} \ddot{\mathbf{u}}_e \\ \ddot{\mathbf{D}} \end{Bmatrix} + \begin{bmatrix} \mathbf{C}_u & \mathbf{0} \\ \mathbf{0} & \mathbf{0} \end{bmatrix} \begin{Bmatrix} \dot{\mathbf{u}}_e \\ \dot{\mathbf{D}} \end{Bmatrix} + \begin{bmatrix} \mathbf{K}_{uu} & \mathbf{K}_{ud} \\ \mathbf{K}_{du} & \mathbf{K}_{dd} \end{bmatrix} \begin{Bmatrix} \mathbf{u}_e \\ \mathbf{D} \end{Bmatrix} = \begin{Bmatrix} \mathbf{F}_u \\ \mathbf{F}_D \end{Bmatrix} \quad (3.70)$$

To incorporate structural damping into the equations a structural damping matrix \mathbf{C}_u is added. The nature of the damping matrix can be chosen to meet the needs of the user. In this work classical damping has been used.

A second method is possible for cases when the strain across the piezoelectric device can be assumed to be constant. This assumption would be valid for small patches attached to relatively large structures and not near any stress concentrations. Since the strain across the piezoelectric layer is assumed to be constant, then the electric displacement can thereby be assumed to be constant. For this case Eq. (3.64) is reduced to

$$\mathbf{D}_3 = \frac{\partial q}{\partial A} \approx \frac{q}{A} \quad \text{for small PZTs} \quad (3.71)$$

where q is the total charge on the electrodes. Thus, the governing equations can now be expressed in terms of the charge flow in each piezoelectric device. The advantage of this is that each piezoelectric device added to the structure only adds a single electrical degree of freedom to the system. Thus, modeling of a complex smart structural system can be accomplished with little more computational effort than that required for the original structure. Integrating over the area of the plate yields the governing equations

$$\delta \Pi_u = \delta \mathbf{u}_e^T \int_{t_0}^t \left(-\mathbf{M}_u \ddot{\mathbf{u}}_e - \mathbf{K}_{uu} \mathbf{u}_e - \mathbf{K}_{uq} \mathbf{q} + \mathbf{F}_u \right) dt = 0 \quad (3.72a)$$

$$\delta \Pi_q = \delta \mathbf{q}^T \int_{t_0}^t \left(-\mathbf{K}_{qu} \mathbf{u}_e - \mathbf{K}_{qq} \mathbf{q} + \mathbf{F}_q \right) dt = 0 \quad (3.72b)$$

where \mathbf{q} is the vector of the PZT charges and \mathbf{M}_u is the structural mass matrix. and \mathbf{C}_u is the structural damping matrix. The matrix \mathbf{K}_{uu} is the mechanical stiffness matrix, \mathbf{K}_{qq} is the electrical stiffness matrix, and \mathbf{K}_{uq} and \mathbf{K}_{qu} are the stiffness matrices due to piezoelectric-mechanical coupling. The vectors \mathbf{F}_u and \mathbf{F}_q are the force vectors due to mechanical and electrical loading. These terms are defined in Eqs. (3.67), (3.68a), (3.69a) and as follows

$$\mathbf{K}_{uq} = -\frac{1}{A_e} \sum_{i=1}^{ngp} \sum_{j=1}^{ngp} w_i w_j |\mathbf{J}| \mathbf{N}_{u2}^T \mathbf{L}_{1L}^T \mathbf{P}^T \quad (3.73a)$$

$$\mathbf{K}_{qu} = \mathbf{K}_{uq}^T = -\frac{1}{A_e} \sum_{i=1}^{ngp} \sum_{j=1}^{ngp} w_i w_j |\mathbf{J}| \mathbf{P} \mathbf{L}_{1L} \mathbf{N}_{u2} \quad (3.73b)$$

$$\mathbf{K}_{qq} = \frac{1}{A_e^2} \sum_{i=1}^{ngp} \sum_{j=1}^{ngp} w_i w_j |\mathbf{J}| \beta_{33}^S t_{pzt} \quad (3.73c)$$

$$\mathbf{F}_q = \Phi \quad (3.74)$$

Similarly, the governing equations can be written in matrix form as follows

$$\begin{bmatrix} \mathbf{M}_u & \mathbf{0} \\ \mathbf{0} & \mathbf{0} \end{bmatrix} \begin{Bmatrix} \ddot{\mathbf{u}}_e \\ \ddot{\mathbf{q}} \end{Bmatrix} + \begin{bmatrix} \mathbf{C}_u & \mathbf{0} \\ \mathbf{0} & \mathbf{0} \end{bmatrix} \begin{Bmatrix} \dot{\mathbf{u}}_e \\ \dot{\mathbf{q}} \end{Bmatrix} + \begin{bmatrix} \mathbf{K}_{uu} & \mathbf{K}_{uq} \\ \mathbf{K}_{qu} & \mathbf{K}_{qq} \end{bmatrix} \begin{Bmatrix} \mathbf{u}_e \\ \mathbf{q} \end{Bmatrix} = \begin{Bmatrix} \mathbf{F}_u \\ \mathbf{F}_q \end{Bmatrix} \quad (3.75)$$

The choice of which method to use depends on the structural system being analyzed. If a strain gradient across the piezoelectric layer is present then large errors can result from using the second method. For the majority of the results shown in this work the finite element discretization of the electric displacement has been used to ensure accuracy.

3.1.6. Electrical equations

The absence of any electrical inertia or damping terms in Eqs. (3.70) and (3.75) is a result of only considering the mechanical aspects of the smart structure. When considering a smart structure as a whole, additional terms must be added for electrical components in the system. For a simple LRC circuit, the variational energy must include the following

$$\delta \Pi_q = \delta \left(\frac{1}{2} L \dot{q}^2 \right) - \delta q R \dot{q} - \delta \left(\frac{1}{2C} q^2 \right) + V \delta q \quad (3.76)$$

where L , R and C are the inductance, resistance and capacitance, and V is the applied voltage. The importance of formulating Hamilton's Principle in terms of the charge, rather than electric field or potential, now becomes apparent. If the equations of motion for any electrical system attached to the smart structure can be formulated in the following form

$$\mathbf{M}_q \ddot{\mathbf{q}}_e + \mathbf{C}_q \dot{\mathbf{q}}_e + \mathbf{K}_q \mathbf{q}_e = \mathbf{F}_q \quad (3.77)$$

then these equations can be directly combined with Eq. (3.75). This combination results in a completely coupled electrical-mechanical system of the following form

$$\begin{bmatrix} \mathbf{M}_u & \mathbf{0} \\ \mathbf{0} & \mathbf{M}_q \end{bmatrix} \begin{Bmatrix} \ddot{\mathbf{u}}_e \\ \ddot{\mathbf{q}}_e \end{Bmatrix} + \begin{bmatrix} \mathbf{C}_u & \mathbf{0} \\ \mathbf{0} & \mathbf{C}_q \end{bmatrix} \begin{Bmatrix} \dot{\mathbf{u}}_e \\ \dot{\mathbf{q}}_e \end{Bmatrix} + \begin{bmatrix} \mathbf{K}_{uu} & \mathbf{K}_{uq} \\ \mathbf{K}_{qu} & \mathbf{K}_{qq}^* \end{bmatrix} \begin{Bmatrix} \mathbf{u}_e \\ \mathbf{q}_e \end{Bmatrix} = \begin{Bmatrix} \mathbf{F}_u \\ \mathbf{F}_q \end{Bmatrix} \quad (3.78)$$

where \mathbf{q}_e includes not only the charge associated with the PZTs, but also the electrical system. Matrix \mathbf{K}_{qq}^* also includes the electrical stiffness components of both the PZTs and the electrical system. If the electric displacement was discretized then it is necessary to use the following relation between the electric displacement and the total PZT charge

$$q_i = \left(\int_S \mathbf{N}_q dS \right) \mathbf{D}_{ie} \quad \text{or} \quad \mathbf{q} = \mathbf{A}_q \mathbf{D}_e \quad (3.79)$$

Combining Eqs. (3.70), (3.77) and (3.79), the resulting coupled electrical-mechanical system equations are obtained

$$\begin{bmatrix} \mathbf{M}_u & \mathbf{0} \\ \mathbf{0} & \mathbf{A}_q^T \mathbf{M}_q \mathbf{A}_q \end{bmatrix} \begin{Bmatrix} \ddot{\mathbf{u}}_e \\ \ddot{\mathbf{D}}_e \end{Bmatrix} + \begin{bmatrix} \mathbf{C}_u & \mathbf{0} \\ \mathbf{0} & \mathbf{A}_q^T \mathbf{C}_q \mathbf{A}_q \end{bmatrix} \begin{Bmatrix} \dot{\mathbf{u}}_e \\ \dot{\mathbf{D}}_e \end{Bmatrix} + \begin{bmatrix} \mathbf{K}_{uu} & \mathbf{K}_{ud} \\ \mathbf{K}_{du} & \mathbf{K}_{dd} + \mathbf{A}_q^T \mathbf{K}_q \mathbf{A}_q \end{bmatrix} \begin{Bmatrix} \mathbf{u}_e \\ \mathbf{D}_e \end{Bmatrix} = \begin{Bmatrix} \mathbf{F}_u \\ \mathbf{F}_d \end{Bmatrix} \quad (3.80)$$

Equations (3.78) and (3.80) provide the means to solve a variety of coupled piezoelectric-mechanical problems. The eigenvalues and eigenvectors can be determined to compute the natural frequencies and mode shapes of the system. The complex linear problem can be solved to determine the forced response of the system to a harmonic excitation. Another advantage of this

model is that the integration of the structural finite element model and electrical components allows for design of passive damping circuits for complicated structures using multi-variable optimization methods. This technique would allow determination of optimum PZT location, orientation and the electrical component values for single or multi-mode damping of the structure.

3.1.7. *Boundary Conditions*

The developed system equations shown in Eqs. (3.78) and (3.80) apply to an unconstrained plate and do not take into account any mechanical or electrical constraints. Mechanical constraints are applied to the finite element system in the conventional manner using the elimination approach. Boundary conditions for the electrical system must also be applied depending on the nature of the electrical system that is assumed.

If the electrical system is fully modeled using Eq. (3.78) or (3.80) then the electrical system is fully described and additional boundary conditions are generally not required. However, it is also permissible to not include the electrical circuitry equations and instead use Eq. (3.70) or (3.75) to describe the system. In this manner a direct voltage can be assumed to be applied to each piezoelectric device or a fixed amount of charge flow can be applied as a boundary condition. This method neglects the effects of resistance and inductance in the electrical system, but it is in most cases convenient and accurate. The application of a fixed voltage corresponds to the traditional method of in which an actuator is controlled. If the applied voltage is zero then the PZT is assumed to be shorted out and the resulting charge flow from the device acts as a sensor signal. The voltage is applied as a load and appears in the forcing vector on the right-hand side. If the piezoelectric device is assumed to be open circuited then the net charge flow from the device will be zero. If the system is formulated in terms of total charge using Eq. (3.75), then the fixed value of charge is easily applied as a boundary condition using the elimination method. However, if the electric displacement has been discretized using nodal

electrical displacements with Eq. (3.70) then one must be careful to specify that the net charge flow be zero, not the individual nodal electrical displacements. The net charge flow in Eq. (3.79) is specified to be zero creating a single constraint equation for each piezoelectric device. This equation can be enforced using the penalty method creating a submatrix, $c_{pen} \mathbf{A}_q^T \mathbf{A}_q$, to be added to the system stiffness matrix. Results show that the solution is rather insensitive to the penalty value, c_{pen} , and that values around 10^2 times the maximum diagonal component of \mathbf{K}_{uu} work well.

Once appropriate boundary conditions are applied the resulting system of equations can be solved based on the type of analysis required. For ease of notation, this system of equations is simplified to the following form

$$\mathbf{ma} + \mathbf{cv} + \mathbf{ku} = \mathbf{f} \quad (3.81)$$

It is important to note that the system vectors \mathbf{u} , \mathbf{v} , and \mathbf{a} include not only mechanical displacements, but also the electrical displacements or charge flow depending on how the system of equations was developed.

3.1.8. System reduction

Often it is desired to reduce a system using the mode shapes rather than work with the full finite element model. This drastically reduces the number of degrees of freedom and allows for much faster computations once the eigen system is solve for. This is often done in structural mechanics because the necessary assumption that the modal matrix (Φ) uncouples the damping matrix \mathbf{C} is usually valid for structural damping. That is

$$\Phi^T \mathbf{C} \Phi = \text{diag}[\mu_1 \quad \mu_2 \quad \cdots \quad \mu_m] \quad (3.82)$$

However, this assumption cannot be made for most electrical systems that would be connected to the PZTs. So, in general, the coupled electrical-mechanical system of Eq. (3.78) could not be reduced in its entirety using a few of its mode shapes.

The system can be partially reduced using the structural mode shapes if the assumption is made that the mode shapes for the actual coupled system can be expressed in terms of the open circuit mode shapes. This assumption is generally very reasonable since changes in the elastic stiffness of PZTs due to open circuiting or short circuiting cause only modest shifts in natural frequency and very small alterations in the mode shapes. The structural stiffness added by the PZTs is generally small compared to the stiffness of the base structure and the difference between open circuit and short circuit stiffness is only around ten to twenty percent. This combined with the fact that PZTs usually only cover a fraction of the structural surface means that the differences in mode shapes between the open circuited condition and the actual structure will be generally small and localized.

First, the coupled system is reduced so that the open circuit eigenvalue problem can be solved for the desired number of eigenvalues.

$$\mathbf{K}_{uu}\varphi = \omega_{oc}^2 \mathbf{M}_u \varphi \quad (3.83)$$

Then using Eq. (3.82) and

$$\Phi^T \mathbf{K}_{uu} \Phi = \text{diag}[\omega_{oc1}^2 \quad \omega_{oc2}^2 \quad \dots \quad \omega_{ocm}^2] \quad (3.84)$$

$$\Phi^T \mathbf{M}_u \Phi = \mathbf{I}_m \quad (3.85)$$

the coupled system of Eq. (3.78) can be reduced to

$$\begin{bmatrix} \mathbf{I}_m & \mathbf{0} \\ \mathbf{0} & \mathbf{M}_q \end{bmatrix} \begin{Bmatrix} \ddot{\mathbf{r}} \\ \ddot{\mathbf{q}}_e \end{Bmatrix} + \begin{bmatrix} \text{diag}[\mu_m] & \mathbf{0} \\ \mathbf{0} & \mathbf{C}_q \end{bmatrix} \begin{Bmatrix} \dot{\mathbf{r}} \\ \dot{\mathbf{q}}_e \end{Bmatrix} + \begin{bmatrix} \text{diag}[\omega_m^2] & \Phi^T \mathbf{K}_{uq} \\ \mathbf{K}_{qu} \Phi & \mathbf{K}_{qq} \end{bmatrix} \begin{Bmatrix} \mathbf{r} \\ \mathbf{q}_e \end{Bmatrix} = \begin{Bmatrix} \Phi^T \mathbf{F}_u \\ \mathbf{F}_q \end{Bmatrix} \quad (3.86)$$

where

$$\mathbf{r} = \Phi^{-1} \mathbf{u}_e \quad (3.87)$$

Now the problem has been reduced to a small system composed of only the electrical degrees of freedom and the chosen number of mode shapes.

3.2. Results and Verification

In this section a comparison is made between the developed model and known solutions to problems. First the finite element model is validated by comparing static deflections and natural frequencies with published results for both isotropic and orthotropic plates. Next the results predicted by the model for plates with passive electrical damping circuits are compared with experimental results, demonstrating the ability of the developed theory to model smart structural systems.

Table 3.1.
Finite element convergence.

Result	Finite element mesh size				
	4x4	8x8	16x16	32x32	64x64
\bar{w}	0.04729	0.04512	0.04457	0.04443	0.04440
$\bar{\sigma}_1$	0.31304	0.29353	0.28887	0.28772	0.28743

3.2.1. Finite Element Verification

In order to verify correct finite element modeling and implementation of the higher order laminate theory a test specimen is modeled to allow comparison with published results. A rectangular plate simply supported on all four sides is modeled under a uniform pressure. The plate has edges of lengths a and b , and has thickness, h . The displacements and stresses have been normalized using the following relation

$$\bar{w} = w \left(\frac{a}{2}, \frac{b}{2} \right) \frac{h^3 E_2}{q_0 a^4} \quad (3.88a)$$

$$\bar{\sigma}_i = \sigma_i \left(\frac{a}{2}, \frac{b}{2}, \pm \frac{h}{2} \right) \frac{h^2}{q_0 a^2} \quad i = 1, 2 \quad (3.88b)$$

$$\bar{\sigma}_6 = \sigma_6 \left(0, 0, \pm \frac{h}{2} \right) \frac{h^2}{q_0 a^2} \quad (3.88c)$$

$$\bar{\sigma}_4 = \sigma_4 \left(\frac{a}{2}, 0, 0 \right) \frac{h}{q_0 a} \quad (3.88d)$$

$$\bar{\sigma}_5 = \sigma_5 \left(0, \frac{b}{2}, 0 \right) \frac{h}{q_0 a} \quad (3.88e)$$

The first check that was performed on the finite element model was to check that the results converged with an increasing number of nodes. The ratio of the length of the plate edge, a , to the thickness, h , was taken to be 100 and the plate was assumed to be square ($a=b$). The plate is assumed to be isotropic with a Poisson's ratio, ν , of 0.3 and an elastic modulus, E , of 160Gpa. Table 3.1 shows the out-of-plane displacement and the maximum in-plane stress at the center of

Table 3.2.

Stress and displacement comparison for an isotropic simply supported plate.

b/a	a/h	Source	w	$\pm \sigma_1$	$\pm \sigma_2$	σ_6	$-\sigma_4$	$-\sigma_5$
1	5	FEM	0.5369	0.2944	0.2944	0.2210	0.4956	0.4956
		Reddy	0.0535	0.2944	0.2944	0.2112	0.4840	0.4840
	10	FEM	0.04679	0.2889	0.2889	0.2031	0.5031	0.5031
		Reddy	0.0467	0.2890	0.2890	0.1990	0.4890	0.4890
	100	FEM	0.04451	0.2871	0.2871	0.1957	0.5062	0.5062
		Reddy	0.0444	0.2873	0.2873	0.1947	0.4909	0.4909
	CPT	FEM	0.04449	0.2871	0.2871	0.1956	-	-
		Reddy	0.0444	0.2873	0.2873	0.1946	-	-
	5	FEM	0.1251	0.6200	0.2815	0.3058	0.6896	0.5455
		Reddy	0.1248	0.6202	0.2818	0.2927	0.6745	0.5201
2	10	FEM	0.1144	0.6121	0.2783	0.2863	0.6955	0.5512
		Reddy	0.1142	0.6125	0.2789	0.2809	0.6794	0.5230
	100	FEM	0.1109	0.6095	0.2773	0.2789	0.6977	0.5533
		Reddy	0.1106	0.6100	0.2779	0.2769	0.6813	0.5240
	CPT	FEM	0.1109	0.6094	0.2773	0.2788	-	-
		Reddy	0.1106	0.6100	0.2779	0.2769	-	-

the plate using differing numbers of elements. The results show good convergence with an increasing number of nodes for both displacements and stresses, and the results using a modest number of elements per side (~ 10 -20) are seen to be reasonably accurate.

Next the finite element implementation of the higher order plate theory is verified against the numerical results presented by Reddy (1984b). The plate under consideration is isotropic ($\nu=0.3$) and comparison is made for a variety of plate thicknesses. The finite element model used 19 by 19 elements for the square plate and 13 by 25 elements for the rectangular plate. The results are presented in Table 3.2.

Next a comparison is made using an orthotropic material. The plate had an edge length of $b=0.32\text{m}$, and a 1Mpa uniform pressure was applied. For the case of $b/a = 1$ a 19 by 19 element mesh was used. For the case of $b/a=2$ a 13 by 25 element mesh was used. The orthotropic material properties used were

$$\begin{aligned} E_1 &= 143.6\text{GPa} & E_2 &= 75.43\text{GPa} & G_{12} &= 42.06\text{GPa} \\ G_{13} &= 25.58\text{GPa} & G_{23} &= 42.68\text{GPa} & \nu_{12} &= 0.44 & \nu_{21} &= 0.23 \end{aligned} \quad (3.89)$$

The results for the finite element model as well as the exact elasticity solution from Srinivas, Rao and Rao (1970) are shown in Table 3.3.

A final verification is made using the computed natural frequencies for a square plate.

Table 3.3.

Stress and displacement comparison for an orthotropic plate.

b/a	h/a	w (mm)			σ_1 (Mpa)			σ_5 (Mpa)		
		Exact	HOT	CPT	Exact	HOT	CPT	Exact	HOT	CPT
1	0.05	1.044	1.045	1.029	144.3	144.6	144.2	10.85	11.17	-
	0.10	0.1377	0.1369	0.1286	36.01	36.45	36.06	5.382	5.562	-
	0.14	0.05350	0.05282	0.04686	18.34	18.79	18.40	3.805	3.953	-
2	0.05	1.077	1.074	1.064	262.7	262.4	262.0	14.05	14.32	-
	0.10	0.1408	0.1384	0.1329	65.97	65.90	65.49	6.927	7.138	-
	0.14	0.05421	0.05235	0.04845	33.86	33.82	33.41	4.878	5.082	-

The plate is assumed to be made of an isotropic material with a Poisson's ratio, ν , of 0.3, an elastic modulus, E , of 160Gpa and a density of 2000kg/m³. A 19 by 19 element mesh is used for modeling, and the length to thickness ratio (a/h) considered is 10. The results are presented in Table 3.4 along with the exact values from Srinivas, Rao and Rao (1970). The natural frequencies have been normalized using

$$\bar{\omega} = \omega h \sqrt{\frac{\rho}{G}} \quad (3.90)$$

The results show good correlation with the exact solution values. The differences seen in the higher frequency modes are a result of the coarseness of the finite element mesh and a finer mesh size would provide more accurate results.

Table 3.4.

Natural frequencies computed using finite element model compared with exact results.

m	n	Exact	HOT	CPT
1	1	0.0932	0.09289	0.09539
2	1	0.226	0.2214	0.2354
2	2	0.3421	0.3386	0.3710
1	3	0.4171	0.4140	0.4617
2	3	0.5239	0.5166	0.5903
1	4	-	0.6508	0.7649
3	3	0.6889	0.6751	0.7987
2	4	0.7511	0.7386	0.8846

3.2.2. Passive Electrical Damping

To study the validity of simultaneously modeling the electrical and mechanical aspects of a smart structural system it is necessary to compare the model results with experimental data for a structural system with a well-defined electrical system. One such smart structural system is that of a piezoelectric patch connected to a passive electrical damping circuit. Passive damping circuits usually consist of only inductors, resistors and sometimes capacitors, making them easy

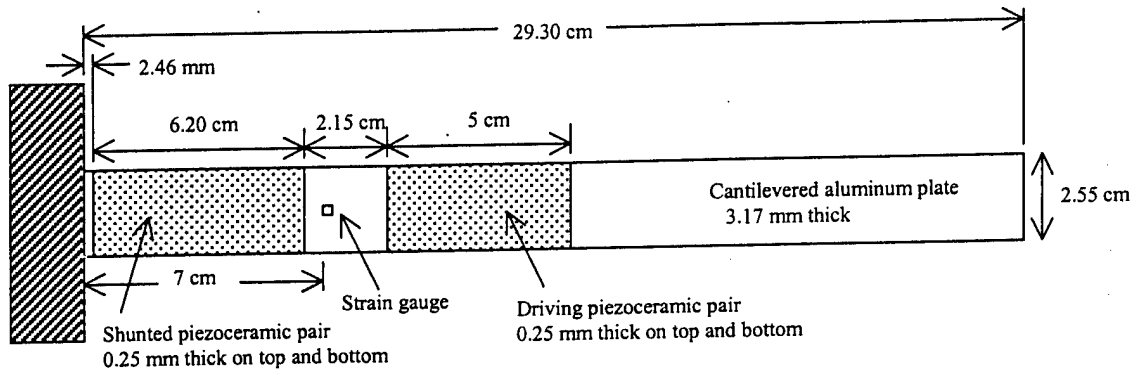


Fig. 3.2. Top view of cantilevered plate with driving and shunted piezoceramic pairs.

to model with linear electrical equations. Also, there is a far amount of literature that has been published on passive damping circuits, providing a good deal of experimental data ideal for model validation.

A cantilevered plate with a shunt damping circuit studied by Hagood and Von Flotow (1991) is first examined. The aluminum plate seen in Fig. 3.2 has two pairs of PZTs mounted on the upper and lower surfaces. One pair is actuated in opposite directions to drive the vibration of the plate and the other is connected to an inductor and resistor in series. The material properties of the plate and PZTs are listed in Table 3.5.

The cantilevered plate was modeled with a 28x3 finite element mesh. The higher order laminate theory results in 7 degrees of freedom per node and 812 degrees of freedom total. The

Table 3.5.

Material properties from experiments of Hagood and Von Flotow.

Material property	Aluminum	PZT
E (Gpa)	73.0	63.0
ν	0.33	0.3 ^a
ρ (kg/m ³)	2800 ^a	7750 ^a
d_{31} (m/V)	n/a	180×10^{-12}
e_3^S (F/m)	n/a	9.22×10^{-9}

^a Assumed values

charge across the four PZT patches was described by four additional degrees of freedom. The open circuit mass matrix, \mathbf{M}_{uu} , and stiffness matrix, \mathbf{K}_{uu} , are used to solve for the first twelve open circuit modes with a LAPACK generalized eigen solver. The system is then reduced using Eq. (3.86) in order to determine the frequency response. The electrical equations for the each circuit are now added directly to the resulting set of equations. A damping coefficient of $\xi=0.01$ was assumed for each mode to create the damping matrix,

The model is first analyzed using an untuned shunt circuit containing only a resistor and no inductor. The increase in the damping coefficient, ξ , for the first bending mode is then calculated for a variety of resistance values. These results are shown in Fig. 3.3 against the non-dimensional resistance. The non-dimensional resistance is the ratio of the actual resistance to the optimum value of $28.68\text{k}\Omega$ predicted by Hagood and Flotow (1991). The results show good correlation with the published experimental values. Since the structural damping of the beam with the PZTs shorted out was only 0.16%, the untuned shunt damping circuit can be seen to roughly quadruple the damping of the structural system.

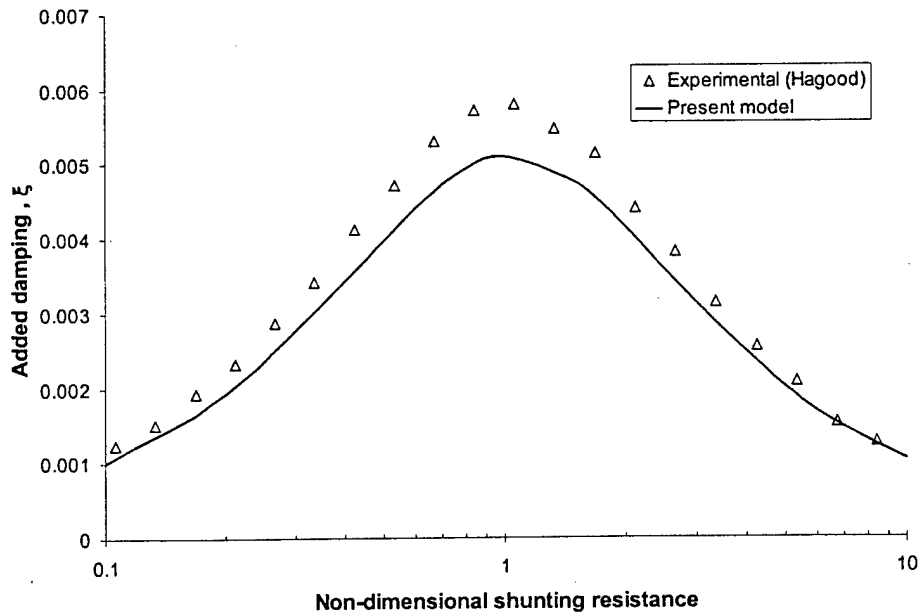


Fig. 3.3. Added damping to first mode of the cantilevered plate for untuned resistance shunting.

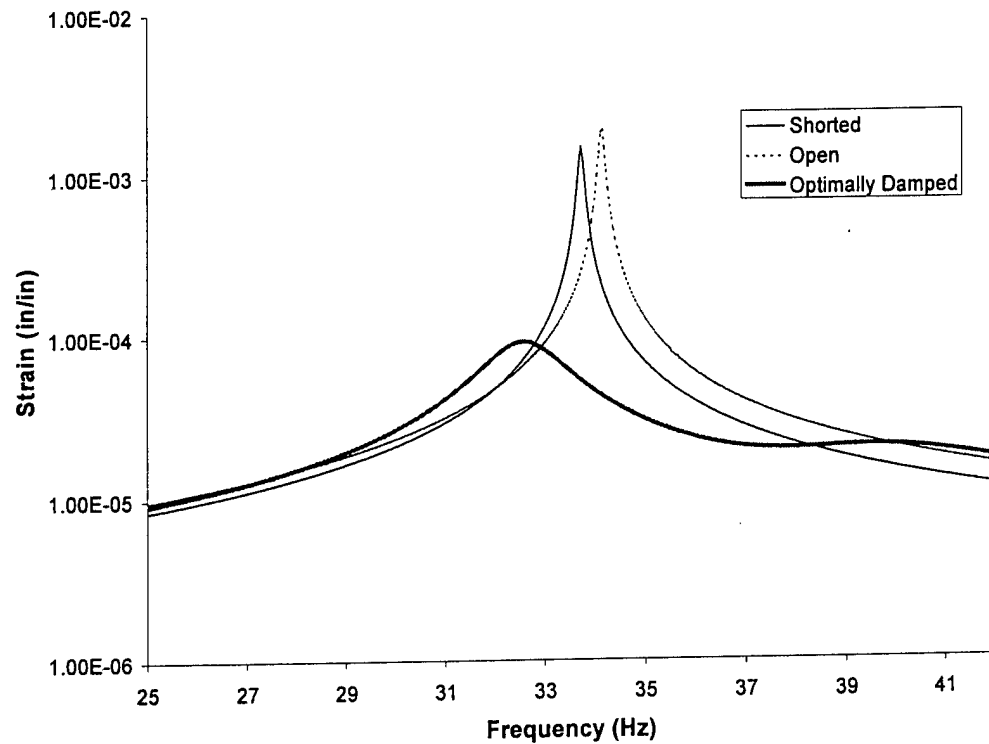


Fig. 3.4. Analytical strain for first mode actuation of cantilevered plate with shunted piezoceramic pair open, shunted and optimally tuned and damped.

The plate is then modeled with a tuned shunt damping circuit. The inductor used has the optimum value of 148.2 H predicted by the literature (Hagood and Flotow, 1991). It is connected in series with a resistor having a varying amount of resistance. Figure 3.4 shows the first bending mode frequency response for the plate with three conditions for the shunted PZTs; open circuited, shorted out, and optimally damped using the values of Hagood and Flotow (1991). The results clearly show the reduction in natural frequency caused by shorting out the PZT. Also Fig. 3.4 shows how efficient the tuned damping circuit can be at damping out a particular mode of vibration. The frequency response for the first mode is also shown in Fig. 3.5 for varying resistance. When the resistance is infinitely large, the system behaves as in open case. As resistance decreases, the damping increases, flattening the system response. As resistance decreases below the optimum value of 6640Ω the system begins to develop two separate peaks.

These results show fair correlation with the experimental data of Hagood and Flotow (1991) presented in Fig. 3.6; however, there are still noticeable differences. This is most likely the result of inaccuracy in the predicted natural frequency of the current theory. The finite element model predicts an open circuit natural frequency of 34.136 Hz as opposed to the measured natural frequency of 33.77 Hz. This is most likely caused by a combination of the finite element discretization and difference between the assumed material properties and the actual properties. When the finite element model is modified using lower stiffnesses to closely match the experimental value of natural frequency, the frequency responses are almost identical to the experimental results of Hagood and Flotow (1991), as shown in Fig. 3.7.

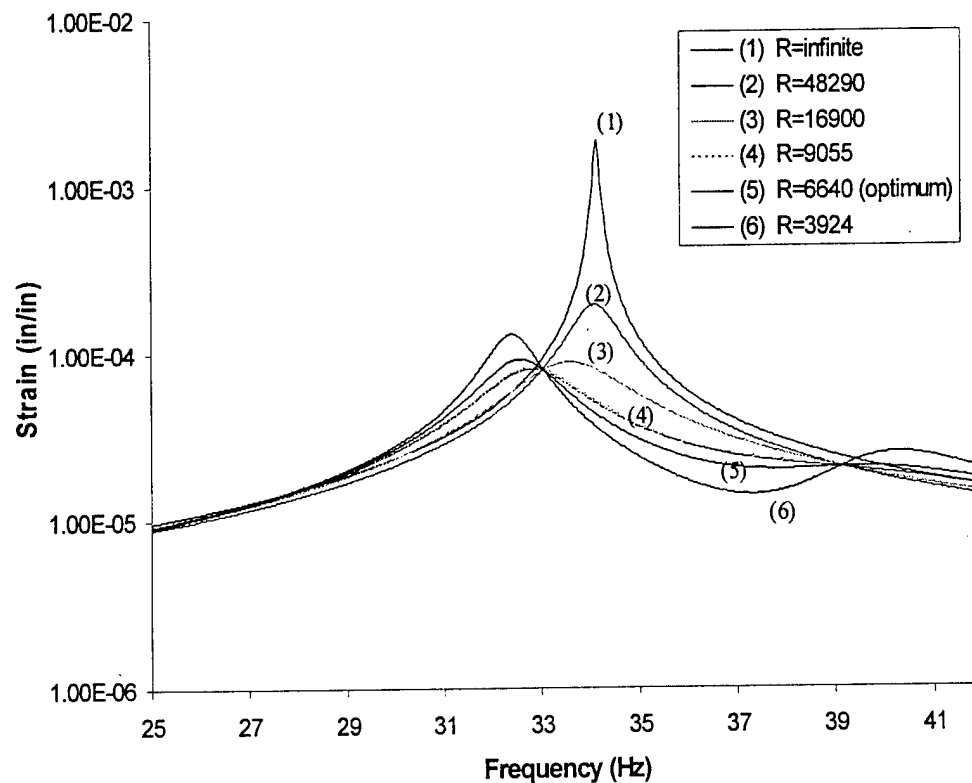


Fig. 3.5. Analytical strain for first mode actuation of cantilevered plate with tuned shunt circuit and varying resistance.

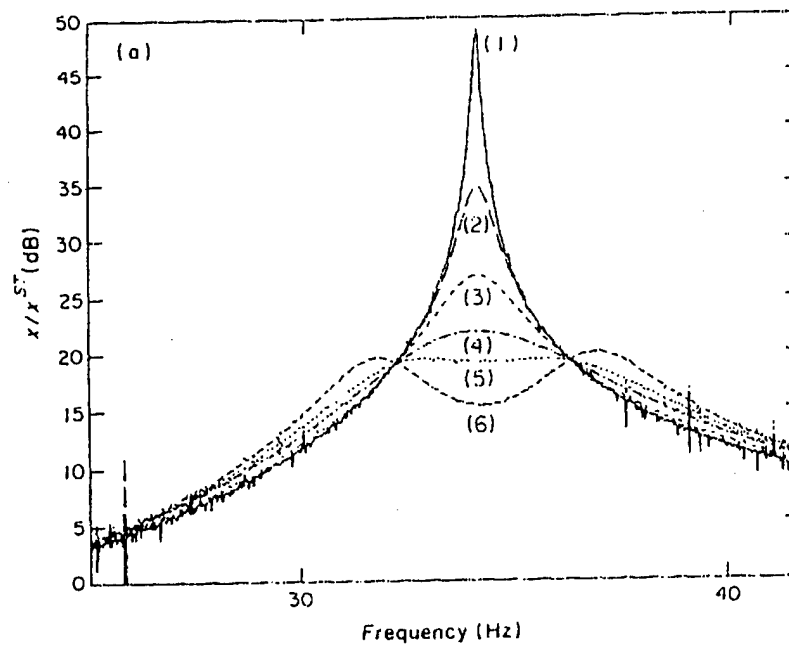


Fig. 3.6. Hagood's experimental results for first mode actuation of cantilevered plate with tuned shunt circuit and varying resistance.

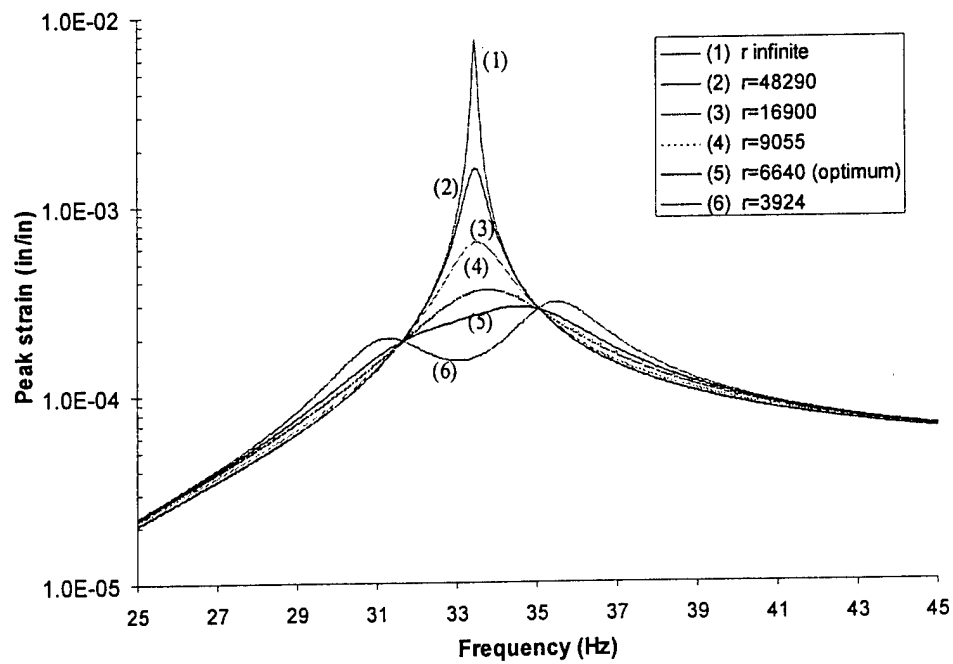


Fig. 3.7. Strain for first mode actuation of the modified cantilevered plate with tuned shunt circuit and varying resistance.

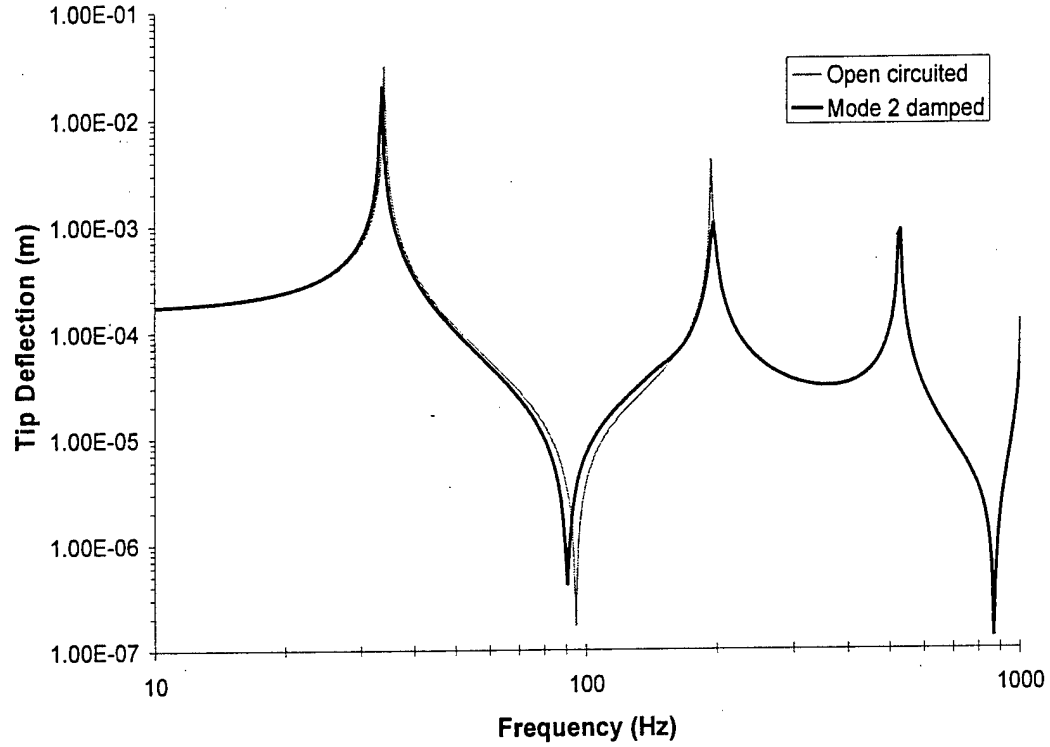


Fig. 3.8. Frequency response for aluminum plate with mode 2 damped.

Next the multi-mode damping technique of Wu (1998) is used on the same cantilevered aluminum plate. When a single mode is damped, an inductor and a resistor in parallel are connected to the shunted PZTs. This leads to electrical equations of the form

$$\begin{bmatrix} L & -L \\ -L & L \end{bmatrix} \ddot{\mathbf{q}} + \begin{bmatrix} 0 & 0 \\ 0 & R \end{bmatrix} \dot{\mathbf{q}} + \begin{bmatrix} 0 & 0 \\ 0 & 0 \end{bmatrix} \mathbf{q} = \begin{Bmatrix} 0 \\ 0 \end{Bmatrix} \quad (3.91)$$

where L and R are the inductance and resistance respectively. These are then added to the structural finite element equations. The values of the inductance and resistance, determined using the method proposed by Wu (1998), are 199.4H/113.7k Ω , 8.888H/27.66k Ω , and 1.188H/16.38k Ω for bending modes 1, 2, and 3 respectively. The tip deflection as a function of frequency for the plate with mode 2 damped is plotted in Fig. 3.8 with that of the shorted plate. Next modes 1 and 2 are damped with the circuit shown in Fig. 3.9. The values of L_2' and C_2' are chosen such that $L_2' C_2' = 1/\omega_1^2$ and are assumed to be 22.516H and 1.00 μ F respectively. The values of R_2'' and

L_2'' , calculated using the multi-mode theory of Wu (1998), are $36.54\text{k}\Omega$ and 9.862H respectively.

This leads to the electrical equations given by

$$\begin{bmatrix} 0 & 0 & 0 & 0 & 0 \\ 0 & 0 & 0 & 0 & 0 \\ 0 & 0 & L_1 & 0 & 0 \\ 0 & 0 & 0 & L_2' & 0 \\ 0 & 0 & 0 & 0 & L_2'' \end{bmatrix} \ddot{\mathbf{q}} + \begin{bmatrix} R_1 & -R_1 & -R_1 & 0 & 0 \\ -R_1 & R_1 + R_2' & R_1 & 0 & -R_2' \\ -R_1 & R_1 & R_1 & 0 & 0 \\ 0 & 0 & 0 & 0 & 0 \\ 0 & -R_2' & 0 & 0 & R_2' \end{bmatrix} \dot{\mathbf{q}} + \begin{bmatrix} 0 & 0 & 0 & 0 & 0 \\ 0 & \frac{1}{C_2} & 0 & \frac{-1}{C_2} & 0 \\ 0 & 0 & 0 & 0 & 0 \\ 0 & \frac{-1}{C_2} & 0 & \frac{1}{C_2} & 0 \\ 0 & 0 & 0 & 0 & 0 \end{bmatrix} \mathbf{q} = \begin{bmatrix} 0 \\ 0 \\ 0 \\ 0 \\ 0 \end{bmatrix} \quad (3.92)$$

The resulting frequency response is shown in Fig. 3.10. This technique can be seen to result in a decrease in maximum tip deflection of over one order of magnitude. This versatile technique can also be extended to as many modes as one wishes to damp out.

Finally a comparison is made between the open circuited and short circuited mode shapes. As discussed above, the system can be reduced using its open circuited eigenvectors. However, it is desirable to estimate the nature of any resulting errors when this technique is applied to an electrical system where the short circuit mode shapes are more appropriate. Since the open and shorted eigenvectors are both normalized to the same mass matrix, the difference between the two can be directly calculated. Then to compare the deviation, the norm of the difference can be compared to the norm of the original eigenvector. The ratio of the 2-norms of

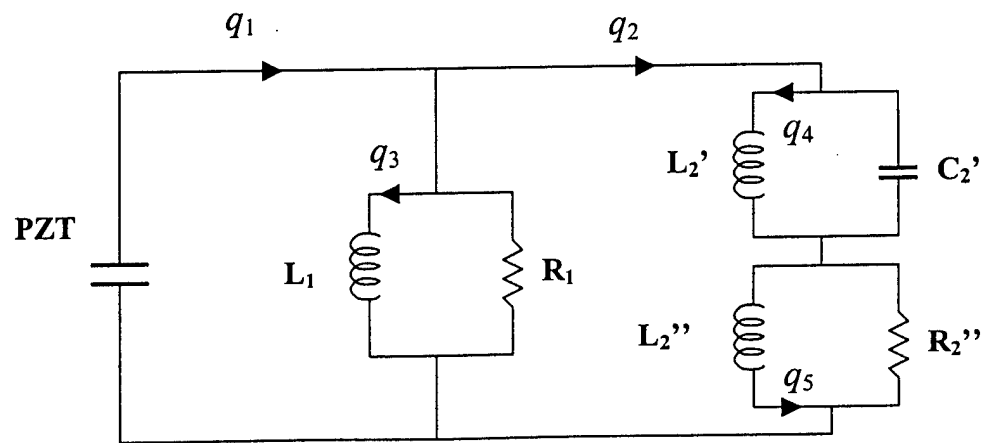


Fig. 3.9. Two mode damping circuit.

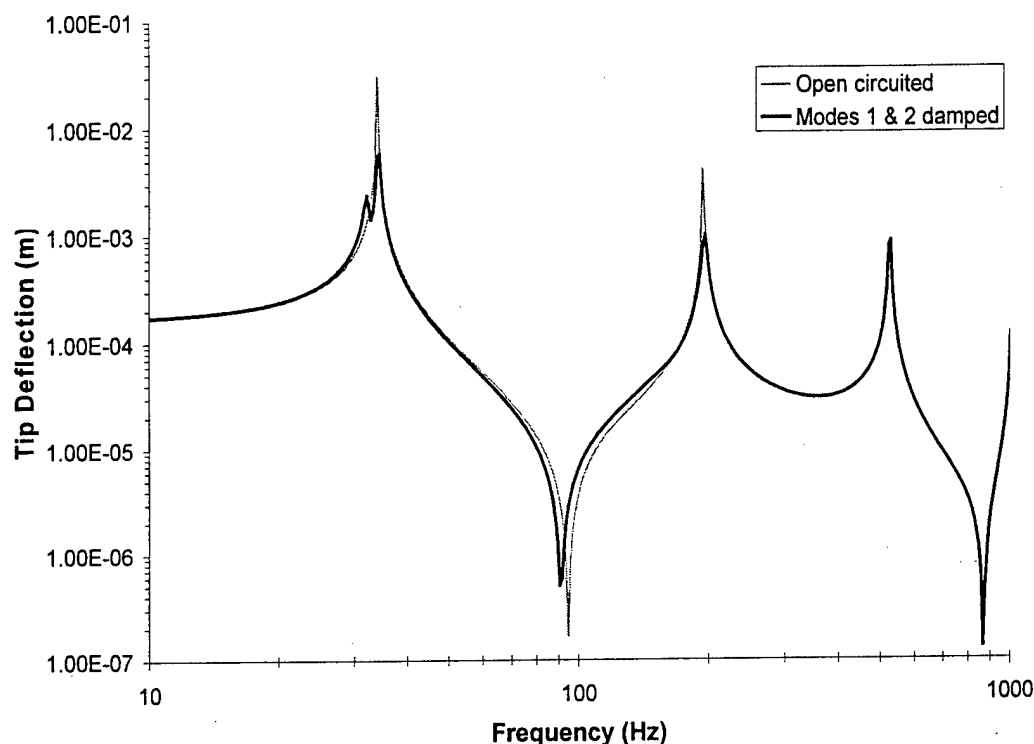


Fig. 3.10. Frequency response for aluminum plate with modes 1 and 2 damped.

the difference to the open circuit mode shape is found to be 1.79×10^{-5} , 4.53×10^{-5} , and 2.73×10^{-5} for the first three bending modes of the cantilevered aluminum plate use above. These very small differences are negligible when compared to the changes in natural frequency, which are on the order of one percent. Thus, the technique for using open circuit mode shapes for system reduction will likely yield good results in most practical problems.

3.3. Transient Analysis

Although the dynamic results shown thus far are useful for the study of smart structures, the ability to model the transient response of such structures is the most important and most difficult goal to achieve. Active control systems are often used to damp out transient vibrations using feedback control circuits, thus an accurate analysis of the control system requires an

accurate estimation of the dynamic response of the system. Also, damage detection schemes often use changes in the dynamic response of the structure to detect and localize damage. Thus, an accurate modeling technique is an invaluable tool in the design such systems. Having demonstrated the basic validity of the developed theory, it is desired to study its ability to accurately model the transient response of adaptive structural systems and compare the mechanical and electrical response with experimental results and other modeling techniques.

3.3.1. Newton-Raphson Method

The nonlinear transient analysis is conducted using Newmark-beta method with Newton-Raphson (N-R) iteration (Argyris and Mlejnek, 1991; Cook, et al., 1989; Bathe, 1996). The above system of dynamic equilibrium, Eq. (3.81), can be rewritten in the implicit form at time $(t + \Delta t)$ as follows

$$\mathbf{m} \mathbf{a}(t + \Delta t)^k + \mathbf{c}(t + \Delta t) \mathbf{v}(t + \Delta t)^k + \mathbf{k}(t + \Delta t) \Delta \mathbf{u}^k = \mathbf{f}(t + \Delta t) - \mathbf{R}(t + \Delta t)^{k-1} \quad (3.93)$$

where, \mathbf{m} is the time independent augmented mass matrix, $\mathbf{c}(t + \Delta t)$ is the augmented damping matrix at time $(t + \Delta t)$ and $\mathbf{k}(t + \Delta t)$ is the augmented stiffness matrix at time $(t + \Delta t)$. The vector, $\mathbf{f}(t + \Delta t)$, contains the externally applied nodal point loads, which is the right hand force vector in Eq(3.81) and the vector, $\mathbf{R}(t + \Delta t)^{(k-1)}$, contains nodal point forces equivalent to elemental stresses at time $(t + \Delta t)$ in $(k-1)^{\text{th}}$ iteration. The mechanical and electric displacements at the nodes are contained in the vector, \mathbf{u} .

The incremental nodal displacements at the k^{th} iteration of a particular time-step $(t + \Delta t)$ are defined for a given time step, Δt , as follows

$$\Delta \mathbf{u}^k = \mathbf{u}(t + \Delta t)^k - \mathbf{u}(t + \Delta t)^{k-1} \quad (3.94)$$

Using the trapezoidal rule, the following assumptions are made

$$\mathbf{u}(t + \Delta t) = \mathbf{u}(t) + \frac{\Delta t}{2} \{\mathbf{v}(t) + \mathbf{v}(t + \Delta t)\} \quad (3.95a)$$

$$\mathbf{v}(t + \Delta t) = \mathbf{v}(t) + \frac{\Delta t}{2} \{\mathbf{a}(t) + \mathbf{a}(t + \Delta t)\} \quad (3.95b)$$

This leads to the following forms

$$\mathbf{v}(t + \Delta t) = \{\mathbf{u}(t + \Delta t) - \mathbf{u}(t)\} \frac{2}{\Delta t} - \mathbf{v}(t) \quad (3.96a)$$

$$\mathbf{a}(t + \Delta t) = \frac{4}{(\Delta t)^2} \{\mathbf{u}(t + \Delta t) - \mathbf{u}(t)\} - \frac{4}{\Delta t} \mathbf{v}(t) - \mathbf{a}(t) \quad (3.96b)$$

For the k^{th} iteration of a particular time-step ($t + \Delta t$) substitution of Eq. (3.94) into Eqs. (3.96a,b) results in the following

$$\mathbf{v}(t + \Delta t)^k = \frac{2}{\Delta t} \{\mathbf{u}(t + \Delta t)^{k-1} + \Delta \mathbf{u}^k - \mathbf{u}(t)\} - \frac{4}{\Delta t} \mathbf{v}(t) \quad (3.97a)$$

$$\mathbf{a}(t + \Delta t)^k = \frac{4}{(\Delta t)^2} \{\mathbf{u}(t + \Delta t)^{k-1} + \Delta \mathbf{u}^k - \mathbf{u}(t)\} - \frac{4}{\Delta t} \mathbf{v}(t) - \mathbf{a}(t) \quad (3.97b)$$

Substitution of Eqs. (3.97a,b) into Eq. (3.93) yields the iterative form

$$\bar{\mathbf{k}} \Delta \mathbf{u}^k = \mathbf{f}(t + \Delta t) - \mathbf{R}(t + \Delta t)^{k-1} - \mathbf{m} \mathbf{a}_1^{k-1} - \mathbf{c}(t + \Delta t) \mathbf{a}_2^{k-1} \quad (3.98)$$

where

$$\mathbf{a}_1^{k-1} = \left[\frac{4}{(\Delta t)^2} \{\mathbf{u}(t + \Delta t)^{k-1} - \mathbf{u}(t)\} - \frac{4}{\Delta t} \mathbf{v}(t) - \mathbf{a}(t) \right] \quad (3.99a)$$

$$\mathbf{a}_2^{k-1} = \left[\frac{2}{\Delta t} \{\mathbf{u}(t + \Delta t)^{k-1} - \mathbf{u}(t)\} - \mathbf{v}(t) \right] \quad (3.99b)$$

$$\bar{\mathbf{k}} = \frac{4}{(\Delta t)^2} \mathbf{m} + \frac{2}{\Delta t} \mathbf{c}(t + \Delta t) + \mathbf{k}(t + \Delta t) \quad (3.99c)$$

$$\mathbf{R}(t + \Delta t)^{k-1} = \mathbf{k}(t + \Delta t) \mathbf{u}(t + \Delta t)^{k-1} \quad (3.99d)$$

This results in a time integration method that can be iterated at each time step to provide accurate prediction of the transient response of the system.

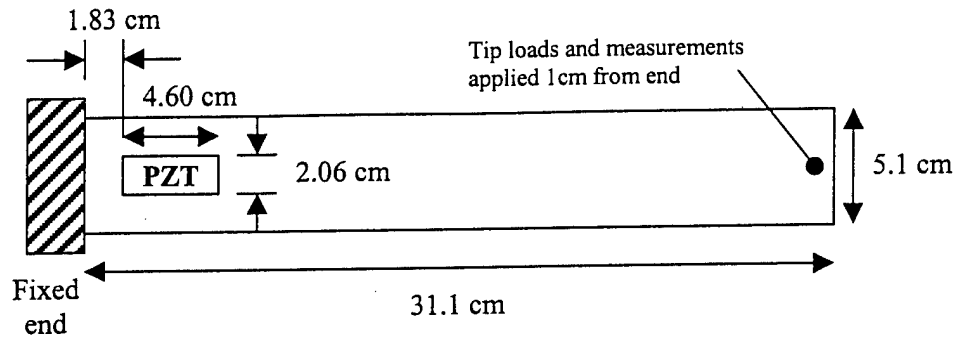


Fig. 3.11. Cantilever plate layout.

3.3.2. Results

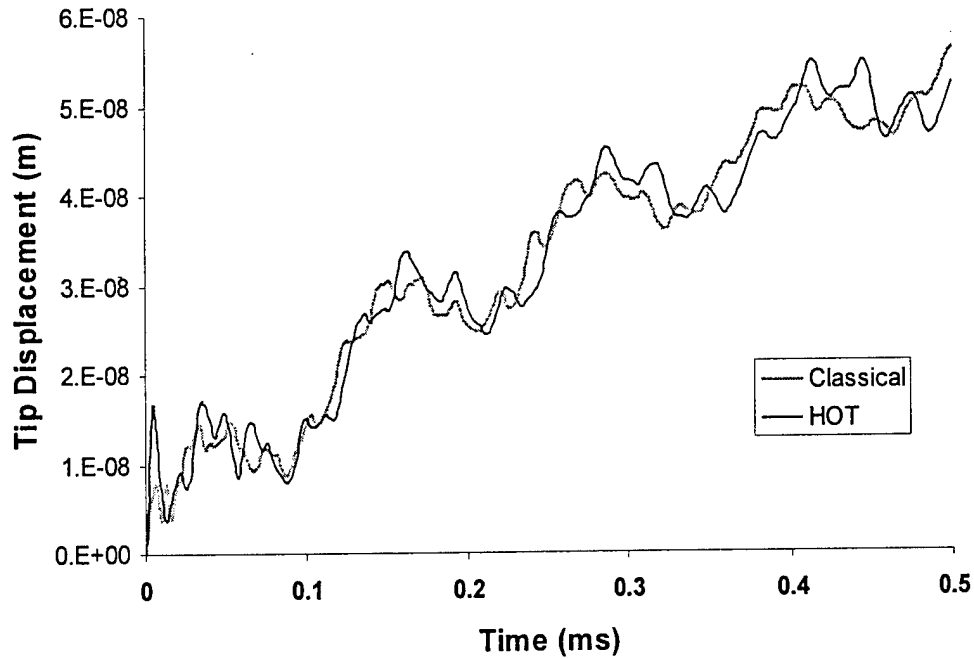
The developed model is used to calculate the response of a composite plate with surface bonded actuators subjected to impulse loading. The objective is to demonstrate the nature and magnitude of errors that exist when simpler approaches are used. First, a comparison is made between the response predicted by the refined higher order laminate theory and the classical plate theory. Then the difference between the coupled piezoelectric-mechanical model and the uncoupled model is examined.

The plate under consideration is clamped at one end with a cantilevered section 31.1cm long by 5.1cm wide. The plate is a graphite-epoxy laminate with sixteen plies of 0.137mm ply thickness. A variety of ply stacking sequences are considered, including cross-ply as well as balanced and unbalanced angle-ply lay-ups. A piezoelectric patch is bonded to the upper surface of the plate as shown in Figure 3.11. The patch is made of PZT-5H with a thickness of 0.25mm. The material properties for the graphite-epoxy and PZT are listed in Table 3.6.

Table 3.6.

List of material properties used for transient analysis.

Property	Graphite-epoxy	PZT-5H
E_1 (GPa)	372.0	60.6
E_2 (GPa)	4.12	60.6
ν_{12}	0.275	0.29
ν_{23}	0.42	0.48
G_{12} (GPa)	3.99	23.49
G_{23} (GPa)	3.6	22.99
ρ (kg/m ³)	1788.5	7500
d_{31} and d_{32} (nm/V)	-	-0.274
d_{24} and d_{15} (nm/V)	-	0.741
χ_{33}^T (nC/m)	-	30.1

Fig. 3.12. Tip displacement for $[0^\circ, 90^\circ]_{4s}$ laminate ($L/h=142$) under $1\mu s$ impulse loading.

3.3.2.1 Higher order versus classical plate theory

First, a comparison is made between the refined higher order laminate theory and the classical plate theory. A laminate stacking sequence of $[0^\circ, 90^\circ]_{4s}$ is considered first, with the

PZT left open circuited. This laminate has a ratio of plate length to thickness of 142, making this a relatively thin plate. The plate is modeled with the refined higher order laminate theory, which includes the effects of transverse shear, as well as with the classical plate theory, which neglects transverse shear. All other aspects of the modeling are identical in both cases. The plate is subjected to a 5-Newton, $1\mu\text{s}$ impulse point load at the tip. The analysis is performed for both cases with a $1\mu\text{s}$ time step. Figure 3.12 shows the resulting tip displacement obtained using the two models. The difference between the higher order theory and the classical theory is modest, but noticeable during the short time interval analyzed, even for this thin laminate. By including transverse shear stress, the refined higher order theory results in a model with lower natural frequencies than those predicted by the classical plate theory. This reduction in natural frequencies is due to the fact that during vibration the plate undergoes not only pure bending, but also deformation in the form of out-of-plane shear. The bending modes are all composed of both

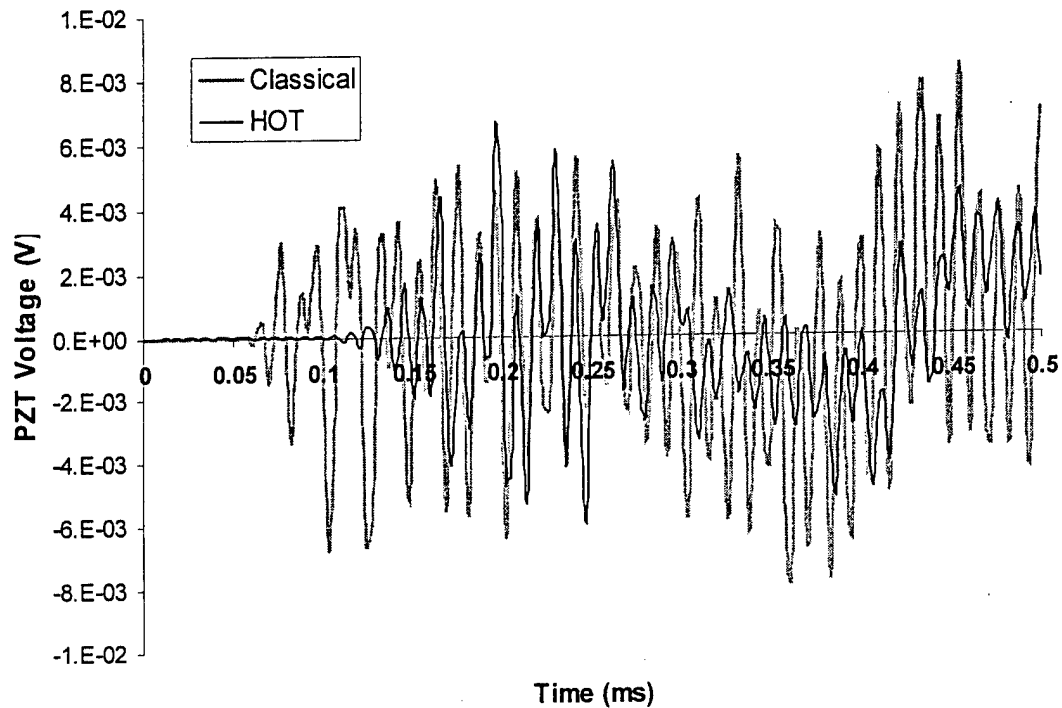


Fig. 3.13. Sensor output for $[0^\circ, 90^\circ]_{4s}$ laminate ($L/h=142$) under $1\mu\text{s}$ impulse loading.

forms of deformation and, thus, models which do not include both are too stiff. The effects are not only more significant for thicker laminates, but also for the higher frequency modes, and this difference in frequencies can be seen in Figure 3.12. Figure 3.13 shows the voltage output from the PZT sensor during the impulse loading. A very significant difference in voltage output is observed between the two plate theories. Although the shape of the response is very similar, the magnitude of the signal differs significantly. This is because at these high frequencies the output of the coupled piezoelectric-mechanical theory is very sensitive to changes in the strain field of the vibrational waves than mode across the sensor.

Next, the same plate is analyzed under a 1-Newton, $5\mu\text{s}$ impulse point load at the tip. The time step for the transient analysis is $5\mu\text{s}$, so that a longer time segment could be examined. The tip displacement for the higher order and classical plate theories is shown in Figure 3.14 and the sensor output is shown in Figure 3.15. When a longer time step is used the differences between the two theories are much less significant for the thin plate, because the natural

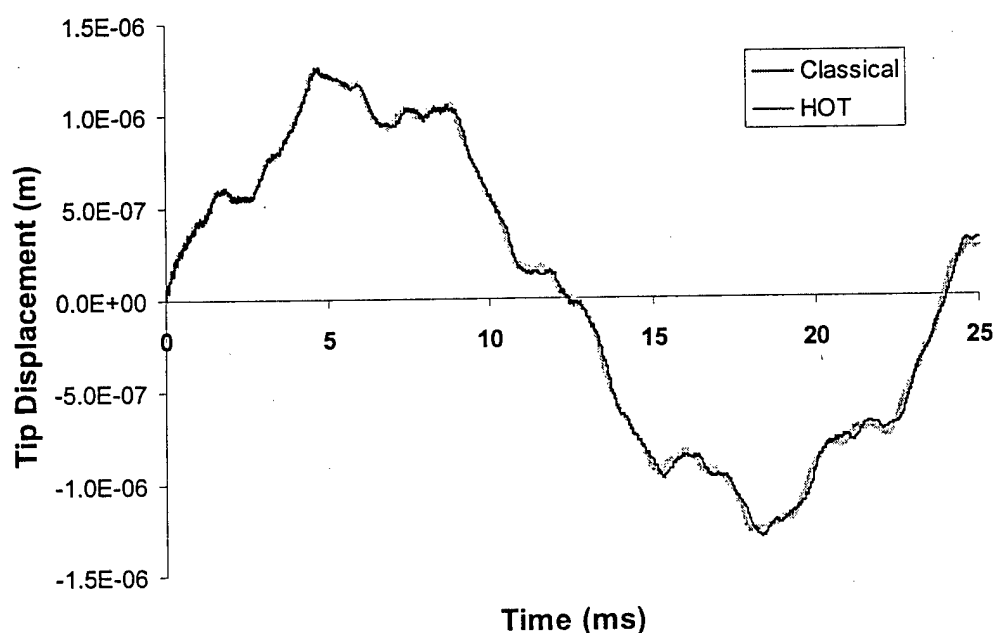


Fig. 3.14. Tip displacement for $[0^\circ, 90^\circ]_{4s}$ laminate ($L/h=142$) under $5\mu\text{s}$ impulse loading.

frequencies associated with the lower order modes predicted by the two plate theories are quite similar. Note that in this case the charge flow from the PZT is measured for sensor output. It can be seen that the differences in the higher frequencies affect sensor output to a greater degree than tip displacement.

An increase in plate thickness increases the difference in the response predicted by the higher order theory and the classical plate theory. This is shown in Figure 3.16, which depicts the tip response for a $[0^\circ, 90^\circ]_{4s}$ laminate. The ratio of plate length to thickness is 28.4 for this case, making this a moderately thick plate. The impulse length and time step used in this case are both $1\mu s$. By increasing plate thickness differences are observed even in the low frequency modes predicted by the two plate theories. This results in sizable differences in plate deflections.

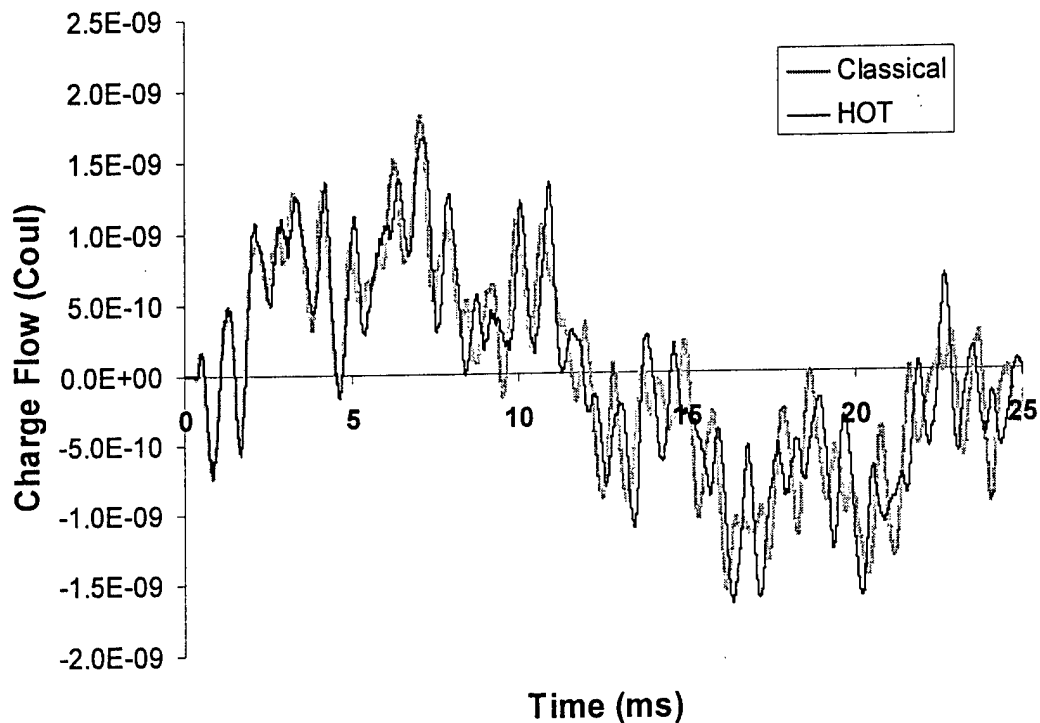


Fig. 3.15. Sensor output for $[0^\circ, 90^\circ]_{4s}$ laminate ($L/h=142$) under $5\mu s$ impulse loading.

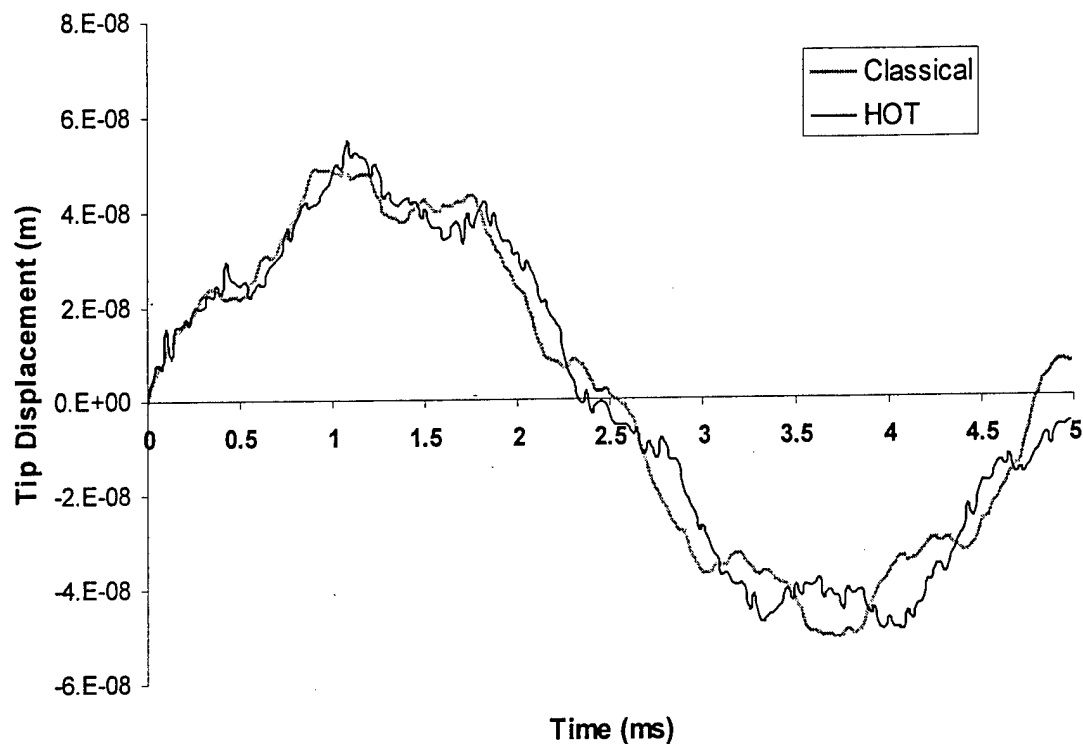


Fig. 3.16. Tip displacement for $[0^\circ_s, 90^\circ_s]_{4s}$ laminate ($L/h=28.4$) under $1\mu s$ impulse loading.

3.3.2.2 Coupled versus uncoupled piezoelectric theory

Next a comparison is made between the coupled and the uncoupled piezoelectric models. The plate with $[0^\circ, 90^\circ]_{4s}$ stacking sequence is considered. The plate is subjected to a 1-Newton, $5\mu s$ impulse point load at the tip and a $5\mu s$ time step is used for the transient analysis. The PZT is open circuited and voltage is measured for sensor output. The response is calculated using both the coupled theory presented in this work as well as the traditional uncoupled approach. The resulting tip displacement is shown in Figure 3.17 for both approaches. Only slight differences between the two models are observed in this case. This is due to the relatively small size of the PZT patch and its limited contribution to the overall plate stiffness. This difference is expected to be larger for thicker PZT patches.

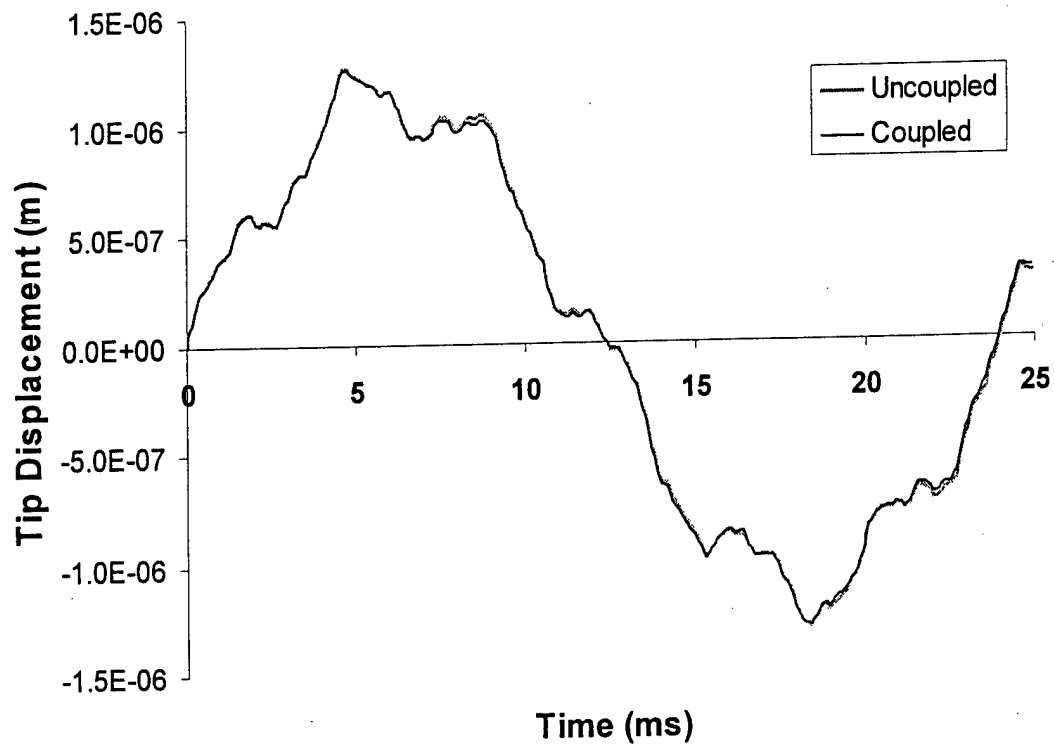


Fig. 3.17. Tip displacement for $[0^\circ, 90^\circ]_{4s}$ laminate under impulse loading.

Figure 3.18 shows the charge flow of the sensor for both cases. Here it can be seen that the coupled theory predicts dramatically different results from the uncoupled approach, even though the displacements are shown to be similar. The reason for the large differences in the electrical response is due to a combination of two factors. The first is the fact that the uncoupled theory assumes that the electric field is constant over the entire area of the PZT. During impulse loading high frequency bending waves travel across the length of the plate, as shown in Figure 3.19. As these high frequency waves move across the PZT, the piezoelectric material is subjected to areas of local compression and tension. As a result, the electric displacement is positive in some local areas and negative in others as shown in Figure 3.20. The net charge output is thereby reduced since charge merely flows from one region of the patch to another. When the PZT is open circuited, the charge flow within the PZT still occurs making the voltage output very sensitive to local strain. As shown in Figure 3.21, the strains at the two ends of the PZT are very

dissimilar during the impulse loading. Thus, there exists a continuously changing strain gradient across the PZT patch, which leads to the difference in results predicted by the coupled and uncoupled models. Figure 3.22 presents the output if the voltage of the PZT is measured, as

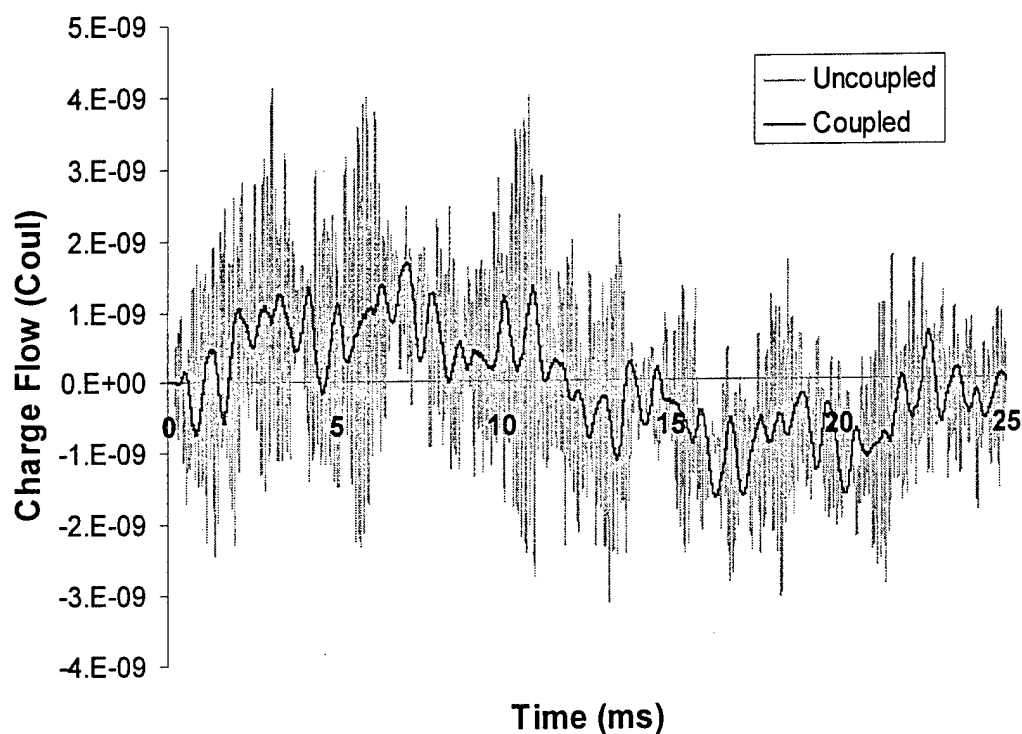


Fig. 3.18. Sensor charge flow for $[0^\circ, 90^\circ]_{4s}$ laminate under impulse loading.

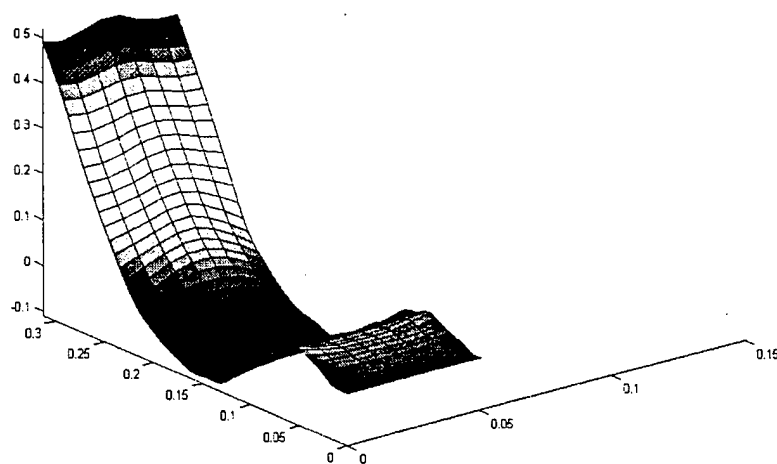


Fig. 3.19. Plate displacement at $t=73.95 \mu s$ during impulse tip loading.

opposed to the charge flow. Again the coupled theory predictions greatly differ from the uncoupled approach and the high frequency signal can be seen to be much more prominent when voltage is measured.

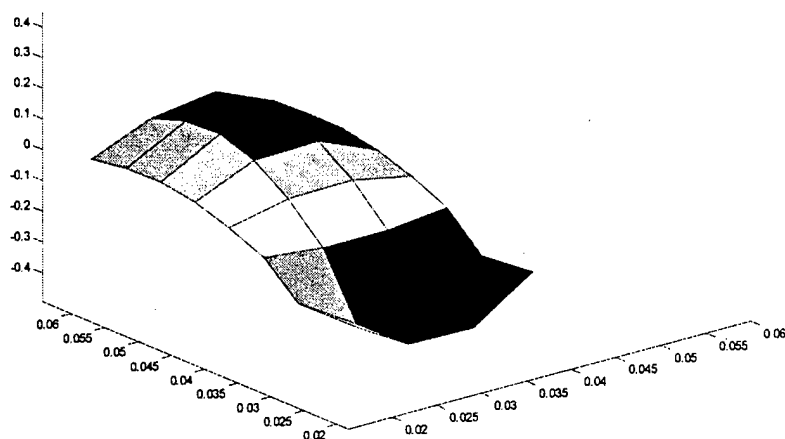


Fig. 3.20. Electric displacement at $t=60.45 \mu\text{s}$ during impulse loading.

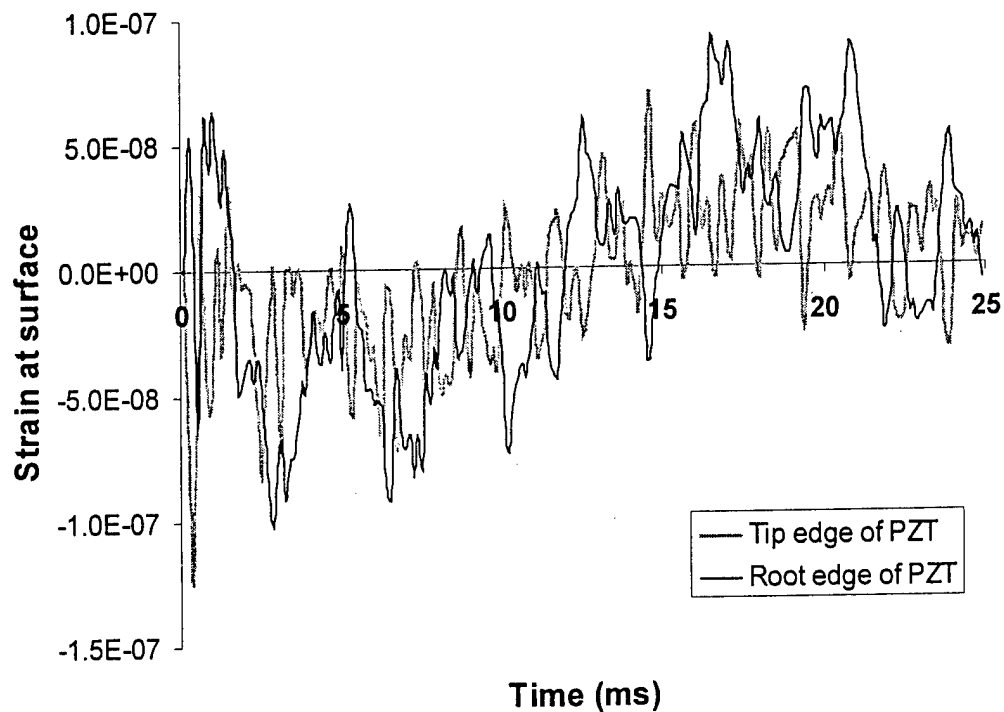


Fig. 3.21. Longitudinal strain at the plate surface on both ends of the PZT patch.

The second factor that creates differing results between the coupled and uncoupled approaches is the existence of electrical inductance, both in the electrical circuit and within the piezoelectric material itself. This inductance acts like mass in a mechanical system and prevents instantaneous changes in the charge flow of the electrical system. The magnitude of the electrical signal created by high frequency vibrations in the piezoelectric material are thus limited in magnitude, just as mass limits amplitude of vibrations induced by forces in a mechanical system. The uncoupled approach is incapable of including inductance effects, thus the high frequency component of the electrical sensor output will always be overpredicted when compared to a physical system. The coupled model has the ability to include inductance that exists in the physical system. A typical 1m long coax cable has inductance on the order of $0.3\mu\text{H}$ and this can be included by use of Eq. (3.80). The piezoelectric device itself also has some inductance which affects not only the net output of the device, but also the charge flow from one area of the

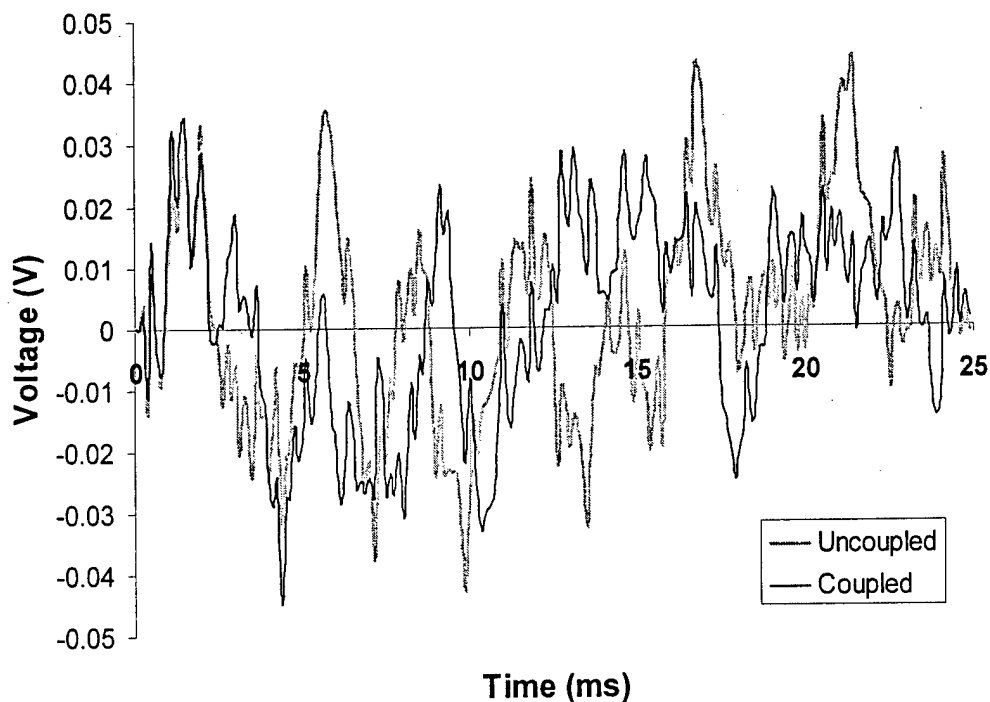


Figure 3.22. Sensor output for $[0^\circ, 90^\circ]_{4s}$ laminate under impulse loading.

actuator to another. This inductance can be included in Eq. (3.75) by addition of positive values along the diagonal of the section of the mass matrix corresponding to the piezoelectric electric displacement. The exact value for the internal inductance is very difficult to quantify and comparison with experimental data seems to be the best method for obtaining these values.

3.3.3. Experimental comparison

To validate the model and verify the conclusions made from comparison of the coupled theory with the uncoupled approach, a set of experiments was performed. The objective of these experiments was to provide a set of transient sensor outputs for a well-defined model and compare these directly with the results predicted by the developed model.

The test specimen used was a cantilevered plate with two piezoelectric patches bonded to the surface. The plate was made from 3.18mm thick Aluminum 2024-T3 and the plate geometry

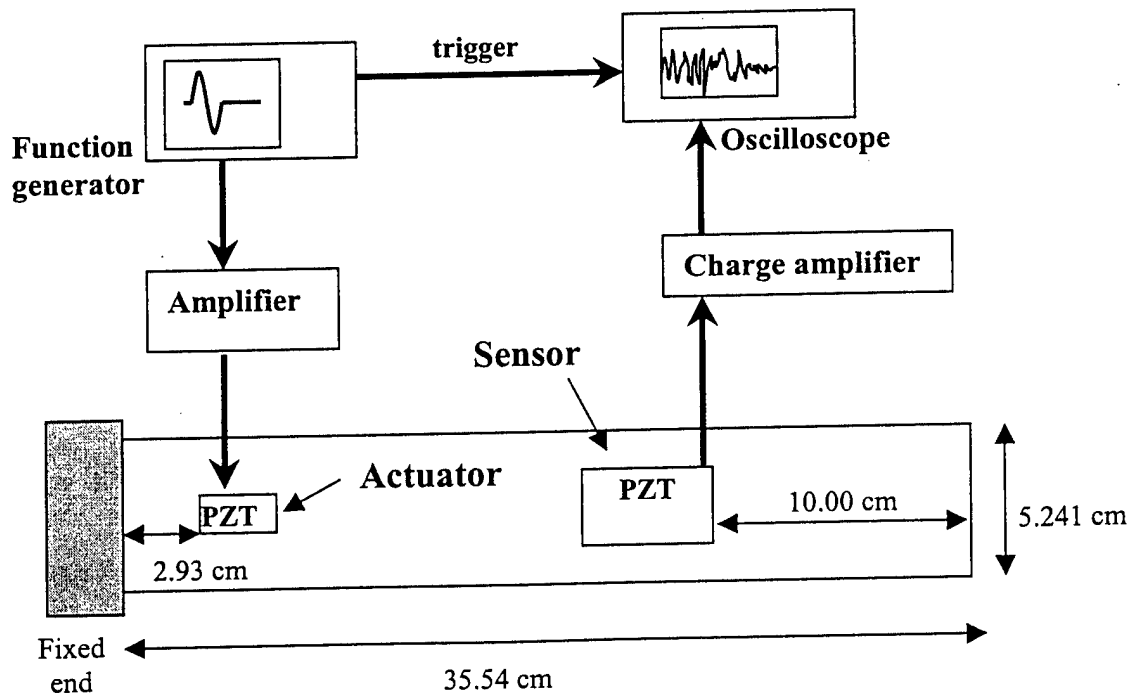


Fig. 3.23. Experimental setup and plate geometry for transient analysis.

is that shown in Figure 3.23. The small piezoelectric patch at the root was a custom ACX actuator with wafer dimensions of 1.27cm length, 0.635cm width and 0.25mm thickness. The larger piezoelectric patch was an ACX QP-10N actuator with wafer dimensions of 4.597cm length, 2.057cm width and 0.25mm thickness. Both devices were made of PZT-5A with a polyamide coating. The material properties for the aluminum and the piezoelectric devices are shown in Table 3.7.

The small patch at the root was used as an actuator to induce vibration in the plate, while the larger patch was used as a sensor. To simulate an impulse loading in the plate, a single cycle of high frequency voltage was applied to the actuator. The single cycle voltage was generated by a function generator set operate in burst mode and create a 3.75V signal once every two seconds. The input voltage was then amplified to a 75V-peak signal that was sent to the actuator. This signal is illustrated in Fig. 3.24.

The sensor output was measured using two different methods. First the sensor was connected to a charge amplifier that converted to the charge flow of the device into a voltage signal that was measured and analyzed using an oscilloscope. This method allowed measurement of the charge output of the piezoelectric device for comparison with the developed model. Next,

Table 3.7.

Material properties for experimental comparison.

Material property	Aluminum	PZT
E (Gpa)	68.5	60.6
ν	0.326	0.29
G (Gpa)	25.83	23.49
ρ (kg/m ³)	2784	7500
d_{31}, d_{32} (m/V)	n/a	-274×10^{-12}
d_{24}, d_{15} (m/V)	n/a	741×10^{-12}
e_3^S (F/m)	n/a	3.01×10^{-9}

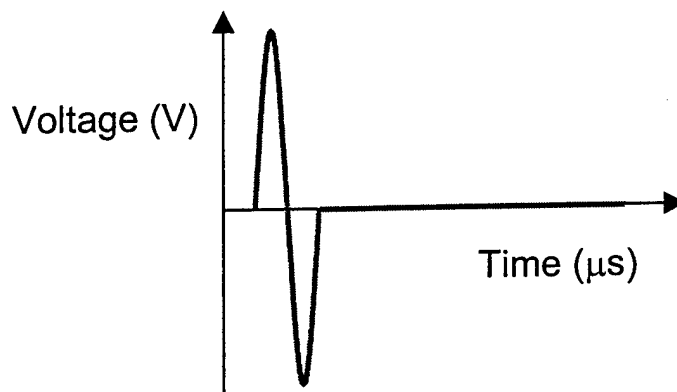


Fig. 3.24. Input voltage used to simulate impulse loading.

the sensor was connected directly to the oscilloscope and the voltage output was measured.

Sensor output was measured for a range of input frequencies. The frequency of the single cycle voltage input allowed control of the duration of the impulse. Higher frequency inputs acted like shorter duration impulse loads and excited higher frequency responses from the system. This method proved to be much more controlled than mechanical impulse loads and the output signals for the impulses were very repeatable. To minimize any effects of noise and deviation between individual impulses, the oscilloscope was set to provide an averaged output using sixteen impulse signals.

The charge output for 10kHz, 25kHz and 50kHz input frequencies is shown in Fig. 3.25. The important aspect to be noted from these results is that the overall shape of the output is the same for all three frequencies. The effect of electrical inductance discussed above can be clearly seen, in that the magnitude of the very high frequency component of the output is much smaller than the lower frequency component, which governs the overall shape of the output. Although the higher frequency input voltages provide more high frequency excitation of the system, the magnitude of the electrical signal created by this component is limited due to the electrical inductance and the fact that the high frequency vibrations cause less net charge flow.

Figure 3.26 shows the voltage output for 1kHz, 10kHz and 25kHz input frequencies. It is clear that the voltage is more sensitive to high frequency vibration and less affected by the electrical inductance than the case when sensor charge flow is used. This is reasonable since although the oscilloscope is not a true open circuit it has a $1\text{M}\Omega$ internal resistance that limits the electrical system to very small net charge flows. Less charge flow in turn implies less effect from inductance, but charge flow within the piezoelectric device during high frequency vibration is still affected.

The developed analysis is now used to model the system described above. A finite element mesh with 85 by 9 elements was used for the plate resulting in 860 nodes. The system had 6020 mechanical degrees of freedom, 8 nodal electrical displacements for the small actuator and 48 nodal electrical displacements for the sensor. The material properties listed in Table 3.7 are used to model the system. The sensor charge flow predicted by the model for 10kHz and 25kHz input frequencies are shown in Figs. 3.27 and 3.28. The output shows good correlation between the coupled model and the experimental results from Fig. 3.25. The overall shape of the signals are very similar and similarities between the two frequencies are replicated by the model. This result is in contrast to the predicted response using the uncoupled approach seen in Fig. 3.29. The lack of internal inductance causes the high frequency components of the signal to dominate the sensor output. The results from the coupled approach and the experimental results are not identical and a more valuable comparison can be made by examining the response in the frequency domain. Figure 3.30 shows the frequency content of the response for the coupled and uncoupled approaches. Both models correlate well at the lower frequencies, but the uncoupled model has a large amount of high frequency content as discussed above. At higher frequencies, significant differences in response between coupled and uncoupled models is observed. The results from the coupled model also deviates from the experimental results. This is a result of the limitations of the finite element method and the mesh size used in this model. The variations

observed are not unreasonable considering the difficulties associated with accurate modeling of high frequency structural dynamics. Figure 3.31 shows a comparison between the classical and higher order plate models. Both results were computed using the coupled theory and show similar response curves. The primary difference between these two models appears in the exact locations of the response peaks, since the classical plate theory specify lower natural frequencies compared to the higher order theory. Once again, deviations in response between experiments and models are observed at higher frequencies due to the reasons stated above. However, the relative merit of the two theories is difficult to establish from these results.

Next sensor voltage was calculated using the developed model. The sensor voltage predicted by the model for 1kHz and 10kHz input frequencies are shown in Figs. 3.32 and 3.33. The output is similar to the experimental data, but is less accurate than the predicted charge flow. The reason for this difference is the difficulty in accurately characterizing the electrical system. The oscilloscope used to measure the voltage experimentally is not an ideal voltage-measuring device. The actual circuit measures the voltage across a large resistor and the circuit has a small amount of charge flow, contrary to the zero net charge flow assumed by the piezoelectric boundary conditions. Also, the charge flow within the PZT becomes extremely important in determining the output voltage. A more detailed characterization of the internal inductance and resistance of the piezoelectric device and voltage measuring circuit must be used to accurately model the voltage response of an adaptive structure. The sensor charge flow is less sensitive to these effects, thus making it easier to obtain an accurate model.

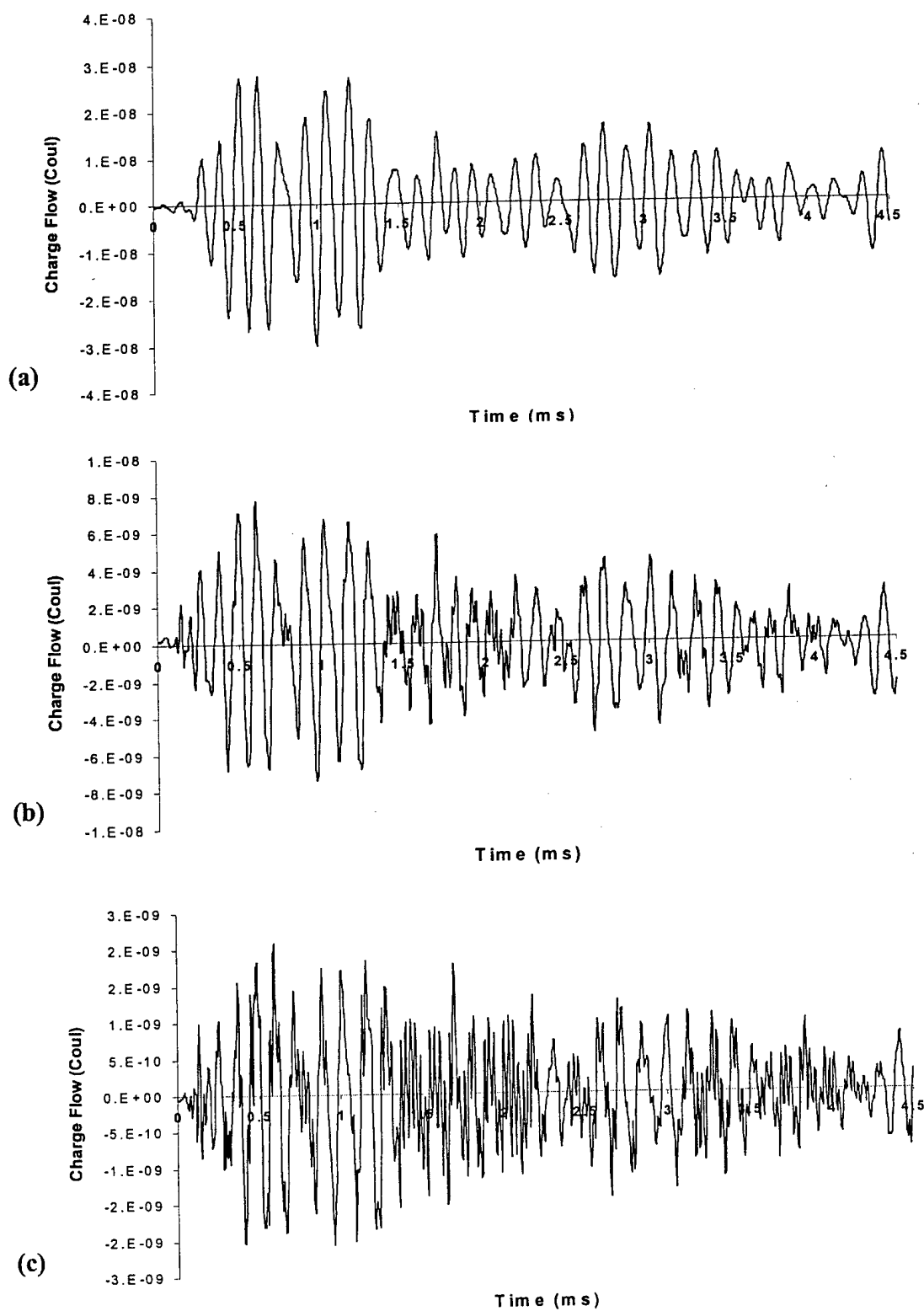


Fig. 3.25. Sensor charge flow for input frequencies of (a) 10kHz, (b) 25kHz and (c) 50kHz.

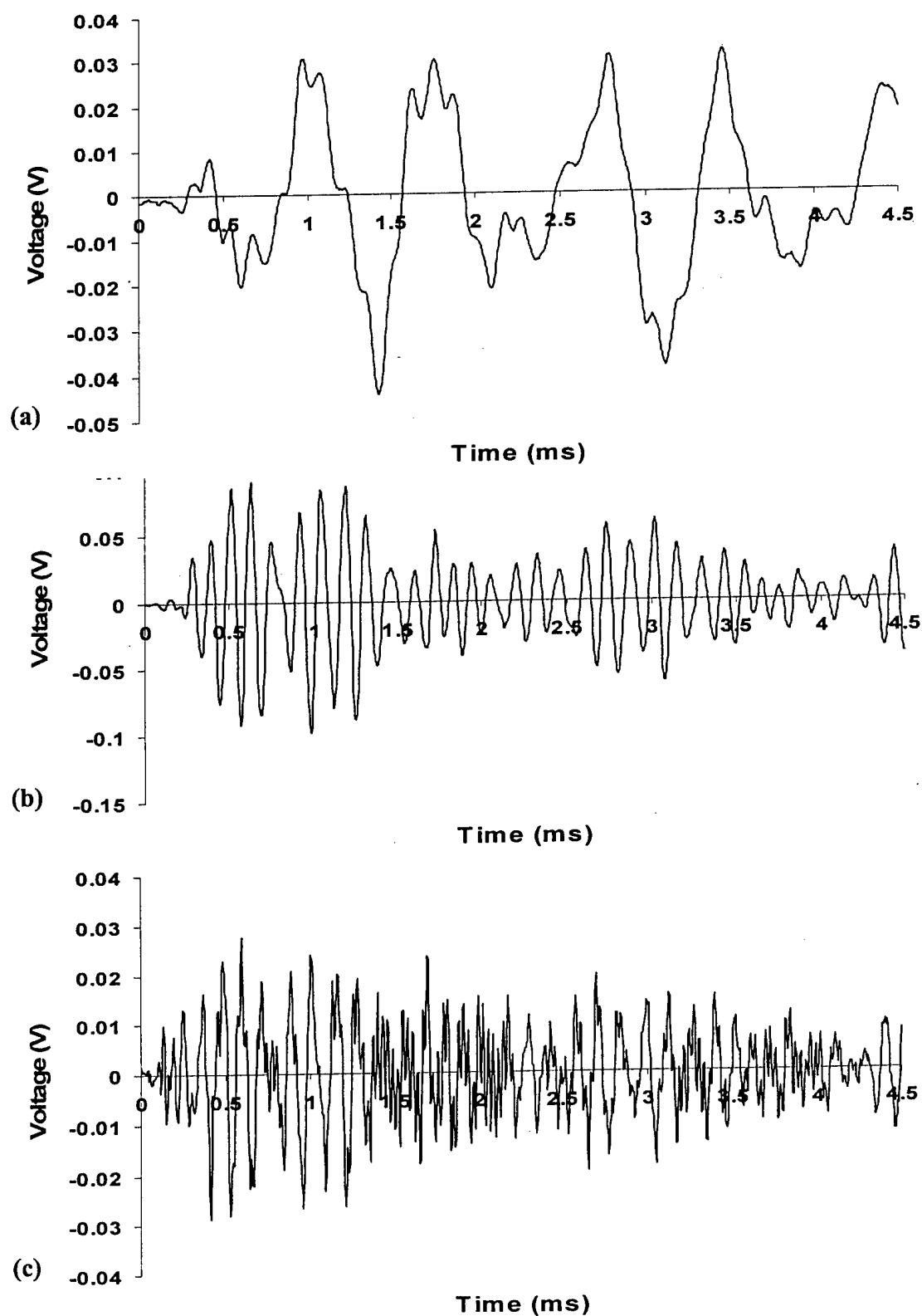


Fig. 3.26. Sensor voltage for input frequencies of (a) 1kHz, (b) 10kHz and (c) 25kHz.

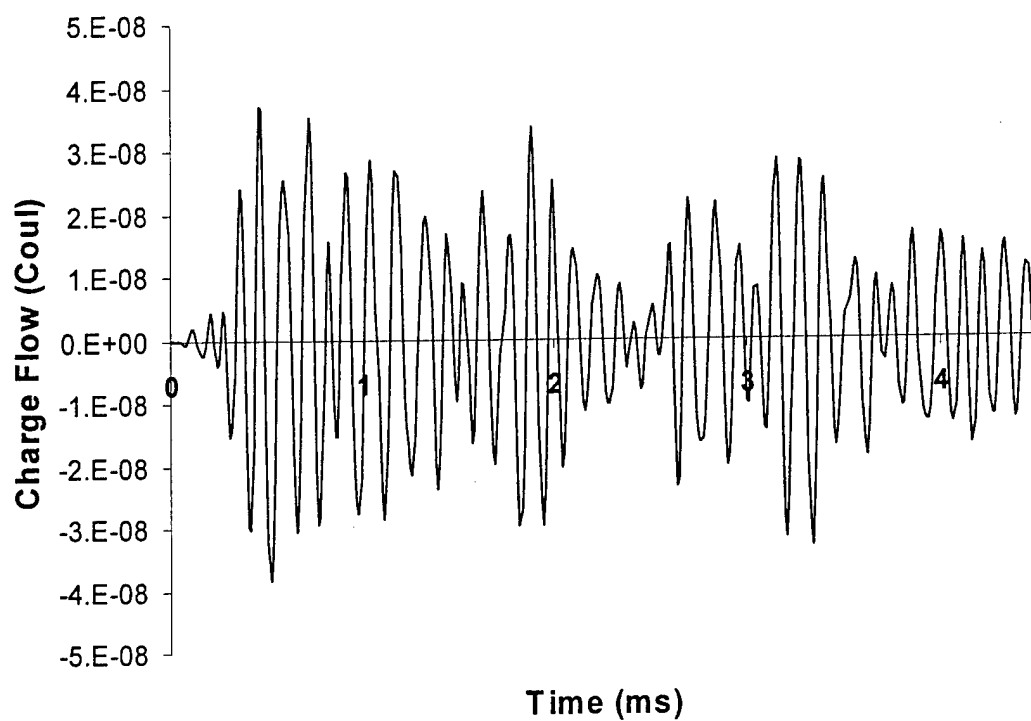


Fig. 3.27. Predicted response for 10kHz input frequency.

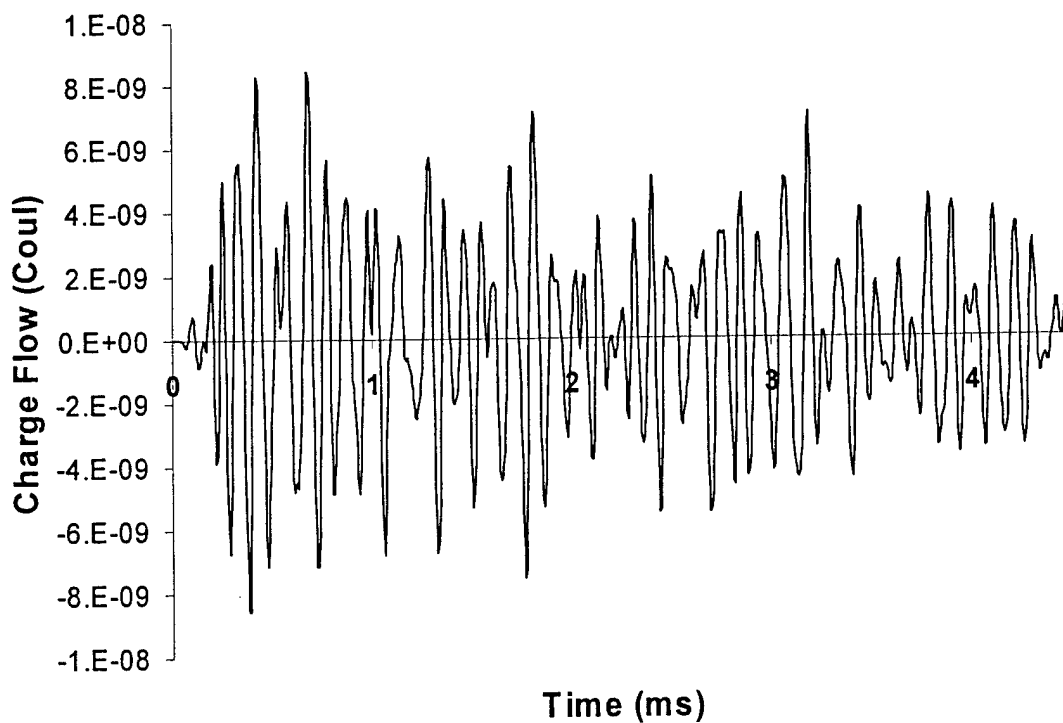


Fig. 3.28. Predicted response for 25kHz input frequency.

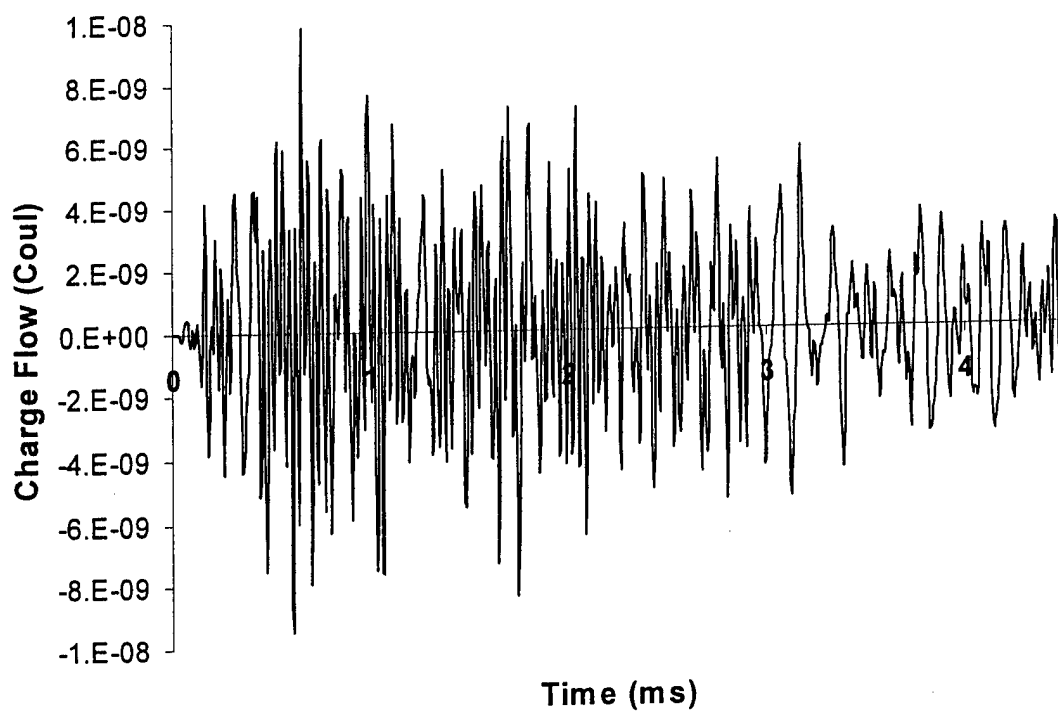


Fig. 3.29. Uncoupled response for 25kHz input frequency.

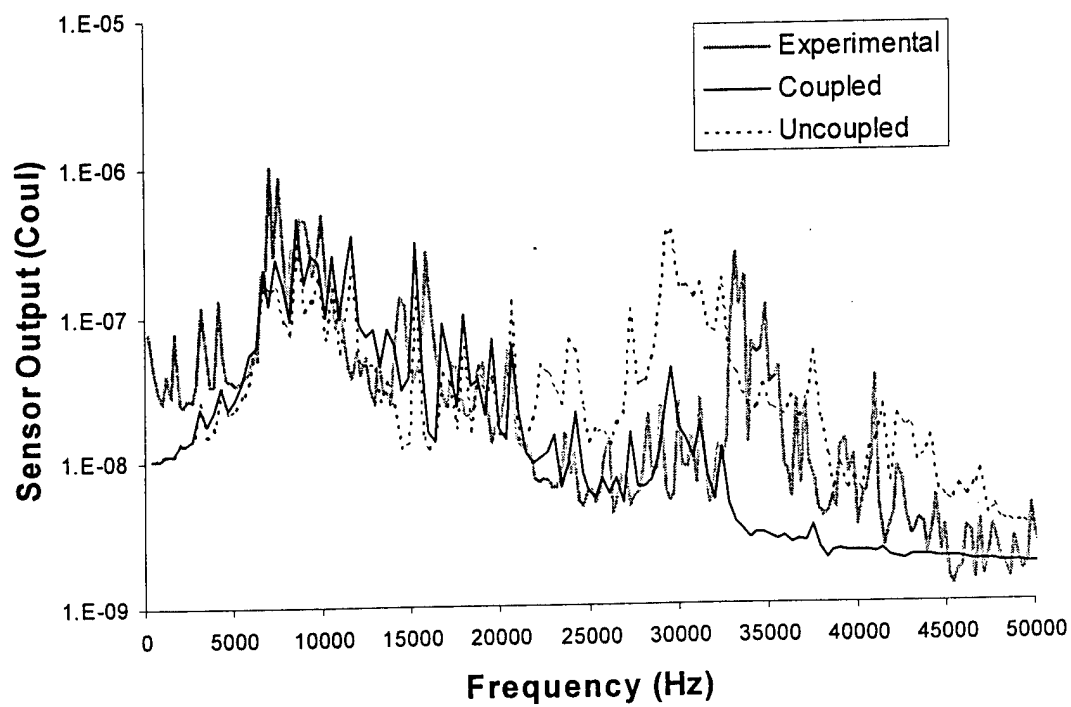


Fig. 3.30. Frequency domain comparison between coupled and uncoupled models for 25kHz input frequency.

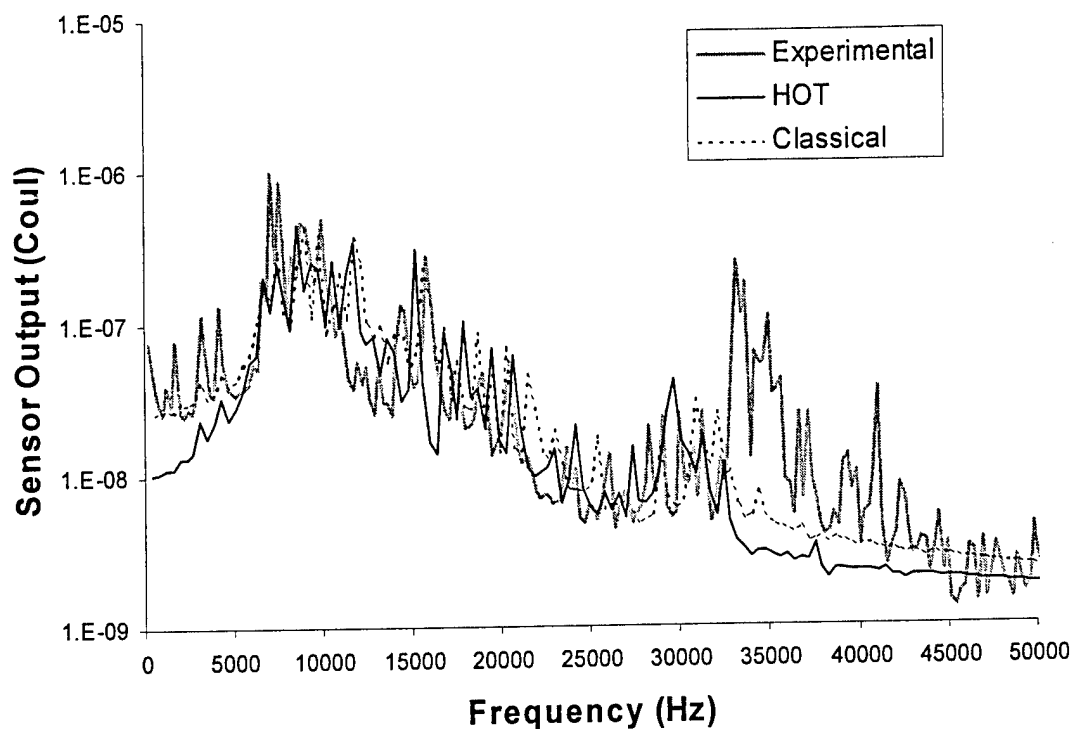


Fig. 3.31. Comparison of classical and higher order plate theories for 25kHz input frequency.

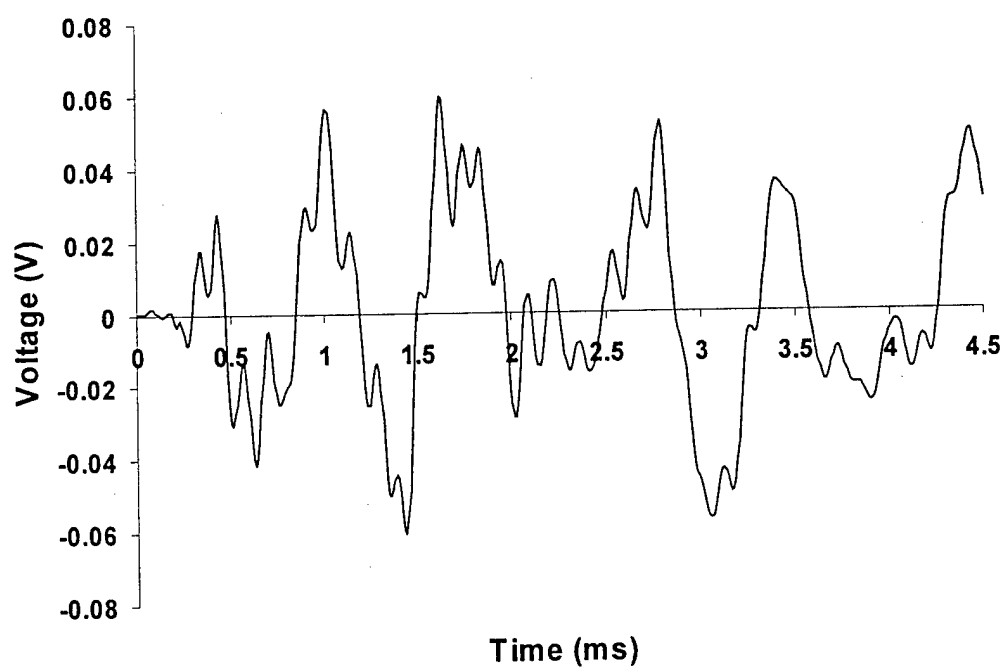


Fig. 3.32. Predicted response for 1kHz input frequency.

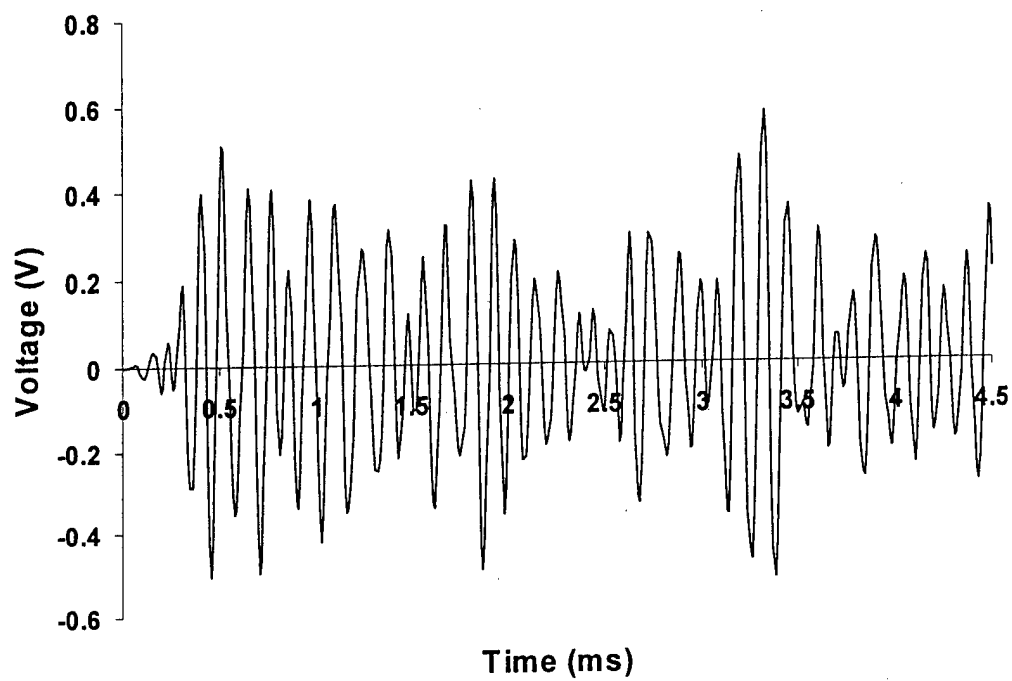


Fig. 3.33. Predicted response for 10kHz input frequency.

4. Delamination Modeling in Composite Laminates

Delamination occurs when a region of composite material becomes debonded from the layers below it. Delamination is known to affect not only the compressive strength of composite laminates, but also the dynamic characteristics of a composite structure. Since adaptive structural systems using piezoelectric patches are often used to detect and localize damage, such as delamination, the developed theory is extended to include the modeling of delamination. The primary goal of this investigation is to study the effects of delamination on the system response as opposed to predicting delamination growth. The response that is examined is not just the mechanical response, but also the electrical response that includes the sensor signal. Accurate prediction of the sensor signal will allow future damage detection studies to be more reliable.

When delamination occurs, a thinner sublaminates is formed above and below the region of delamination. The overall method for delamination modeling used in this work is to model each individual sublaminates as a separate plate and then join the sublaminates together to represent the entire plate. During plate vibration the possibility exists for the individual sublaminates to contact or impact each other, so a method for analyzing transient response that includes this contact is implemented. During transient analysis this contact/impact can cause numerical instabilities, thus a discontinuous time integration method is used for modeling the transient response of the structure. The resulting model is then used to study the effect of delamination on the response of adaptive composite structures.

4.1. Modeling

To include the presence of delamination the laminate theory developed in the previous chapter must be modified to model the multiple sublaminates in the region of delamination. This requires modification of the higher order displacement field and also selection of a method for

joining the sublaminates together at their boundaries with the undamaged host structure. In this section these issues are addressed and the model including delamination is developed. It should be noted that delamination growth is not considered in this work.

4.1.1. Higher Order Theory with Delamination

As discussed in the previous chapter, the refined higher order laminate theory provides a convenient and accurate method for modeling laminates and including the effect of transverse shear. Transverse shear becomes very important in moderately thick plates, and as a result, classical plate theory under predicts deformation due to out-of-plane loads and over predicts natural frequencies for the bending of plates. Delamination creates smaller sublaminates within the host structure. Although these sublaminates are thinner than the undamaged laminate, they are often relative small in size and it is possible that the sublaminates will have a higher relative thickness that the undamaged laminate. Thus, transverse shear will also play an important role for accurate modeling of local vibration modes and the higher order laminate theory is still an effective tool for addressing transverse shear effects.

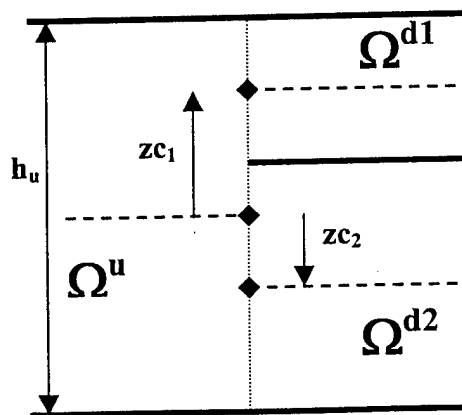


Fig. 4.1. Relationship between the finite element mesh of the sublaminates and the undelaminated regions of the plate.

To incorporate delamination, the structure is divided into regions, as seen in Fig. 4.1 and the higher order displacement equations are applied to each region (Ω^r $r = u, d1, d2$). It must be noted that the refined higher order plate theory developed in the previous chapter assumed that the out-of-plane coordinate, z , was referenced from the midplane of the laminate. The assumption that $z=0$ corresponded to the laminate midplane and that $\pm h/2$ corresponded to the surfaces of the plate allowed the simplification into the form presented in Eqs. (3.32). Assuming that the midplane of the original undelaminated structure corresponds to $z=0$, then the sublaminates formed by the delamination are offset from the original reference point. This introduces eccentricity in the plate theory and Eqs. (3.32) need to be modified to account for this. The displacement field of Eqs. (3.32) now assumes the following form

$$\mathbf{u}_1^r = u^r + (z - c^r) \left(\psi_x^r - \frac{\partial w^r}{\partial x} \right) - \frac{4(z - c^r)^3}{3h^2} \psi_x^r \quad (4.1a)$$

$$\mathbf{u}_2^r = v^r + (z - c^r) \left(\psi_y^r - \frac{\partial w^r}{\partial y} \right) - \frac{4(z - c^r)^3}{3h^2} \psi_y^r \quad (4.1b)$$

$$\mathbf{u}_3^r = w^r \quad (4.1c)$$

where c^r is the coordinate of the local midplane of each region. This introduces a change of coordinates that permits the description of the displacement that satisfies the conditions of zero transverse shear strains on the upper and lower surfaces of the sublaminate.

4.1.2. Continuity Conditions

Next, continuity conditions are imposed on the interfaces between the undelaminated region and the sublaminates. Ideally it is desired to match the displacement fields at the interface between the delaminated and undelaminated regions. Since the displacement distributions in Eqs. (4.1) are nonlinear, this equality condition cannot be satisfied exactly. There are a number of

different approaches to enforce continuity between the regions. A commonly used approach is to satisfy the equality in an average sense. This technique has the disadvantage that the slopes of the out-of-plane displacement, $\frac{\partial w}{\partial x}$ and $\frac{\partial w}{\partial y}$, are generally not equal on either side of the interface.

In this research, a more direct approach is developed in which continuity conditions are imposed at the interfaces between the undelaminated region and the sublaminates based on the offset between the finite element nodes at the midplane of each sublaminate. A transformation matrix method¹⁸ is used in which the out-of-plane displacements and slopes and the in-plane displacements are forced to be equal for the laminate and sublaminate on each side of the interface resulting in the following set of constraint equations

$$w_u - w_i = 0 \quad (4.2a)$$

$$\frac{\partial w_u}{\partial x} - \frac{\partial w_i}{\partial x} = 0 \quad (4.2b)$$

$$\frac{\partial w_u}{\partial y} - \frac{\partial w_i}{\partial y} = 0 \quad (4.2c)$$

$$u_u + \left(zc_i - \frac{4zc_i^3}{3h_u^2} \right) \psi_{xu} - zc_i \frac{\partial w_u}{\partial x} - u_i = 0 \quad (4.2d)$$

$$\left(1 - \frac{4zc_i^2}{h_u^2} \right) \psi_{xu} - \psi_{xi} = 0 \quad (4.2e)$$

$$v_u + \left(zc_i - \frac{4zc_i^3}{3h_u^2} \right) \psi_{yu} - zc_i \frac{\partial w_u}{\partial y} - v_i = 0 \quad (4.2f)$$

$$\left(1 - \frac{4zc_i^2}{h_u^2} \right) \psi_{yu} - \psi_{yi} = 0 \quad (4.2g)$$

where i represents each sublaminate in the delaminated region. A transformation matrix is constructed in order to eliminate the degrees of freedom at the boundary of the sublaminates from the system matrices. This transformation condenses the system along the boundary of the

delamination to effectively remove the sublaminates nodes and reform the system equations in terms of the nodal degrees of freedom belonging to the undelaminated region.

4.1.3. *Delamination Crack Tip Singularity*

The formulation presented in the previous sections neglects the singularity created by the delamination crack tip. As a result, the strains and stresses in the vicinity of where the sublaminates join the undelaminated structure are not accurately modeled. Since the objective of this work is to capture the effect of delamination on the global response of the structure this is not necessarily of concern, provided that this singularity does not create any large changes in the global deformation of the structure.

To verify that the crack tip singularity has minimal effect on the structural deformation, an idealized two-dimensional delaminated beam is modeled. The beam, as shown in Fig. 4.2, is cantilevered and has a delamination starting at the free end. The beam is assumed to be made of an isotropic material to allow convenient finite element modeling. The beam is modeled using a traditional mesh of 2-D plane strain elements and, also, with a 2-D mesh that includes a finer mesh size and quarter-point crack tip elements in the vicinity of the delamination tip. The quarter-point crack tip elements are further described in the next chapter. The sublaminates are subjected to an opening force at the free end, and the resulting displacement (end opening) is computed for both finite element meshes. In the following results, the material is assumed to

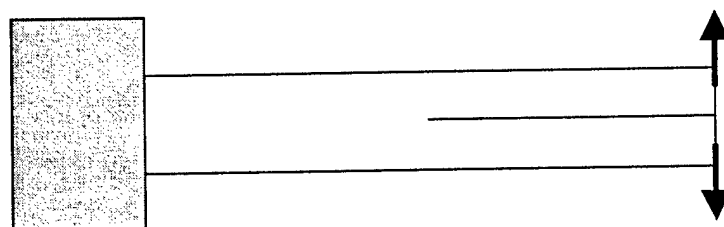


Fig. 4.2. Cantilevered beam for crack tip analysis.

have an elastic modulus of 91GPa, a Poisson's ratio of 0.3, and a density of 2000kg/m³. Figure 4.3 shows the two finite element meshes in the deformed state.

Figure 4.4 presents the difference in results, between the two models, for varying delamination length. In this case, the sublaminates are each 1mm thick, and the length of the undelaminated section is 1cm. In Fig. 4.4, the abscissa is the ratio of the length of the delamination to the total beam thickness. It can be seen that as the delamination becomes larger, the crack tip singularity has less influence on the deformed shape of the beam.

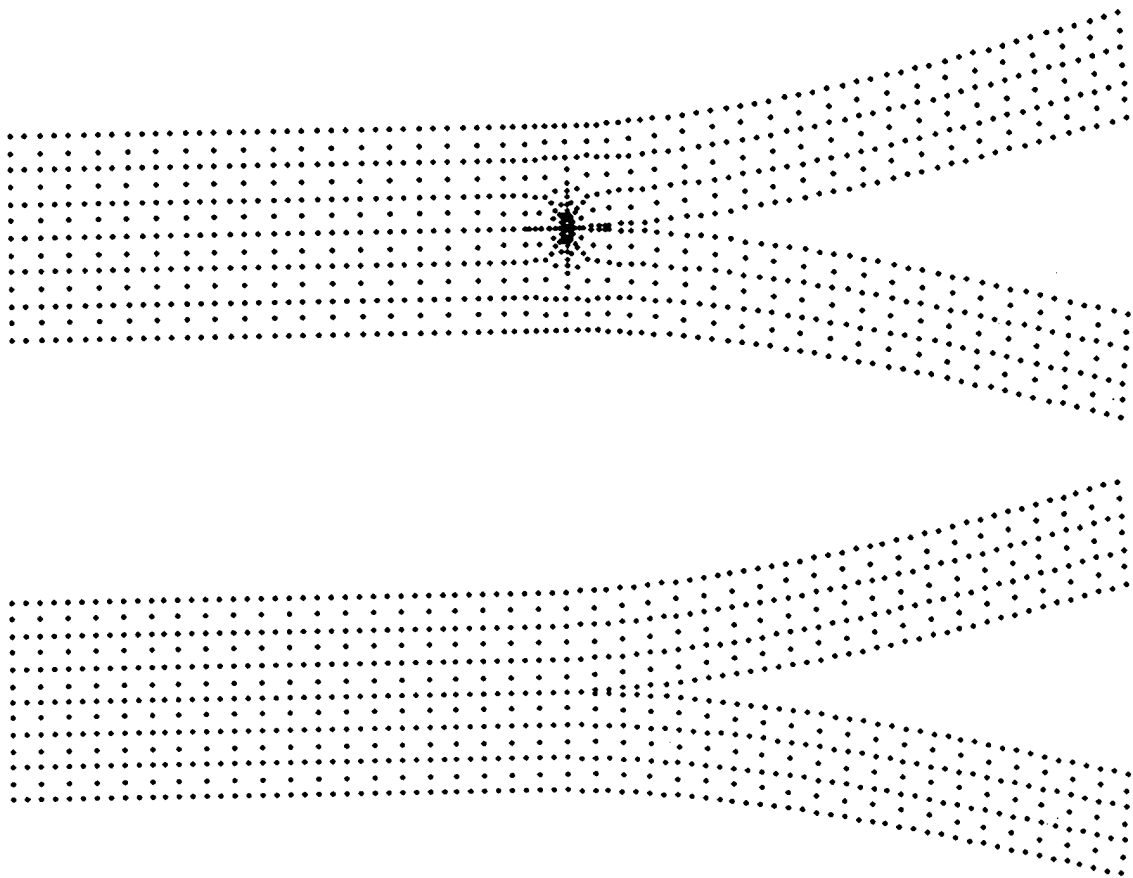


Fig. 4.3. Deformed shape of the finite element meshes with and without the crack tip singularity.

If the location of the delamination within the beam is changed to be closer to the surface, similar results are obtained. Figure 4.5 shows the difference in delamination opening for three different delamination locations. In the figure, t_1/t_2 , refers to the ratio of thickness of the upper sublamine to the thickness of the lower sublamine. It is important to note that the delamination location has virtually no effect on the calculated error. Since plate structures are generally thinner than beams, neglecting the crack tip singularity is not expected to create errors greater than one percent for all but the smallest of delaminations. Small delaminations would require a finer mesh of plate elements to model the small sublaminates, and a more accurate field description, through the thickness, may be necessary.

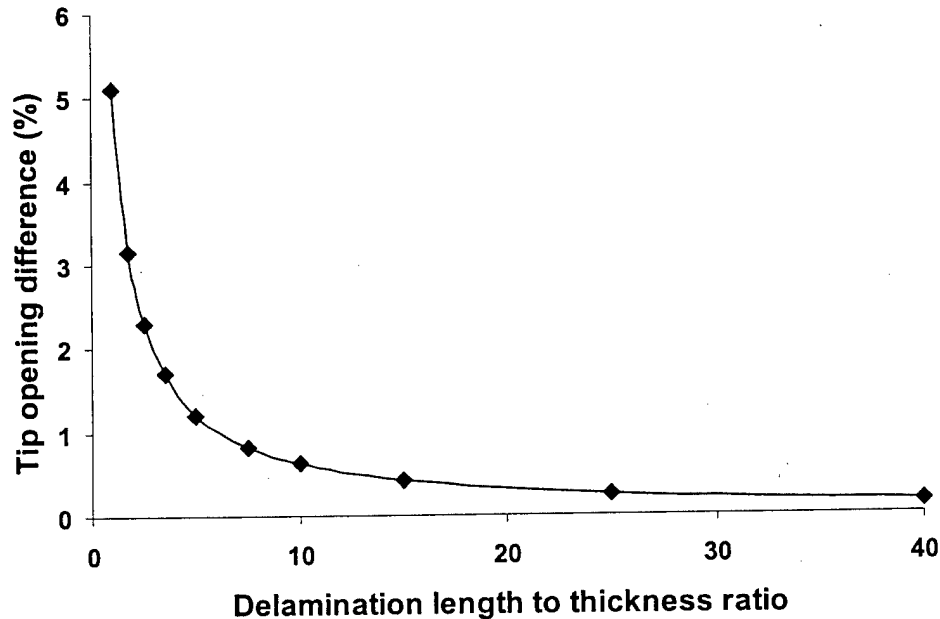


Fig. 4.4. Error from neglect of crack tip singularity.

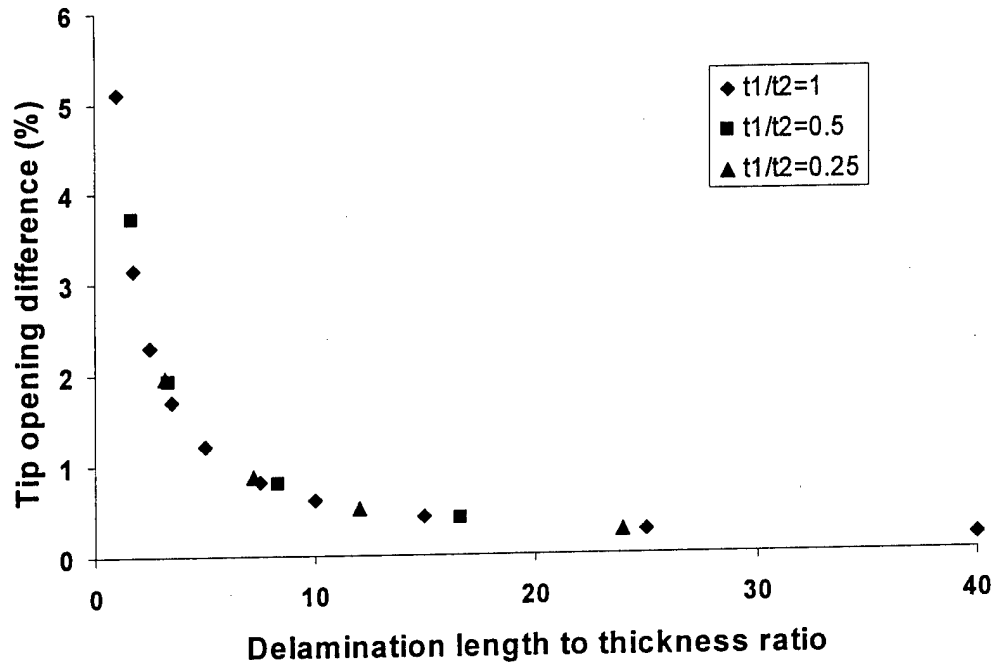


Fig. 4.5. Error from neglect of crack tip singularity for varying delamination locations.

4.2. Dynamic Contact

The formulation for the modeling of delamination developed in the previous section does not take into account any possible contact between the sublaminates. During vibration the delaminated region opens up a little, forming a gap between the sublaminates and then the sublaminates come back together, impacting each other. Traditional mode shapes, derived from the eigen vectors of the plate, are not valid representations of such behavior of a delaminated plate since any opening between the sublaminates would correspond to a condition where the sublaminates penetrate each other during the opposite half-cycle. In order to capture the true response of a plate during vibration, it is important to model the possibility of contact between the sublaminates in the delaminated region. Since little work has been done to assess the importance of sublaminate contact on the accuracy of delamination results, it is included in this model.

The contact between the sublaminates makes the response a nonlinear problem and time-integration methods are generally used to study the dynamic response. However, the sudden

impact of the sublaminate creates oscillations in analytical response that will destabilize most numerical methods. A discontinuous time-integration method proposed by Cho and Kim (1999a,b) is used in this work to treat the contact between the sublaminate. This method allows discontinuity to be incorporated into time-integration without having any other constraints enforced on the nodes during contact and release, and it also has been shown to be more stable than other methods.

4.2.1. *Contact Stiffness*

To represent contact between the sublaminate, each node of the upper sublaminate is assumed to be connected to the corresponding node of the lower sublaminate by a fictitious spring. This spring is assumed to have zero stiffness under tension and stiffness proportional to the transverse Young's modulus of the plate when subjected to compression. This is a typical method often used by other researchers modeling the buckling of composite laminates with delamination (Kardomateas and Schmueser, 1988; Pavier and Clarke, 1996). The difference during dynamic analysis is that the sudden change in stiffness of the springs acts like an impact, requiring careful modeling to correctly capture. Since this stiffness matrix is not constant, the dynamic response now becomes a nonlinear problem. During the time integration solution this matrix must be recomputed as the contact surface between the sublaminate changes over time.

The contact stiffness values must then be added to the existing system equations. For analytical purposes the stiffness matrix for the contact springs is formed as an independent matrix, \mathbf{k}_{ctc} , based on the current nodal displacements. This stiffness matrix is then added to the linear stiffness matrix in Eq. (3.76) before solving for the nodal displacements.

$$\mathbf{m}\mathbf{a} + \mathbf{c}\mathbf{v} + \mathbf{k}\mathbf{u} + \mathbf{k}_{ctc}\mathbf{u} = \mathbf{f} \quad (4.3)$$

As noted before, the matrix, \mathbf{k}_{ctc} , will change over time as the sublaminate come in contact with each other and then open up. The bimodularity of the contact springs makes the contact problem

nonlinear and a time-integration technique is used to study the response of the laminate when contact between the sublaminates is allowed.

4.2.2. Discontinuous Time-Integration Technique

The time-integration technique used in this paper is based on the discontinuous time-integration method of Cho and Kim (1999a). The reason for using a method such as this, as opposed to a traditional Newmark method, is that the sudden change in stiffness that occurs during impact and release of the sublaminates creates jumps in the field variables resulting in numerical oscillations in the analytical solution. The discontinuous time-integration method uses a generalized derivative concept to model the effect of sudden constraints that occur during contact/impact problems. The generalized derivative allows discontinuity to be incorporated into time-integration without having any other constraints enforced on the nodes during contact and release.

The definition of the generalized derivative of distribution (Cho and Kim, 1999a) is constructed through an integration by parts formula. With this procedure, the difficulty of differentiating a distribution is transferred to the differentiation of a test function. Integration by parts gives the generalized relation between the displacement vector, \mathbf{u} , and the velocity vector, \mathbf{v} .

$$\int_n^{n+1} \gamma^T \mathbf{v} dt = - \int_n^{n+1} \dot{\gamma}^T \mathbf{u} dt + \gamma^T \mathbf{u} \Big|_{t_n}^{t_{n+1}} \quad \text{for all } \gamma(t) \quad (4.4)$$

where γ is the test function. In weighted residual form this equation is written as

$$0 = \int_n^{n+1} \gamma^T (\mathbf{v} - \dot{\mathbf{u}}) dt = \int_n^{n+1} \gamma^T \mathbf{v} + \dot{\gamma}^T \mathbf{u} dt - \gamma^T \mathbf{u} \Big|_{t_n}^{t_{n+1}} \quad \text{for all } \gamma(t) \quad (4.5)$$

A similar equation can be written for the relation between the velocity and the acceleration.

$$\int_n^{n+1} \gamma^T \mathbf{a} dt = - \int_n^{n+1} \dot{\gamma}^T \mathbf{v} dt + \gamma^T \mathbf{v} \Big|_{t_n}^{t_{n+1}} \quad \text{for all } \gamma(t) \quad (4.6)$$

The time step shown in Figure 4.6 includes jump conditions for both displacements, velocities and accelerations at time t_n , but the test function is assumed to be continuous to enforce the effect of the initial condition.

Linear Lagrange interpolation functions are used in the time domain for approximating the displacement, \mathbf{u} , velocity, \mathbf{v} , acceleration, \mathbf{a} , and the test function, γ . The approximation vectors are written for the interval $t_n < t \leq t_{n+1}$ as follows

$$\mathbf{u}(t) = \psi_0(t)\mathbf{u}_n^0 + \psi_1(t)\mathbf{u}_n^1 \quad (4.7a)$$

$$\mathbf{v}(t) = \psi_0(t)\mathbf{v}_n^0 + \psi_1(t)\mathbf{v}_n^1 \quad (4.7b)$$

$$\mathbf{a}(t) = \psi_0(t)\mathbf{a}_n^0 + \psi_1(t)\mathbf{a}_n^1 \quad (4.7c)$$

$$\gamma(t) = \psi_0(t)\gamma_n^0 + \psi_1(t)\gamma_n^1 \quad (4.7d)$$

where

$$\psi_0(t) = \frac{t_{n+1} - t}{t_{n+1} - t_n} \quad (4.8a)$$

$$\psi_1(t) = \frac{t - t_n}{t_{n+1} - t_n} \quad (4.8b)$$

Substituting Eqs. (4.7a-d) into Eqs. (4.5) and (4.6) yields the approximated relations for the time derivative.

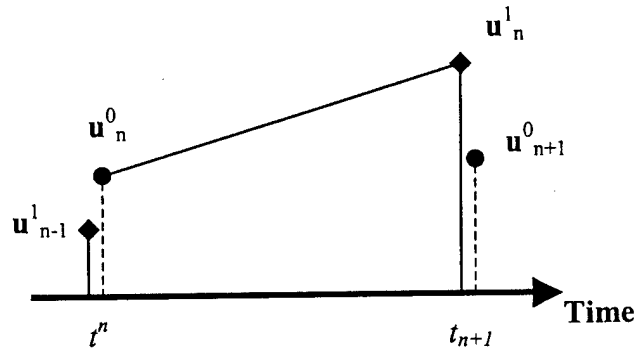


Fig. 4.6. Description of the time domain with jumps in the displacement variable.

$$0 = \sum_{i=0}^i \left\{ \int_{t_n}^{t_{n+1}} \left(\psi_i \psi_0 \gamma_n^{iT} \mathbf{v}_n^0 + \psi_i \psi_1 \gamma_n^{iT} \mathbf{v}_n^1 + \dot{\psi}_i \psi_0 \gamma_n^{iT} \mathbf{u}_n^0 + \dot{\psi}_i \psi_1 \gamma_n^{iT} \mathbf{u}_n^1 \right) dt \right\} - \gamma^T \mathbf{u} \Big|_{t_n}^{t_{n+1}} \quad (4.9a)$$

$$0 = \sum_{i=0}^i \left\{ \int_{t_n}^{t_{n+1}} \left(\psi_i \psi_0 \gamma_n^{iT} \mathbf{a}_n^0 + \psi_i \psi_1 \gamma_n^{iT} \mathbf{a}_n^1 + \dot{\psi}_i \psi_0 \gamma_n^{iT} \mathbf{v}_n^0 + \dot{\psi}_i \psi_1 \gamma_n^{iT} \mathbf{v}_n^1 \right) dt \right\} - \gamma^T \mathbf{v} \Big|_{t_n}^{t_{n+1}} \quad (4.9b)$$

The variables \mathbf{u} , \mathbf{v} , and \mathbf{a} contain discontinuities at the initial time, t_n , so the vectors from the previous time step are included.

$$\begin{aligned} \mathbf{u}(t_n) &= \mathbf{u}_{n-1}^1 & \mathbf{v}(t_n) &= \mathbf{v}_{n-1}^1 & \mathbf{a}(t_n) &= \mathbf{a}_{n-1}^1 & \gamma(t_n) &= \gamma_n^0 \\ \mathbf{u}(t_{n+1}) &= \mathbf{u}_n^1 & \mathbf{v}(t_{n+1}) &= \mathbf{v}_n^1 & \mathbf{a}(t_{n+1}) &= \mathbf{a}_n^1 & \gamma(t_{n+1}) &= \gamma_n^1 \end{aligned} \quad (4.10)$$

The effect of the initial condition is weakly imposed via \mathbf{u}_{n-1}^1 , \mathbf{v}_{n-1}^1 and \mathbf{a}_{n-1}^1 . Because Eqs. (4.9a,b) must hold for all γ_n^i , it can be written in matrix form as

$$\hat{\Phi} \mathbf{U}_{n+1} = \Phi \mathbf{V}_{n+1} + \Theta \mathbf{U}_n \quad (4.11a)$$

$$\hat{\Phi} \mathbf{V}_{n+1} = \Phi \mathbf{A}_{n+1} + \Theta \mathbf{V}_n \quad (4.11b)$$

where

$$\mathbf{U}_{n+1} = \begin{Bmatrix} \mathbf{u}_n^0 \\ \mathbf{u}_n^1 \end{Bmatrix} \quad \mathbf{V}_{n+1} = \begin{Bmatrix} \mathbf{v}_n^0 \\ \mathbf{v}_n^1 \end{Bmatrix} \quad \mathbf{A}_{n+1} = \begin{Bmatrix} \mathbf{a}_n^0 \\ \mathbf{a}_n^1 \end{Bmatrix} \quad (4.12)$$

$$\hat{\Phi} = \begin{bmatrix} \left(- \int_n^{n+1} \dot{\psi}_0 \psi_0 dt \right) \mathbf{I} & \left(- \int_n^{n+1} \dot{\psi}_0 \psi_1 dt \right) \mathbf{I} \\ \left(- \int_n^{n+1} \dot{\psi}_1 \psi_0 dt \right) \mathbf{I} & \left(1 - \int_n^{n+1} \dot{\psi}_1 \psi_1 dt \right) \mathbf{I} \end{bmatrix} = \begin{bmatrix} \frac{1}{2} \mathbf{I} & \frac{1}{2} \mathbf{I} \\ -\frac{1}{2} \mathbf{I} & \frac{1}{2} \mathbf{I} \end{bmatrix} \quad (4.13)$$

$$\Phi = \begin{bmatrix} \left(\int_n^{n+1} \psi_0 \psi_0 dt \right) \mathbf{I} & \left(\int_n^{n+1} \psi_0 \psi_1 dt \right) \mathbf{I} \\ \left(\int_n^{n+1} \psi_1 \psi_0 dt \right) \mathbf{I} & \left(\int_n^{n+1} \psi_1 \psi_1 dt \right) \mathbf{I} \end{bmatrix} = \begin{bmatrix} \frac{\Delta t}{3} \mathbf{I} & \frac{\Delta t}{6} \mathbf{I} \\ \frac{\Delta t}{6} \mathbf{I} & \frac{\Delta t}{3} \mathbf{I} \end{bmatrix} \quad (4.14)$$

$$\Theta = \begin{bmatrix} \mathbf{0} & \mathbf{I} \\ \mathbf{0} & \mathbf{0} \end{bmatrix} \quad (4.15)$$

Inverting the relation yields the solution for the time step

$$\mathbf{U}_{n+1} = \Psi \mathbf{V}_{n+1} + \Psi_0 \mathbf{U}_n \quad (4.16a)$$

$$\mathbf{V}_{n+1} = \Psi \mathbf{A}_{n+1} + \Psi_0 \mathbf{V}_n \quad (4.16b)$$

where

$$\Psi = \begin{bmatrix} \frac{\Delta t}{6} \mathbf{I} & -\frac{\Delta t}{6} \mathbf{I} \\ \frac{\Delta t}{2} \mathbf{I} & \frac{\Delta t}{2} \mathbf{I} \end{bmatrix} \quad (4.17)$$

$$\mathbf{J} = \begin{bmatrix} 0 & \mathbf{I} \\ 0 & \mathbf{I} \end{bmatrix} \quad (4.18)$$

The next step is to incorporate the time steps into the system matrices in Eq. (4.3). It is important to note that the system vectors \mathbf{u} , \mathbf{v} , and \mathbf{a} include not only mechanical displacements, but also the electrical displacements. The governing equations must apply at both the beginning and end of each time step. This yields following form

$$\begin{bmatrix} \mathbf{m}^0 & 0 \\ 0 & \mathbf{m}^1 \end{bmatrix} \begin{Bmatrix} \mathbf{a}_n^0 \\ \mathbf{a}_n^1 \end{Bmatrix} + \begin{bmatrix} \mathbf{c}^0 & 0 \\ 0 & \mathbf{c}^1 \end{bmatrix} \begin{Bmatrix} \mathbf{v}_n^0 \\ \mathbf{v}_n^1 \end{Bmatrix} + \begin{bmatrix} \mathbf{k}^0 + \mathbf{k}_{ctc}^0 & 0 \\ 0 & \mathbf{k}^1 + \mathbf{k}_{ctc}^1 \end{bmatrix} \begin{Bmatrix} \mathbf{u}_n^0 \\ \mathbf{u}_n^1 \end{Bmatrix} = \begin{Bmatrix} \mathbf{f}^0 \\ \mathbf{f}^1 \end{Bmatrix} \quad (4.19)$$

or

$$\mathbf{M} \mathbf{A}_{n+1} + \mathbf{C} \mathbf{V}_{n+1} + (\mathbf{K} + \mathbf{K}_{ctc}) \mathbf{U}_{n+1} = \mathbf{F}_{n+1} \quad (4.20)$$

Combining the Eqs. (4.16a,b) and Eq.(4.20) gives the governing equation for the discontinuous time step.

$$(\mathbf{M} \Psi^{-1} \Psi^{-1} + \mathbf{C} \Psi^{-1} + \mathbf{K} + \mathbf{K}_{ctc}) \mathbf{U}_{n+1} = \mathbf{F}_{n+1} - \mathbf{M} \bar{\mathbf{A}}_{n+1} - \mathbf{C} \bar{\mathbf{V}}_{n+1} \quad (4.21)$$

where $\bar{\mathbf{V}}_{n+1}$ and $\bar{\mathbf{A}}_{n+1}$ are the predictors for velocity and acceleration.

$$\bar{\mathbf{V}}_{n+1} = -\Psi^{-1} \mathbf{J} \mathbf{U}_n \quad (4.22a)$$

$$\bar{\mathbf{A}}_{n+1} = -\Psi^{-1} \Psi^{-1} \mathbf{J} \mathbf{U}_n - \Psi^{-1} \mathbf{J} \mathbf{V}_n \quad (4.23b)$$

These equations can be solved using a predictor-corrector solution algorithm. Thus, for each time step, the following procedure is performed

(i) Calculate the predictors in Eqs. (4.22a,b)

(ii) Calculate the effective stiffness matrix

$$\mathbf{K}_{eff} = \mathbf{M}\Psi^{-1}\Psi^{-1} + \mathbf{C}\Psi^{-1} + \mathbf{K} + \mathbf{K}_{cfc} \quad (4.24)$$

(iii) Solve for current displacements

$$\mathbf{K}_{eff}\mathbf{U}_{n+1} = \mathbf{F}_{n+1} - \mathbf{M}\bar{\mathbf{A}}_{n+1} - \mathbf{C}\bar{\mathbf{V}}_{n+1} \quad (4.25)$$

(iv) Correct the velocities and accelerations

$$\mathbf{V}_{n+1} = \Psi^{-1}\mathbf{U}_{n+1} + \bar{\mathbf{V}}_{n+1} \quad (4.26a)$$

$$\mathbf{A}_{n+1} = \Psi^{-1}\Psi^{-1}\mathbf{U}_{n+1} + \bar{\mathbf{A}}_{n+1} \quad (4.26b)$$

This solution method can be computationally expensive, especially for large system matrices, but it effectively deals with the discontinuity created by contact between the sublaminates and prevents oscillations in the numeric results. The results shown by Cho and Kim (1999a) illustrate how much more effective this method is than traditional Newmark methods.

Table 4.1.

Properties of carbon-epoxy laminae.

Property	Carbon-epoxy
E11	134.4 GPa
E22	10.34 GPa
G12	5.00 GPa
ν	0.33
ρ	1.477 g/cm ³

4.3. Results

Verification of the proposed model is performed using the experimental results obtained by Shen and Grady (1992). The test specimen examined is a carbon-epoxy composite cantilevered plate with dimensions, 5 in. length and 0.5 in. width. The ply stacking sequence is

$[0^\circ, 90^\circ]_{2s}$ and the ply thickness is 0.005 in., resulting in a length to thickness ratio (L/h) of 125.

The material properties for the carbon-epoxy composite are listed in Table 4.1.

First the natural frequencies of the plate are determined using the eigen values of the system and compared with the experimentally determined natural frequencies for the first vibration mode. Both delaminated and undelaminated plates are used in this comparison. For the delaminated case, a centrally located (along the longitudinal axis) through-the-width delamination with four different ply locations is considered. Delamination lengths of 1 in., 2 in., 3 in. and 4 in. are examined and compared with the undelaminated values. Thus, in Table 4.2, interface 1 corresponds to a delamination located at the midplane and interface 4 refers to the case of surface delamination with the uppermost ply being delaminated.

The plate is modeled using a finite element mesh of 20×4 elements. The refined higher order theory results in seven degrees-of-freedom per node, or 735 degrees-of-freedom for the undelaminated plate. The introduction of delamination adds additional degrees for freedom associated with the new sublaminates. For a 2 in. delamination the total number of degrees-of-freedom for the system is 1050.

Table 4.2.

Comparison of the natural frequencies (Hz) for a delaminated composite plate predicted by the present model with experimental data.

Undelaminated	Experimental		Present Model	
	79.83		82.11	
Interface	1 in.	2 in.	3 in.	4 in.
1 - Exp.	78.17	75.38	66.96	57.54
Model	81.37	76.73	67.57	56.89
2- Exp.	77.79	75.13	67.96	48.37
Model	81.42	77.11	68.42	58.04
3- Exp.	80.12	79.75	76.96	72.46
Model	81.92	80.65	77.44	71.66
4- Exp.	75.96	68.92	62.50	55.63
Model	81.94	80.83	78.04	73.21

The results from the present model and the experimentally determined average values are listed in Table 4.2. It is important to note that in the eigen analysis, contact between the sublaminates during vibration is not modeled. Thus the analytically computed natural frequencies are expected to over-predict the reduction in natural frequency caused by delamination. However, good overall correlation is observed between the results from the present model and experiments, as shown in Table 4.2. The only exception is the case with delamination located at interface 4 (uppermost lamina). The large drop in natural frequency that was observed experimentally is most likely due to buckling of the upper sublaminate. To capture this phenomenon analytically, nonlinear modeling with Von Karman nonlinear strains is required.

Next the effect of contact between the laminates is examined. The plate is subjected to a one Newton tip load and released from this static position. The discontinuous time integration method is used to examine the effect of delamination on the response. Figure 4.7 shows the analytically computed time histories of the undelaminated plate and the plate with a 2 in. delamination at interface 2. The deflection plotted in Fig. 4.7 is the vertical displacement at the midpoint of the delaminated area on the upper sublaminate. As seen in Fig. 4.7, the response curves for the delaminated plate with and without contact are virtually superimposed showing that the contact has little effect on this low frequency vibration mode. Figure 4.8 shows the response of the two sublaminates for a plate with a 2 in. delamination at interface 3. The opening and closing of the delamination can be clearly seen, however, this has little effect on the frequency of vibration. These results seem to indicate that the contact phenomenon has little effect on the natural frequencies of low vibration modes, at least in cases when the size of the delamination is not disproportionately large. As a result of this, the natural frequencies estimated using the eigen values of the delaminated plate are reasonably accurate, as seen in Table 4.2. The first bending and twisting mode shapes for the undelaminated plate are shown in Fig. 4.9, and those for the upper surface of the plate with a 2 in. delamination at interface 2 are shown in Fig.

4.10. The bending mode shows little distortion, but the twisting mode shows a large amount of twist concentrated in the location of the delamination.

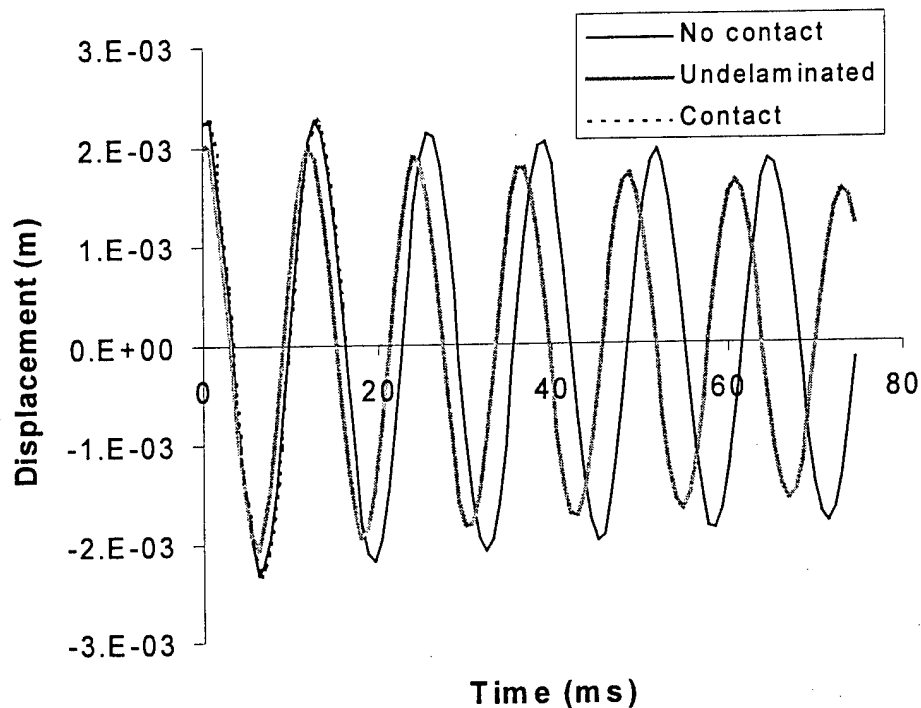


Fig. 4.7. Time history for a delaminated plate under free response from a static load.

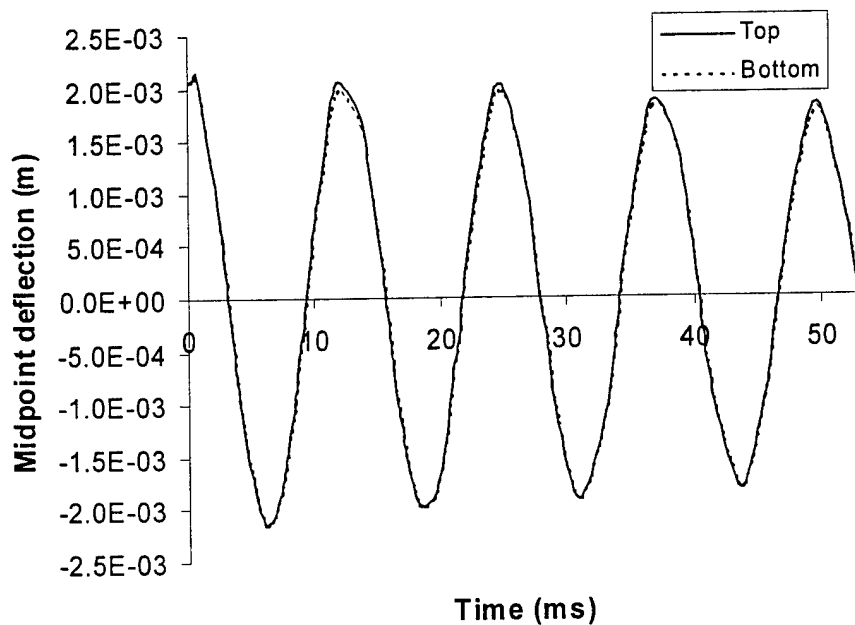


Fig. 4.8. Displacement of upper and lower sublaminae for a delaminated $[0^\circ, 90^\circ]_{2s}$ plate under free response.

It is also useful to examine the effects of varying ply stacking sequence on the natural frequencies of the delaminated plate. Figure 4.11 shows the natural frequencies for the first two bending modes and the first twisting mode for the plate with a $[0^\circ, 90^\circ]_{2s}$ stacking sequence and a 2 in. delamination located at different interfaces. It is clear that delamination located towards the midplane of the plate have the largest effect on the natural frequency of the first vibration mode while delamination closer to the surface more significantly affects the second and higher

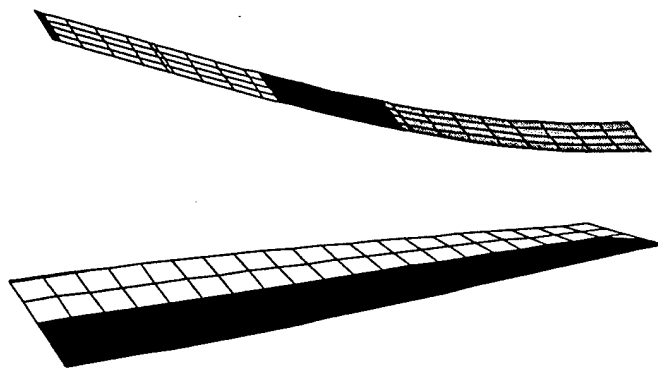


Fig. 4.9. First bending and twisting modes for the undelaminated $[0^\circ, 90^\circ]_{2s}$ cantilevered plate.

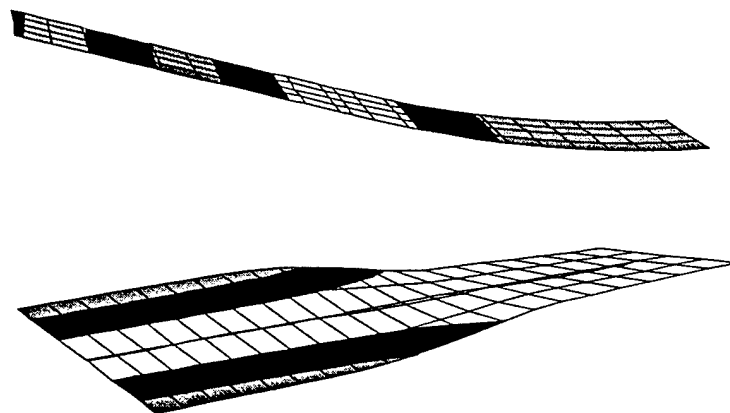
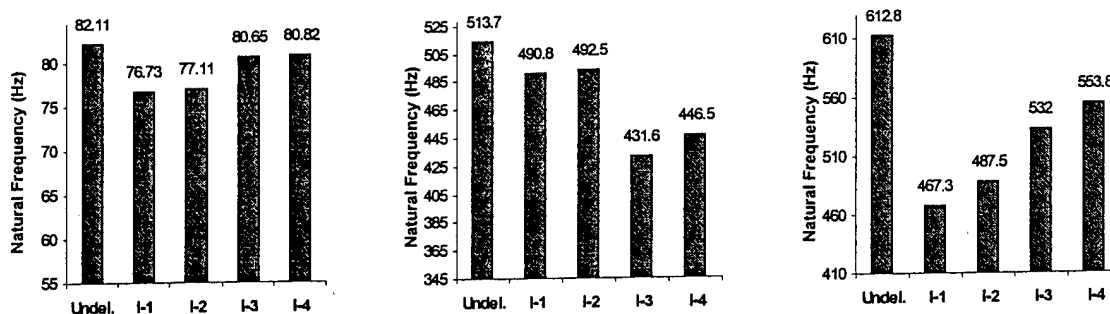


Fig. 4.10. First bending and twisting modes for the $[0^\circ, 90^\circ]_{2s}$ cantilevered plate with 2 in. delamination.

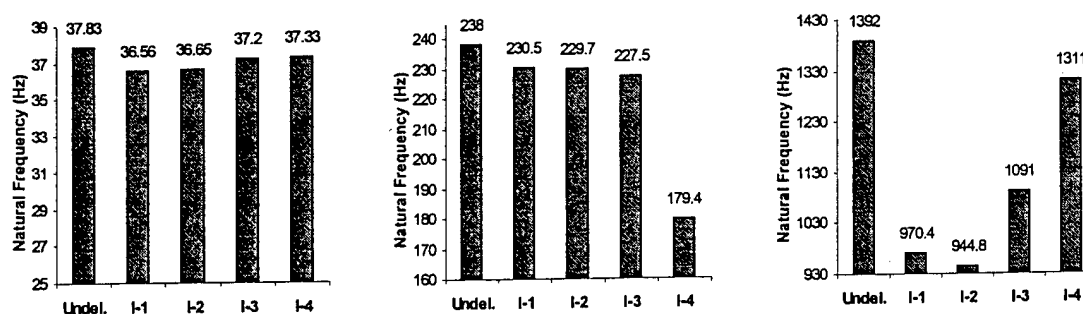
frequency bending modes. Also, larger impact of delamination is observed in the twisting modes. Figure 4.12 presents the results for a $[45^\circ, -45^\circ]_{2s}$ configuration. It can be seen that the bending modes of this angle ply layup are less affected by delamination compared with the crossply layup. This is the result of the increased anisotropy of the angle ply layup and the increased coupled between the shear and tensile strains. However, the twisting frequency is reduced by over thirty percent. This is an even greater reduction than the twenty-three percent drop observed in the $[0^\circ, 90^\circ]_{2s}$ laminate.

So far only balanced laminates were considered. To study the effect of an unbalance ply layup, a laminate of $[0^\circ, 45^\circ]_{2s}$ stacking sequence is considered, and results are shown in Fig. 5.13. Note that although this ply arrangement causes significant coupling between the bending and twisting modes, the reductions in natural frequency due to delamination are very similar to those observed in the crossply layup. Thus, it appears that the 0° plies dominate the response of the cantilevered composite plate.

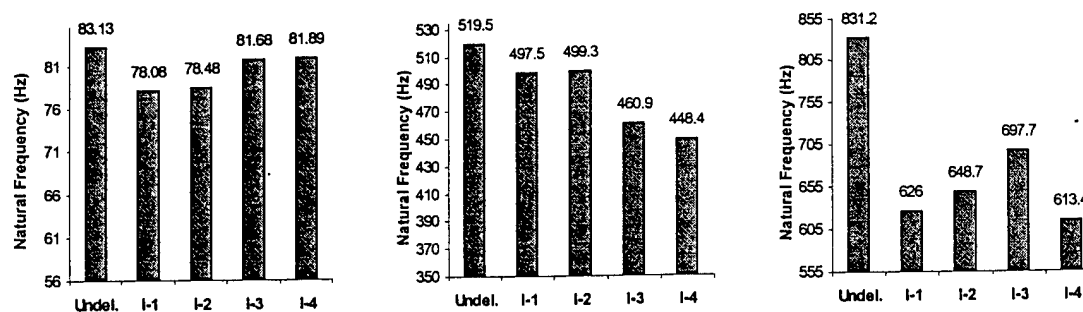
Next the effect of laminate thickness is investigated. The $[0^\circ, 90^\circ]_{2s}$ laminate is considered, but with an assumed ply thickness of 0.025 in., making the laminate five times thicker and changing the length to thickness ratio, $L/h = 25$. In practice this could be achieved by stacking the plies in groups of five to create a $[0_5^\circ, 90_5^\circ]_{2s}$ laminate. The effects of delamination on natural frequencies for this laminate are shown in Fig. 4.14. The natural frequencies for this laminate are predictably greater than those of the original laminate due to the increase plate thickness, but the overall trend is very similar to that seen in Fig. 4.11. The change in thickness does create moderate changes in the natural frequencies of the delaminated plate, due to the significant transverse shear within the plate.



a) First bending mode b) Second bending mode c) First twisting mode
 Fig. 4.11. Natural frequencies for a cantilevered $[0,90]_{2s}$ laminate with delamination at varying ply interfaces, $L/h = 125$.



a) First bending mode b) Second bending mode c) First twisting mode
 Fig. 4.12. Natural frequencies for a cantilevered $[45,-45]_{2s}$ laminate with delamination at varying ply interfaces, $L/h = 125$.



a) First bending mode b) Second bending mode c) First twisting mode
 Fig. 4.13. Natural frequencies for a cantilevered $[0,45]_{2s}$ unbalanced laminate with varying delamination locations, $L/h = 125$.

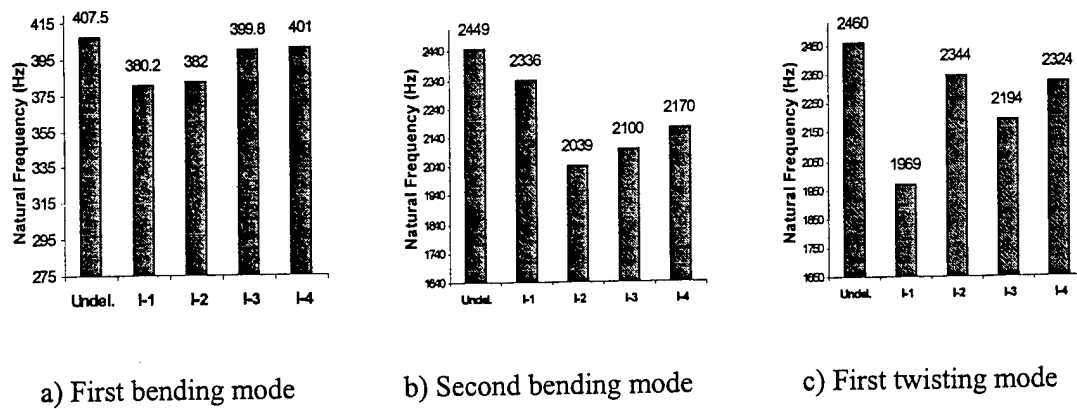


Fig. 4.14. Natural frequencies for a cantilevered $[0,90]_{2s}$ with $L/h = 25$.

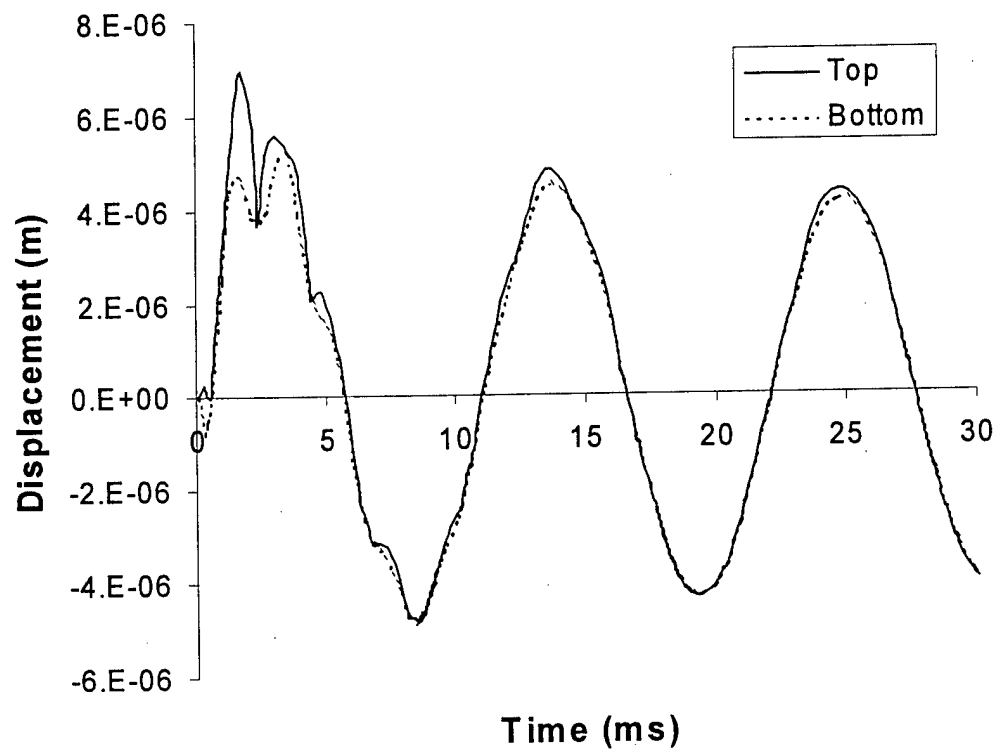


Fig. 4.15. Displacement of the sublaminates during impulse loading for a plate with a 2 in. delamination at interface 3.

Finally, the response of an adaptive laminate in the presence of delamination is examined. A 1 in. by 0.5 in. piezoelectric sensor is assumed to be bonded to the upper surface of the plate. The piezo is assumed to be made of PZT-5H with a thickness of 0.25 mm and is

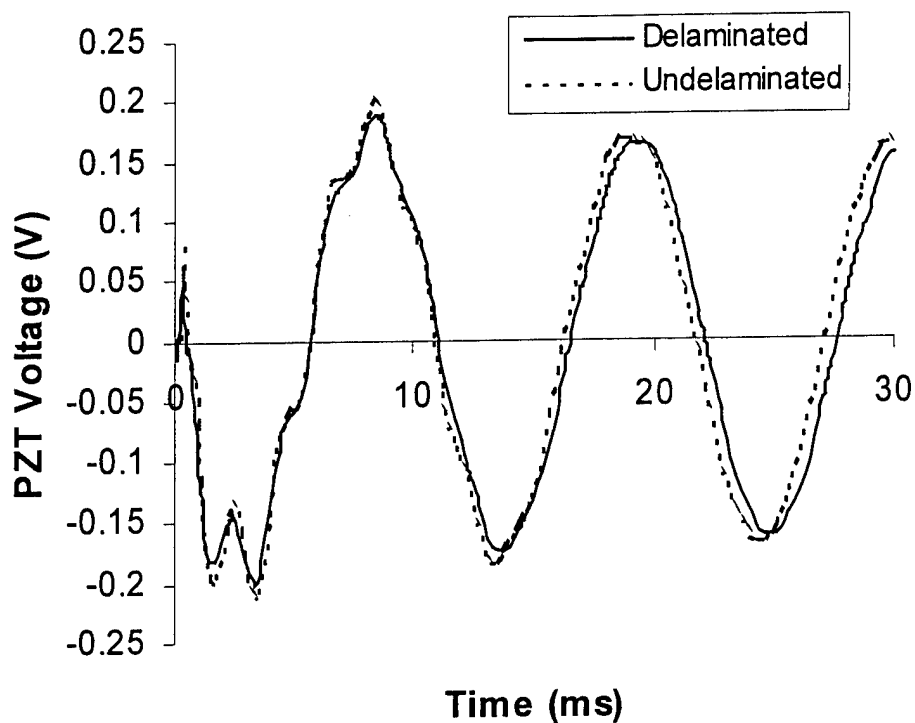


Fig. 4.16. Comparison of PZT output voltage during impulse loading for a plate with a 2 in. delamination at interface 3.

located at a distance of 0.25 in. from the root of the cantilevered plate. The response of the plate is computed for a 5 μ s, 1N impulse tip load.

The first case examined is a $[0^\circ, 90^\circ]_{2s}$ laminate with a 2 in. delamination at interface 3. Figure 4.15 shows the displacement of the upper and lower sublaminates at the center of the delaminated zone. Contact and impact between the sublaminates is very visible due to the high frequency aspects of the vibration. The PZT is assumed to be open circuited and the output voltage is measured. The voltage history is shown in Fig. 4.16. It can be seen that the piezoelectric voltage is definitely affected by the presence of delamination, but the overall shape of the output does not change significantly. This implies that if the PZT were used as sensor, the output signal would be similarly altered by the delamination.

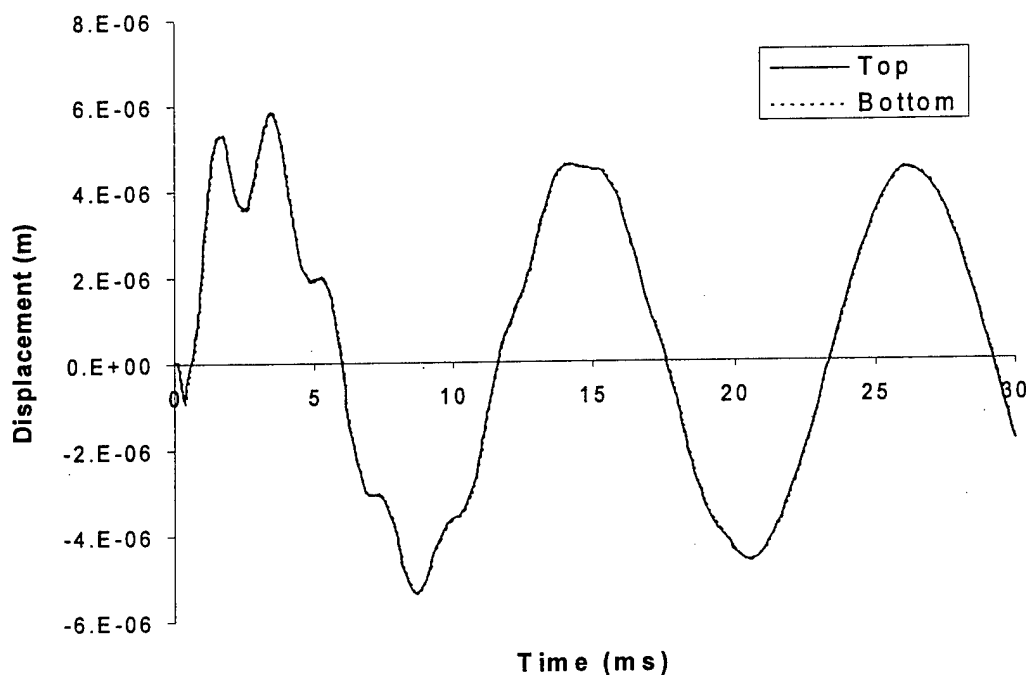


Fig. 4.17. Displacement of the sublaminates during impulse loading for a $[0^\circ, 90^\circ]_{2s}$ laminate with a 2 in. delamination at interface 2.

The next case analyzed is the same $[0^\circ, 90^\circ]_{2s}$ laminate, but with the 2 in. delamination at interface 2. Figure 4.17 shows the displacement of the upper and lower sublaminates at the center of the delaminated zone and Fig. 4.18 shows the voltage history. For this case, the gap opening between the sublaminates is almost imperceptible, but the delamination creates much more significant changes in the voltage output of the sensor. This is consistent with the changes in natural frequencies that were observed in Fig. 4.11. Little opening between the sublaminates is also expected since each sublaminates is thick enough to have appreciable bending stiffness.

The cases studied illustrate the difficulty of using low frequency response to detect damage in composite laminates. Delamination and sublaminates contact are more influential at higher frequencies, which can be modeled using the present approach with a more refined finite element mesh. The developed model can prove to be a useful tool in damage detection studies.

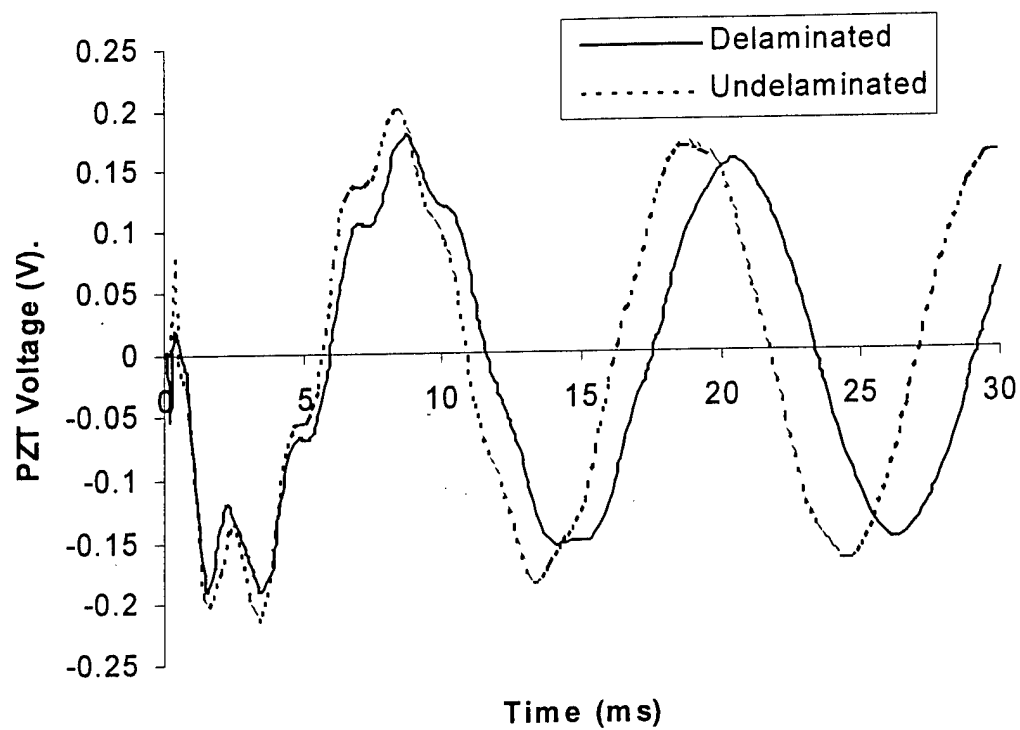


Fig. 4.18. Comparison of PZT output voltage during impulse loading for a $[0^\circ, 90^\circ]_{2s}$ laminate with a 2 in. delamination at interface 2.

5. Effect of Matrix Cracking

Unlike other studies that attempt to predict the amount of damage based on loading history, in this study, it is assumed that the damage is known. The cracking can be in any combination of layers including the surface layers of the laminate. The effects of matrix cracking must be developed to reflect the structural model used. If only the effects of Mode I and Mode III crack opening are considered, then the results would then only be appropriate for classical plate models where transverse shear is not considered. For moderately thick plates modeled using a first order shear deformation theory, the transverse shear plays a role in plate deflection, and therefore Mode II crack behavior must be determined.

A number of assumptions must be made in order to model the effect of matrix cracking in a composite laminate. The first assumption is that the cracks can be modeled as a statistically uniform array spaced at some average distance. It is also assumed that all of the cracks extend vertically through the entire layer and run parallel to the fibers, as shown in Figure 5.1. The term "layer" is used in this section as opposed to "ply." The reason for this is that consecutive plies oriented in the same direction have no means of arresting crack growth, which is normally done when the crack tip intersects fibers running in a different direction. Thus, multiple plies with the same fiber orientation angle behave as a single, thick layer. As will be described later, it is also assumed that cracking in one layer is not influence by the presence of cracks in other layers. Crack growth is not considered in this work.

5.1. Matrix Crack Modeling

Since the equations of motion for the composite plate developed earlier in this work are based on the variation of the total energy, the effect of matrix cracking is determined using the

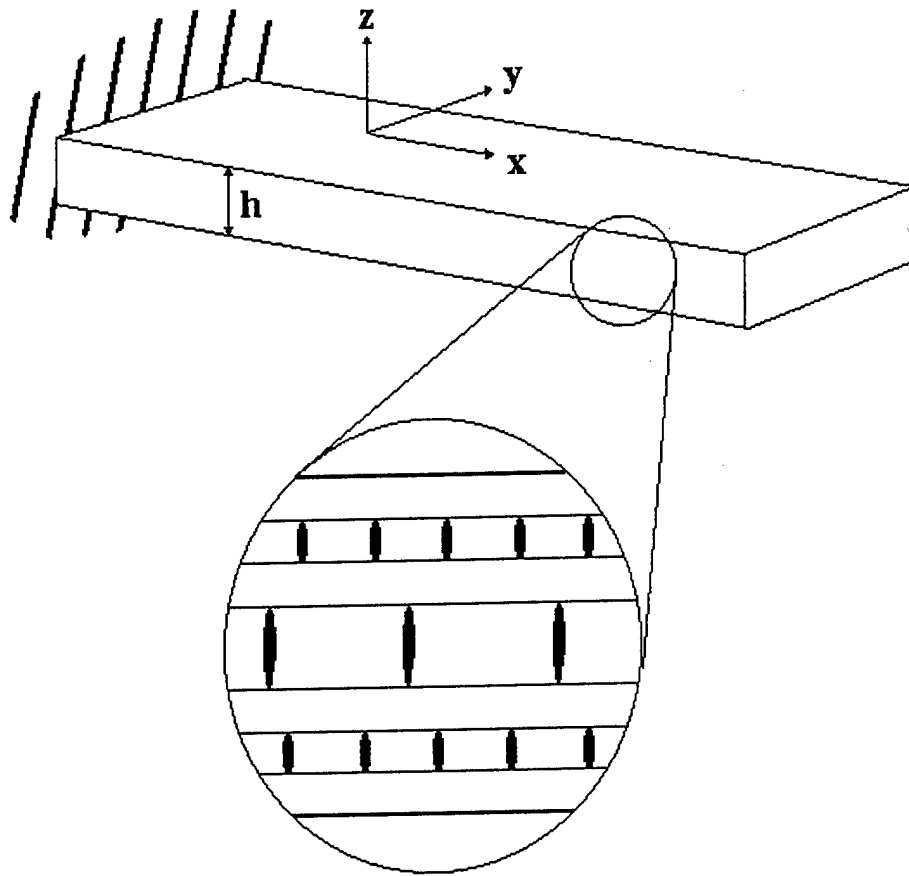


Fig. 5.1. Assumed geometry for cracked composite plate.

energy contained in crack opening. If a convenient method can be found for determining this energy then the effect of matrix cracking can be incorporated as a reduction in laminate stiffness.

5.1.1. *Effective Laminate Stiffness*

The strains for the higher order laminate theory, Eqs. (3.33a-f), can be expressed using the following form

$$\varepsilon_m = \varepsilon_m^o + z(\kappa_m^o + z^2 \kappa_m^2) \quad m = 1, 2, 6 \quad (5.1a)$$

$$\varepsilon_n = \varepsilon_n^o + z^2 \kappa_n^2 \quad n = 4, 5 \quad (5.1b)$$

where z is the location relative to the midplane of the laminate, and ϵ^0 , κ^0 and κ^2 are coefficients expressed as functions of u , v , w , ψ_x , and ψ_y . The total potential strain energy of an uncracked plate can be expressed as follows

$$U_{uncracked} = \int_A \left[\frac{1}{2} \mathbf{s}^T \mathbf{C}_I \mathbf{s} + \frac{1}{2} \mathbf{s}_o^T \mathbf{C}_o \mathbf{s}_o \right] dA \quad (5.2)$$

where, for convenience, the strains are separated into in-plane and out-of-plane components

$$\mathbf{s} = \{\epsilon_1^0 \quad \epsilon_2^0 \quad \epsilon_6^0 \quad \kappa_1^0 \quad \kappa_2^0 \quad \kappa_6^0 \quad \kappa_1^2 \quad \kappa_2^2 \quad \kappa_6^2\}^T \quad (5.3a)$$

$$\mathbf{s}_o = \{\epsilon_4^0 \quad \epsilon_5^0 \quad \kappa_4^2 \quad \kappa_5^2\}^T \quad (5.3b)$$

and the stiffness matrices, \mathbf{C}_I and \mathbf{C}_o , have been integrated through the thickness of the laminate, as defined in Eqs. (3.51 and 3.53). This notation allows convenient expression of the stress strain relations in matrix form and separation of the in-plane and out-of-plane effects.

For a laminate with matrix cracking the total potential energy is reduced since a portion of the energy is associated with the opening of the cracks during deformation. Thus, the total potential energy is expressed as follows

$$U_{cracked} = \int_A \left[\frac{1}{2} \mathbf{s}^T \mathbf{C}_I \mathbf{s} + \frac{1}{2} \mathbf{s}_o^T \mathbf{C}_o \mathbf{s}_o \right] dA - \Delta U_{crack} \quad (5.4)$$

where the energy associated with crack opening, assuming that the work done in one cracked layer is not affected by cracking in other layers is defined as

$$\Delta U_{crack} = \sum_{k=1}^N \left\{ \int_A \left[\frac{1}{2} t^k \rho^k \boldsymbol{\tau}^k \boldsymbol{\tau}^{kT} \boldsymbol{\beta}^{kk} \boldsymbol{\tau}^k + \frac{1}{2} t^k \rho^k \boldsymbol{\tau}_o^k \boldsymbol{\beta}_o^{kk} \boldsymbol{\tau}_o^k \right] dA \right\} \quad (5.5)$$

The summation in this expression provides the total energy for all cracked layers. The energy is seen to be proportional to the thickness of the cracked layer, t^k , and the normalized crack density

parameter, ρ^k . The crack density is defined as the ratio of the thickness of the cracked layer to the average spacing between cracks, d^k .

$$\rho^k = \frac{t^k}{d^k} \quad (5.6)$$

The parameters, τ^k and τ_o^k , represent the in-plane and out-of-plane stresses that would be present in the uncracked laminate.

Computing crack opening energy at every stage of the finite element process would be an awkward and time consuming procedure, so it is desired to find an effective pair of stiffness matrices, \bar{C}_1 and \bar{C}_o , which have the equivalent energy as the cracked laminate. This then satisfies the following expression

$$U_{cracked} = \int_A \left[\frac{1}{2} \mathbf{s}^T \bar{C}_1 \mathbf{s} + \frac{1}{2} \mathbf{s}_o^T \bar{C}_o \mathbf{s}_o \right] dA = \int_A \left[\frac{1}{2} \mathbf{s}^T \mathbf{C}_1 \mathbf{s} + \frac{1}{2} \mathbf{s}_o^T \mathbf{C}_o \mathbf{s}_o \right] dA - \Delta U_{crack} \quad (5.7)$$

The effect of matrix cracking can be seen as a reduction in the values of the matrix \mathbf{C} , yielding a new matrix $\bar{\mathbf{C}}$. It is not sufficient to simply estimate the reduction in \mathbf{Q} for the cracked layer and apply this to calculate $\bar{\mathbf{C}}$, because matrix crack opening causes dissimilar reduction in the extensional and bending stiffnesses. Therefore, the effects of matrix cracking must be calculated separately for each element of \mathbf{C} .

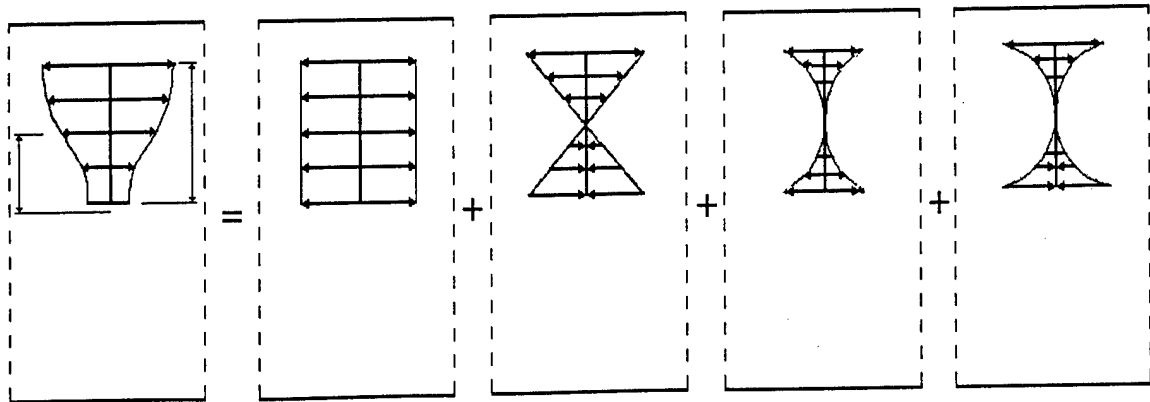


Fig. 5.2. Higher order stress distribution on the crack face.

To determine the effects of matrix cracking, a procedure similar to that developed by Gudmundson and Zang (1993) and Adolfsson and Gudmundson (1997) is used. But unlike their work, which relies on fracture mechanics and the assumption of the crack being in an infinite homogeneous medium, the current technique uses a finite element approach based on the actual laminate configuration. Also, the model developed by Adolfsson and Gudmundson (1997) is based on the classical plate theory that ignores transverse shear stresses. Since a higher order model is used in this paper, additional parameters need to be determined.

Using the principle of superposition, the effective stresses in the cracked laminate are equal to the summation of the stresses corresponding to σ_2 , σ_4 , and σ_6 in the local coordinate system, and to modes I, II, and III crack loading, as seen in Figure 5.2. For the k^{th} layer, this loading can easily be separated into components as follows

$$\tau = \tau_0 + \tau_1\eta + \tau_2\eta^2 + \tau_3\eta^3 \quad \text{for modes I and III} \quad (5.8)$$

$$\tau_o = \tau_{o0} + \tau_{o1}\eta + \tau_{o2}\eta^2 \quad \text{for mode II} \quad (5.9)$$

where

$$\eta = \frac{z - z_k}{\frac{t_k}{2}} \quad (5.10)$$

where z_k is the distance of the layer midplane from the laminate midplane. Thus the stresses on the crack face, τ and τ_o , are cubic and quadratic functions respectively. In matrix form the stresses are expressed as

$$\tau^k = \begin{Bmatrix} \tau_0 \\ \tau_1 \\ \tau_2 \\ \tau_3 \end{Bmatrix} \quad (5.11a)$$

$$\tau_o^k = \begin{Bmatrix} \tau_{o0} \\ \tau_{o1} \\ \tau_{o2} \end{Bmatrix} \quad (5.11b)$$

These components are defined based on the strains in the uncracked laminate as follows

$$\tau_o = \mathbf{T} \mathbf{c} (\varepsilon^0 + z_k \kappa^0 + z_k^3 \kappa^2) \quad (5.12a)$$

$$\tau_1 = \frac{t_k}{2} \mathbf{T} \mathbf{c}_1 (\kappa^0 + 3z_k^2 \kappa^2) \quad (5.12b)$$

$$\tau_2 = \frac{3t_k^2}{4} \mathbf{T} \mathbf{c}_1 z_k \kappa^2 \quad (5.12c)$$

$$\tau_3 = \frac{t_k^3}{8} \mathbf{T} \mathbf{c}_1 \kappa^2 \quad (5.12d)$$

$$\tau_{o0} = \mathbf{T}_o \mathbf{c}_o (\varepsilon_o^0 + z_k^2 \kappa_o^2) \quad (5.13a)$$

$$\tau_{o1} = t_k \mathbf{T}_o \mathbf{c}_o z_k \kappa_o^2 \quad (5.13b)$$

$$\tau_{o2} = \frac{t_k^2}{4} \mathbf{T}_o \mathbf{c}_o \kappa_o^2 \quad (5.13c)$$

where \mathbf{T} and \mathbf{T}_o are the coordinate transformation matrices and \mathbf{c}_1 and \mathbf{c}_o are the stress-strain relations for in-plane and out-of-plane components.

The next step is to relate the stresses to the global strains. The global stress vectors (5.11a,b) are rearranged to form the following relations

$$\tau^k = \begin{bmatrix} \mathbf{I}_3 & z_k \mathbf{I}_3 & z_k^3 \mathbf{I}_3 \\ 0 & \frac{t_k}{2} \mathbf{I}_3 & \frac{3}{2} t_k z_k^2 \mathbf{I}_3 \\ 0 & 0 & \frac{3}{4} t_k^2 z_k \mathbf{I}_3 \\ 0 & 0 & \frac{t_k^3}{8} \mathbf{I}_3 \end{bmatrix} \begin{bmatrix} \mathbf{T} \mathbf{c}_1 & 0 & 0 \\ 0 & \mathbf{T} \mathbf{c}_1 & 0 \\ 0 & 0 & \mathbf{T} \mathbf{c}_1 \end{bmatrix} \mathbf{s} \quad (5.14a)$$

$$\tau_o^k = \begin{bmatrix} \mathbf{I}_2 & z_k^2 \mathbf{I}_2 \\ 0 & t_k z_k \mathbf{I}_2 \\ 0 & \frac{t_k^2}{4} \mathbf{I}_2 \end{bmatrix} \begin{bmatrix} \mathbf{T}_o \mathbf{c}_o & 0 \\ 0 & \mathbf{T}_o \mathbf{c}_o \end{bmatrix} \mathbf{s}_o \quad (5.14b)$$

where \mathbf{I}_j is an identity matrix of rank j . Substituting Eqs. (5.14a,b) into Eq. (5.5) yields the following

$$\Delta U_{crack} = \sum_{k=1}^N \left\{ \int_A \left[\frac{1}{2} t^k \rho^k \left\{ \mathbf{s}^T \begin{bmatrix} \mathbf{T} \mathbf{c}_1 & 0 & 0 \\ 0 & \mathbf{T} \mathbf{c}_1 & 0 \\ 0 & 0 & \mathbf{T} \mathbf{c}_1 \end{bmatrix} \hat{\beta}^{kk} \begin{bmatrix} \mathbf{T} \mathbf{c}_1 & 0 & 0 \\ 0 & \mathbf{T} \mathbf{c}_1 & 0 \\ 0 & 0 & \mathbf{T} \mathbf{c}_1 \end{bmatrix} \mathbf{s} \right\} + \mathbf{s}_o^T \begin{bmatrix} \mathbf{T}_o \mathbf{c}_o & 0 \\ 0 & \mathbf{T}_o \mathbf{c}_o \end{bmatrix} \hat{\beta}_o^{kk} \begin{bmatrix} \mathbf{T}_o \mathbf{c}_o & 0 \\ 0 & \mathbf{T}_o \mathbf{c}_o \end{bmatrix} \mathbf{s}_o \right] dA \right\} \quad (5.15)$$

In the local coordinate system the matrices, $\hat{\beta}^{kk}$ and $\hat{\beta}_o^{kk}$, are diagonal matrices relating the applied stress to crack opening energy.

$$\hat{\beta}^{kk} = \begin{bmatrix} \beta_{00}^{kk} & \beta_{01}^{kk} & \beta_{02}^{kk} \\ \beta_{10}^{kk} & \beta_{11}^{kk} & \beta_{12}^{kk} \\ \beta_{20}^{kk} & \beta_{21}^{kk} & \beta_{22}^{kk} \end{bmatrix} \quad (5.16a)$$

$$\hat{\beta}_o^{kk} = \begin{bmatrix} \beta_o^{kk} & \beta_o^{kk} \\ \beta_o^{kk} & \beta_o^{kk} \end{bmatrix} \quad (5.16b)$$

The component matrices are defined for each geometric variation of the stress as follows

$$\beta_{ij}^{kk} = \begin{bmatrix} 0 & 0 & 0 \\ 0 & \beta_{ij(1)}^k & 0 \\ 0 & 0 & \beta_{ij(3)}^k \end{bmatrix} \quad (5.17a)$$

$$\beta_o^{kk} = \begin{bmatrix} \beta_{ij(2)}^k & 0 \\ 0 & 0 \end{bmatrix} \quad (5.17b)$$

where the nonzero components, $\beta_{ij(1)}^k$, $\beta_{ij(2)}^k$ and $\beta_{ij(3)}^k$, are the stress to energy relations for the specific crack opening modes, I, II and III. The other components are all zero since the matrices

are defined based on the local coordinate system. It can also be shown (Gudmundson and Zang, 1993) that for an elastic material the component matrices are symmetric and that

$$\beta_{ij}^{kk} = \beta_{ji}^{kk} \quad \text{and} \quad \beta_{ij}^{kk} = \beta_{ji}^{kk} \quad (5.18)$$

This results in a system of equations with fifteen unknown parameters. Combining Eqs. (5.7) and (5.15) gives the reduced stiffness matrices.

$$\bar{C}_1 = C_1 - \sum_{k=1}^N \left\{ t^k \rho^k \begin{bmatrix} T c_1 & 0 & 0 \\ 0 & T c_1 & 0 \\ 0 & 0 & T c_1 \end{bmatrix} \hat{\beta}^{kk} \begin{bmatrix} T c_1 & 0 & 0 \\ 0 & T c_1 & 0 \\ 0 & 0 & T c_1 \end{bmatrix} \right\} \quad (5.19a)$$

$$\bar{C}_0 = C_0 - \sum_{k=1}^N \left\{ t^k \rho^k \begin{bmatrix} T_0 c_0 & 0 \\ 0 & T_0 c_0 \end{bmatrix} \hat{\beta}_0^{kk} \begin{bmatrix} T_0 c_0 & 0 \\ 0 & T_0 c_0 \end{bmatrix} \right\} \quad (5.19b)$$

Once the damage parameters are known substitution into Eqs. (5.19a,b) gives the stiffness matrices for the laminate containing matrix cracking. It should be noted that this formulation based on crack tip energy does not take into account crack growth, thus it is not useful for predicting further damage evolution. The next step will be to develop an effective method for calculation the damage parameters for an arbitrary laminate.

5.1.2. Finite Element Analysis of a Representative Crack

These parameters could be estimated using closed form solutions if assumptions like those of Adolfsson and Gudmundson (1997) are made. Adolfsson and Gudmundson (1997) used fracture mechanics solutions based on stress intensity factors to relate the load to the work done. Because of the difficulty in obtaining fracture mechanics solutions, it was necessary to use the solutions for cracks in infinite homogeneous media. The accuracy of this assumption varies dramatically based on laminate thickness and material properties.

To develop a more reliable approach, a separate finite element analysis is used to relate the individual loads to changes in work. The separate finite element modeling of the crack

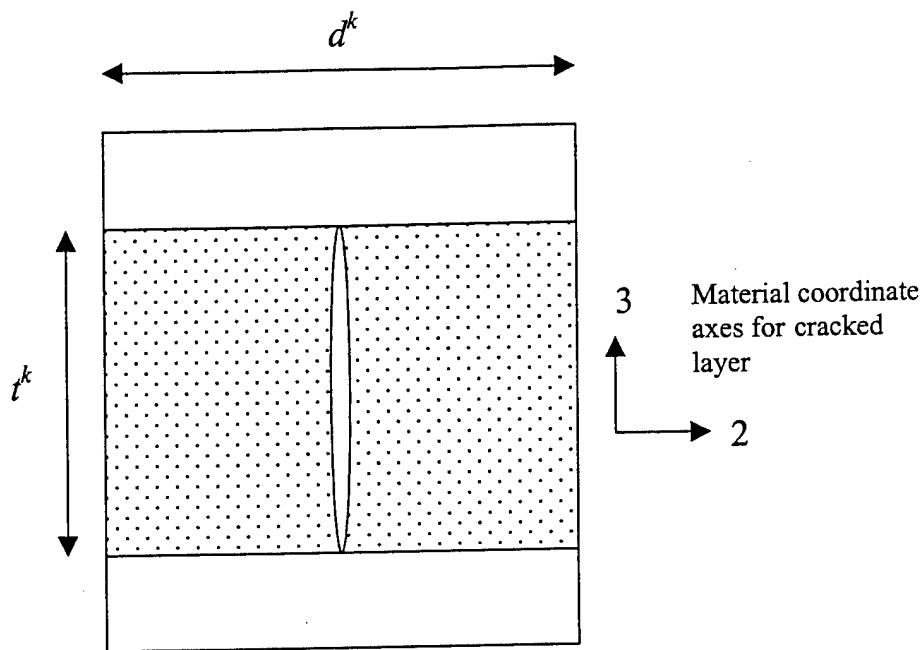


Fig. 5.3. Representative matrix crack used to compute damage parameters.

behavior in each layer with cracks causes definite increases in the computational effort. However, the developed procedure offers advantages that can offset this increase in CPU time. First, the β matrix can be derived for a number of different crack densities, then a simple curve fitting process can be used to express β as a function of crack density. Second, this function can then be stored and reused if the same laminate configuration is encountered again. Therefore, though computational effort is required the first time a new material or laminate configuration is used, subsequent analyses will require very minimal calculations.

The method developed in this work takes a single crack and meshes it with a 2-D finite element grid. The method then enforces the condition of zero global strain. Stresses based on the components of global strain are then applied sequentially to the crack face. The work done by the stress is then calculated for each case. Using these values of work, the damage parameters for Eqs. (5.17a,b) are then computed. The details of this procedure will next be explained.

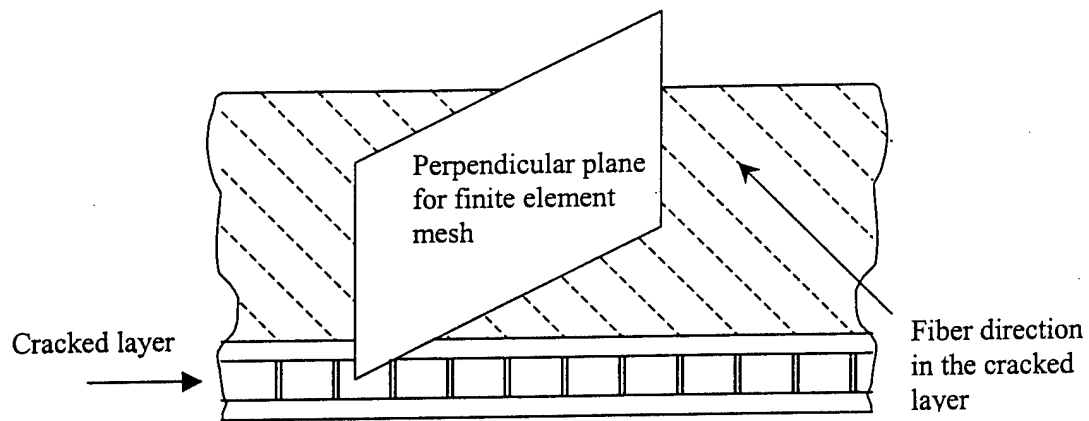


Fig. 5.4. Geometry of perpendicular plane used for the finite element analysis.

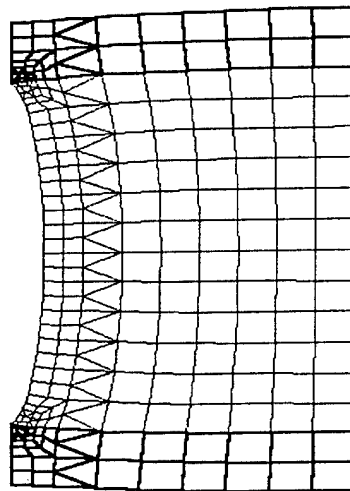


Fig. 5.5. Finite element mesh for representative crack.

Based on the assumption of a uniform distribution of matrix cracks a single cracked segment of the laminate is considered, as shown in Figure 5.3. The cross section perpendicular to the length of the crack, shown in Figure 5.4, is meshed with a two-dimensional finite element grid. Because the matrix crack runs parallel to the fibers, the cross section is oriented perpendicular to the fibers and is in the material 2-3 plane. The use of this cross section orients the coordinate system so that no coordinate transformation is necessary during these

computations. The resulting mesh is shown in Fig. 5.5 with the deformation induced by the applied stresses.

The finite elements are eight noded serendipity quadrilateral elements with three degrees of freedom per node, as shown in Fig. 5.6a. Two degrees of freedom represent the usual displacements within the plane of the mesh, but a third degree of freedom is added to represent out-of-plane displacement caused by pure shear (σ_{12} in the material coordinate system or Mode III crack opening). These displacements are referred to as u_1 , u_2 and u_3 , corresponding to displacements along the material 1-, 2- and 3- axes. The nodes on the sides of the elements are located at the midpoint for all elements except those at the crack tip. The elements adjacent to the crack tip are quarter point crack tip elements, as seen in Fig. 5.6b, with nodes at the quarter point from the tip in order to model the singularity that exists at the crack tip. This method ensures that accurate results are obtained using a reasonable number of nodes.

To obtain the three-dimensional stress tensor from the two-dimensional mesh, the assumption is made that the displacements do not vary with respect to the coordinate perpendicular to the plane of the mesh. Since the 2-D mesh is aligned with the 2-3 material axes, the following assumption is made.

$$\frac{\partial u_1}{\partial x_1} = \frac{\partial u_2}{\partial x_1} = \frac{\partial u_3}{\partial x_1} = 0 \quad (5.20)$$

The strain is now approximated as follows

$$\varepsilon = \begin{Bmatrix} \frac{\partial u_1}{\partial x_1} \\ \frac{\partial u_2}{\partial x_2} \\ \frac{\partial u_3}{\partial x_3} \\ \frac{\partial u_2}{\partial x_3} + \frac{\partial u_3}{\partial x_2} \\ \frac{\partial u_1}{\partial x_3} + \frac{\partial u_3}{\partial x_1} \\ \frac{\partial u_1}{\partial x_2} + \frac{\partial u_2}{\partial x_1} \end{Bmatrix} \approx \begin{Bmatrix} 0 \\ \frac{\partial u_2}{\partial x_2} \\ \frac{\partial u_3}{\partial x_3} \\ \frac{\partial u_2}{\partial x_3} + \frac{\partial u_3}{\partial x_2} \\ \frac{\partial u_1}{\partial x_3} \\ \frac{\partial u_1}{\partial x_2} \end{Bmatrix} \quad (5.21)$$

This strain vector is then used to compute the elemental stiffness using the finite element method.

The element stiffnesses are computed for each element and added to the global system matrix. Since the work must be computed for crack opening under zero global strain, boundary conditions are enforced on the nodes on the end of the finite element mesh. Also, because the crack section is from the middle of a distribution of cracks, the ends must represent a symmetric boundary with other crack sections. Based on these two conditions the displacement for all nodes on the end are fixed in the material 1- and 2- directions and the displacement of the midpoint of the end is fixed in the 3- direction. The system stiffness matrix is symmetric positive definite, so a Cholevsky decomposition can be used to solve the system.

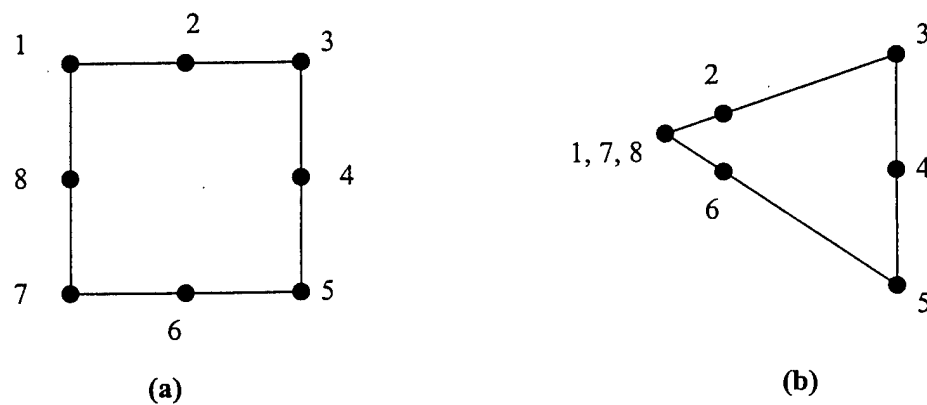


Fig. 5.6. Serendipity (a) and crack tip (b) finite elements used to analyze representative matrix crack.

There are fifteen unknown parameters, so fifteen work computations must be made to gain enough information to solve for every parameter. Crack opening occurs only for those strains which create a stress on the crack surface. Thus the only strains that need to be considered are combinations of $\varepsilon_2^0, \kappa_2^0, \kappa_2^2, \varepsilon_6^0, \kappa_6^0, \kappa_6^2, \varepsilon_4^0, \kappa_4^2$. The stress applied to the crack face is then calculated using the following

$$\begin{Bmatrix} \tau_1 \\ \tau_2 \\ \tau_6 \end{Bmatrix} = \mathbf{c}_1 \begin{Bmatrix} 0 \\ \varepsilon_2^0 + z(\kappa_2^0 + z^2 \kappa_2^2) \\ \varepsilon_6^0 + z(\kappa_6^0 + z^2 \kappa_6^2) \end{Bmatrix} \quad (5.22a)$$

$$\begin{Bmatrix} \tau_4 \\ \tau_5 \end{Bmatrix} = \mathbf{c}_0 \begin{Bmatrix} \varepsilon_4^0 + z^2 \kappa_4^2 \\ 0 \end{Bmatrix} \quad (5.22b)$$

Fifteen combinations of the strains $\varepsilon_2^0, \kappa_2^0, \kappa_2^2, \varepsilon_6^0, \kappa_6^0, \kappa_6^2, \varepsilon_4^0, \kappa_4^2$ are used to create fifteen stress distributions on the crack face. The deformation associated with each combination is then computed using back-substitution on the decomposed stiffness matrix. The work is then computed by integrating the product of the stress and displacement over the crack face.

Using Eq. (5.15) the work for the following fifteen combinations of strain can be computed

$$\varepsilon_2^0 \text{ only} \Rightarrow W_1 = \frac{t_k^2}{2} (c_{22})^2 \beta_{00(1)}^k (\varepsilon_2^0)^2 \quad (5.23a)$$

$$\kappa_2^0 \text{ only} \Rightarrow W_2 = \frac{t_k^2}{2} (c_{22})^2 \beta_{11(1)}^k (\kappa_2^0)^2 \quad (5.23b)$$

$$\kappa_2^2 \text{ only} \Rightarrow W_3 = \frac{t_k^2}{2} (c_{22})^2 \beta_{22(1)}^k (\kappa_2^2)^2 \quad (5.23c)$$

$$\varepsilon_2^0 \text{ and } \kappa_2^0 \Rightarrow W_4 = \frac{t_k^2}{2} (c_{22})^2 \left\{ \beta_{00(1)}^k (\varepsilon_2^0)^2 + \beta_{11(1)}^k (\kappa_2^0)^2 + 2\beta_{01(1)}^k \varepsilon_2^0 \kappa_2^0 \right\} \quad (5.23d)$$

$$\varepsilon_2^0 \text{ and } \kappa_2^2 \Rightarrow W_5 = \frac{t_k^2}{2} (c_{22})^2 \left\{ \beta_{00(1)}^k (\varepsilon_2^0)^2 + \beta_{22(1)}^k (\kappa_2^2)^2 + 2\beta_{02(1)}^k \varepsilon_2^0 \kappa_2^2 \right\} \quad (5.23e)$$

$$\kappa_2^o \text{ and } \kappa_2^2 \Rightarrow W_6 = \frac{t_k^2}{2} (c_{22})^2 \left\{ \beta_{00(1)}^k (\kappa_2^o)^2 + \beta_{11(1)}^k (\kappa_2^2)^2 + 2\beta_{01(1)}^k \kappa_2^o \kappa_2^2 \right\} \quad (5.23f)$$

$$\varepsilon_6^o \text{ only} \Rightarrow W_7 = \frac{t_k^2}{2} (c_{66})^2 \beta_{00(3)}^k (\varepsilon_6^o)^2 \quad (5.23g)$$

$$\kappa_6^o \text{ only} \Rightarrow W_8 = \frac{t_k^2}{2} (c_{66})^2 \beta_{11(3)}^k (\kappa_6^o)^2 \quad (5.23h)$$

$$\kappa_6^2 \text{ only} \Rightarrow W_9 = \frac{t_k^2}{2} (c_{66})^2 \beta_{22(3)}^k (\kappa_6^2)^2 \quad (5.23i)$$

$$\varepsilon_6^o \text{ and } \kappa_6^o \Rightarrow W_{10} = \frac{t_k^2}{2} (c_{66})^2 \left\{ \beta_{00(3)}^k (\varepsilon_6^o)^2 + \beta_{11(3)}^k (\kappa_6^o)^2 + 2\beta_{01(3)}^k \varepsilon_6^o \kappa_6^o \right\} \quad (5.23j)$$

$$\varepsilon_6^o \text{ and } \kappa_6^2 \Rightarrow W_{11} = \frac{t_k^2}{2} (c_{66})^2 \left\{ \beta_{00(3)}^k (\varepsilon_6^o)^2 + \beta_{22(3)}^k (\kappa_6^2)^2 + 2\beta_{02(3)}^k \varepsilon_6^o \kappa_6^2 \right\} \quad (5.23k)$$

$$\kappa_6^o \text{ and } \kappa_6^2 \Rightarrow W_{12} = \frac{t_k^2}{2} (c_{66})^2 \left\{ \beta_{00(3)}^k (\kappa_6^o)^2 + \beta_{11(3)}^k (\kappa_6^2)^2 + 2\beta_{01(3)}^k \kappa_6^o \kappa_6^2 \right\} \quad (5.23l)$$

$$\varepsilon_4^o \text{ only} \Rightarrow W_{13} = \frac{t_k^2}{2} (c_{44})^2 \beta_{00(2)}^k (\varepsilon_4^o)^2 \quad (5.23m)$$

$$\kappa_4^2 \text{ only} \Rightarrow W_{14} = \frac{t_k^2}{2} (c_{44})^2 \beta_{11(2)}^k (\kappa_4^2)^2 \quad (5.23n)$$

$$\varepsilon_4^o \text{ and } \kappa_4^2 \Rightarrow W_{15} = \frac{t_k^2}{2} (c_{44})^2 \left\{ \beta_{00(2)}^k (\varepsilon_4^o)^2 + \beta_{11(2)}^k (\kappa_4^2)^2 + 2\beta_{01(2)}^k \varepsilon_4^o \kappa_4^2 \right\} \quad (5.23p)$$

Using the work computed using the finite element model for each case, the matrix cracking damage parameters can be computed.

$$\beta_{00(1)}^k = \frac{2W_1}{t_k^2 (c_{22})^2 (\varepsilon_2^o)^2} \quad (5.24a)$$

$$\beta_{11(1)}^k = \frac{2W_2}{t_k^2 (c_{22})^2 (\kappa_2^o)^2} \quad (5.24b)$$

$$\beta_{22(1)}^k = \frac{2W_3}{t_k^2(c_{22})^2(\kappa_2^2)^2} \quad (5.24c)$$

$$\beta_{01(1)}^k = \frac{W_4 - W_2 - W_1}{t_k^2(c_{22})^2 \varepsilon_2^0 \kappa_2^0} \quad (5.24d)$$

$$\beta_{02(1)}^k = \frac{W_5 - W_3 - W_1}{t_k^2(c_{22})^2 \varepsilon_2^0 \kappa_2^2} \quad (5.24e)$$

$$\beta_{12(1)}^k = \frac{W_6 - W_3 - W_2}{t_k^2(c_{22})^2 \kappa_2^0 \kappa_2^2} \quad (5.24f)$$

$$\beta_{00(3)}^k = \frac{2W_7}{t_k^2(c_{66})^2(\varepsilon_6^0)^2} \quad (5.24g)$$

$$\beta_{11(3)}^k = \frac{2W_8}{t_k^2(c_{66})^2(\kappa_6^0)^2} \quad (5.24h)$$

$$\beta_{22(3)}^k = \frac{2W_9}{t_k^2(c_{66})^2(\kappa_6^2)^2} \quad (5.24i)$$

$$\beta_{01(3)}^k = \frac{W_{10} - W_8 - W_7}{t_k^2(c_{66})^2 \varepsilon_6^0 \kappa_6^0} \quad (5.24j)$$

$$\beta_{02(3)}^k = \frac{W_{11} - W_9 - W_7}{t_k^2(c_{66})^2 \varepsilon_6^0 \kappa_6^2} \quad (5.24k)$$

$$\beta_{12(3)}^k = \frac{W_{12} - W_9 - W_8}{t_k^2(c_{66})^2 \kappa_6^0 \kappa_6^2} \quad (5.24l)$$

$$\beta_{00(2)}^k = \frac{2W_{13}}{t_k^2(c_{44})^2(\varepsilon_4^0)^2} \quad (5.24m)$$

$$\beta_{11(2)}^k = \frac{2W_{14}}{t_k^2(c_{44})^2(\kappa_4^2)^2} \quad (5.24n)$$

$$\beta_{01(2)}^k = \frac{W_{15} - W_{14} - W_{13}}{t_k^2(c_{44})^2 \varepsilon_4^0 \kappa_4^2} \quad (5.24p)$$

This procedure is conducted for each layer containing matrix cracking. Once the damage parameters have been computed, they can be used give the reduced laminate stiffness matrix when analyzing the response of the structure containing the cracking.

5.2. *Bimodularity Effects*

Modeling of a composite plate with matrix cracking and delamination will be accomplished using the following steps. First, reduced stiffness values will be determined for layers containing matrix cracks using the separate finite element model described above. Each cracked layer will be analyzed individually and given its own reduced stiffness values. The plate will then be modeled using the higher order theory and the finite element method. Once the finite element stiffness matrix for the plate is formed, continuity conditions will be enforced between the regions as described in the previous chapter. However, a problem that is encountered is that Mode I crack opening does not occur when the crack is under compression. Thus, the composite laminate has a different stiffness depending upon the state of stress. This phenomenon is known as bimodularity.

For static problems, bimodularity can be addressed by using an iterative technique. The neutral axis, the location in the z direction where the stress is zero, is first assumed and compressive stiffness properties are applied to the layers under compression and tensile stiffness properties are applied to the layers under tension. The displacements are then determined, and a new neutral axis is calculated. The stiffness matrix is recalculated using the new value and the problem is solved again. The iteration continues until the neutral axis converges to a final value. For the case of matrix cracking, few iterations are required since the difference in overall laminate stiffness for varying locations of the neutral axis is relatively small, compared to the bimodularity that results in such materials as Kevlar-rubber composites.

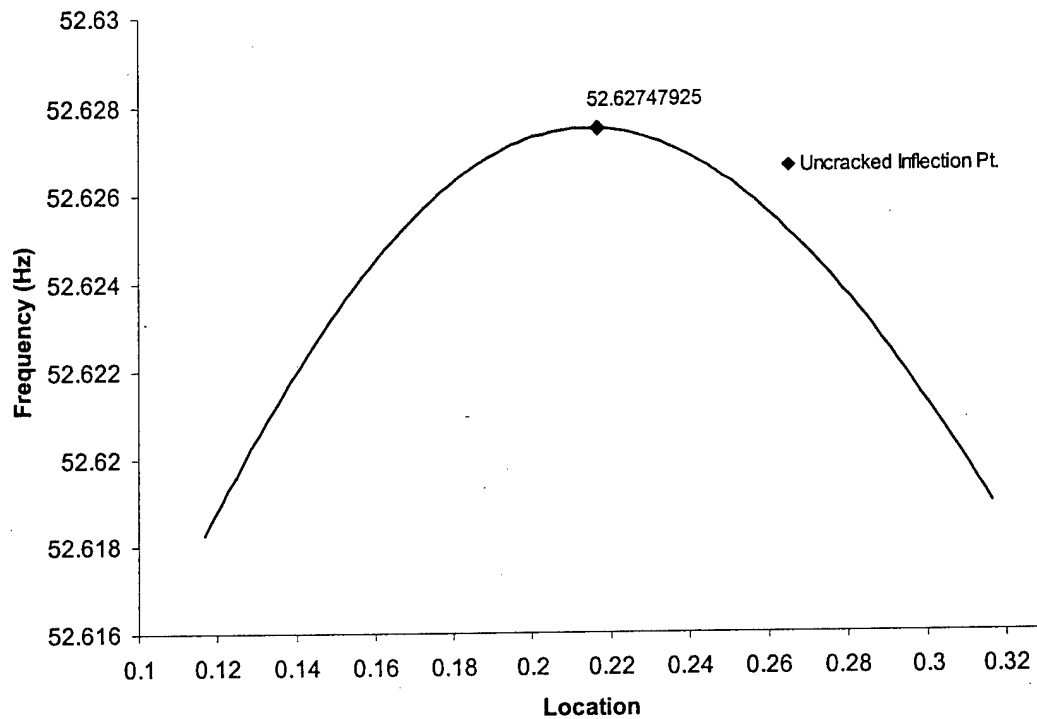


Fig. 5.7. Natural frequency for mode 2 inflection point location for $[0,90_2]_{2s}$ glass-epoxy laminate.

When solving for plate vibration, the nonlinearity associated with the bimodularity of matrix cracking means that superposition of vibration modes is not applicable. Natural frequency values can no longer be calculated using standard eigenvalue analysis since the plate stiffness is dependent upon the deflection shape, or more specifically, whether the plate is in compression or tension. The natural frequencies can be solved for individually if the mode shape was known and used to calculate the correct stiffness matrix. Fortunately, the bimodularity introduced by matrix cracking is relatively small and results in only very small changes in the mode shape from the uncracked case to the case with matrix cracks. To demonstrate this, the technique of Wu, Jing and Chin (1989) is used to solve a transfer matrix model of a cantilever beam with matrix cracks. The natural frequency is calculated assuming different locations for the inflection points, and the local maximum or minimum represents the actual natural frequency. The results are shown for a

$[0,90_2]_{2s}$ glass-epoxy laminate with saturation cracking in all of the 90° layers ($\rho_k=1.0$). This model was chosen since matrix cracking has a large effect in glass-epoxy and laminates with a large number of 90° plies. Figure 5.7 shows the results corresponding to the second mode of vibration. The symbol “ \diamond ” represents the inflection point for the uncracked laminate and it is apparent that the inflection point has shifted only a very small distance. Also, the error introduced in the natural frequency, if the calculations were made using the uncracked mode shape, is on the order of 0.01%. This is so small because near the inflection point, the bending stresses are always small and small changes in the stiffness have little effect. The third mode, shown in Fig. 5.8, demonstrates similar behavior. However, in this case, there are two inflection points, resulting in a surface plot. Again, the shift in inflection point locations is small and has little effect on the calculated natural frequency.

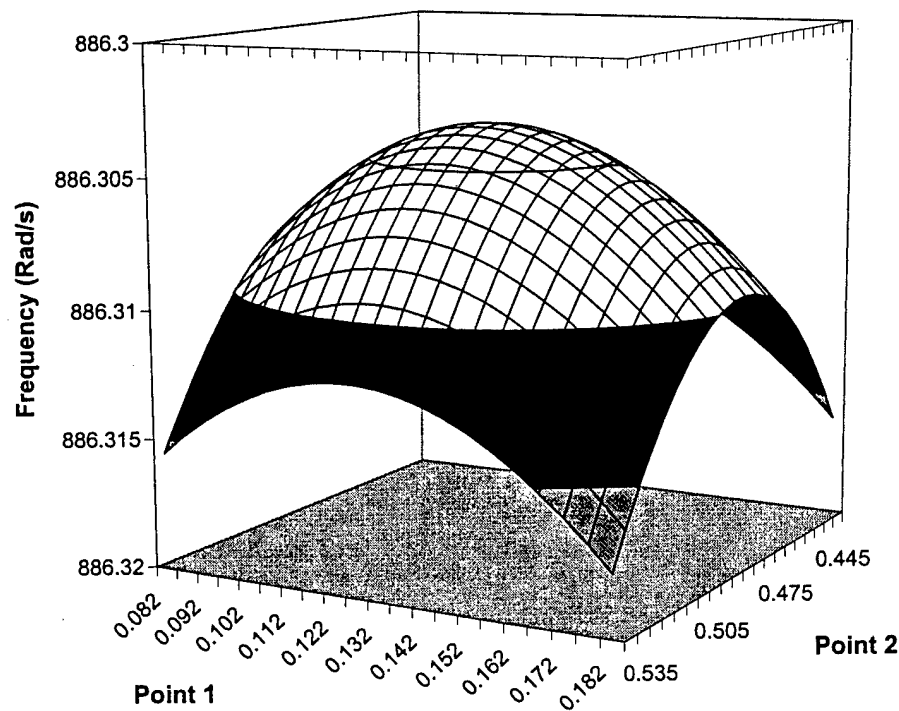


Fig. 5.8. Natural frequency for mode 3 inflection point location for $[0,90_2]_{2s}$ glass-epoxy laminate.

The results from this model show that good estimates of the natural frequency can be obtained by using the uncracked mode shapes in the calculation of the stiffness matrix. The accuracy is further improved by using an iterative process during the natural frequency calculation where the uncracked mode shape is used as an initial starting point in the calculation of the stiffness matrix. The natural frequency and mode shape are determined next using eigen value analysis and the new mode shape is used to recalculate the stiffness matrix. This process is continued until convergence of the inflection points and neutral axes are achieved.

During plate vibration, bimodularity can create further complexities if varying amounts of cracking exist in each of the different layers. In such case, the structure will have different stiffness depending upon whether the plate is being bent up or down. Thus, the period for each half-cycle during vibration at a natural frequency is different, and the overall natural frequency (ω) is determined by

$$\omega = \frac{2}{\omega_1^{-1} + \omega_2^{-1}} \quad (5.25)$$

where ω_1 and ω_2 are the natural frequencies for each half-cycle (Bert, et al., 1989). In other words, to calculate the overall natural frequency (ω) the plate is analyzed first for the upward deflection case (ω_1), and then again for the downward deflection case (ω_2).

5.3. Results

In this section results are presented using the developed model for transverse matrix cracking. The reduction in laminate stiffness caused by matrix cracking is first examined and the results from the model are compared with experimental data and results from other researchers. Next, matrix cracking is included in the modeling vibration in laminate structures, and its effect on the dynamic response is examined.

Table 5.1.

Material properties used for matrix cracking comparison.

Property	Graphite-epoxy	Glass-epoxy
E_1 (GPa)	144.8	41.7
E_2 (GPa)	9.6	13.0
ν_{12}	0.31	0.30
ν_{23}	0.461	0.42
G_{12} (GPa)	4.8	3.40
G_{23} (GPa)	3.3	4.58

5.3.1. Stiffness Reduction

The first step is to verify that the developed model accurately predicts the loss of laminate stiffness. This is done by modeling sample composite plates and comparing the results with published experimental results. Results show that this technique accurately predicts the reduction in stiffness for a variety of materials and laminate configurations.

Shown in Figs. 5.9 and 5.10 are the reductions in extensional and bending stiffness for cracked laminates of $[0,90_2]_s$ graphite-epoxy and $[0,90_3]_s$ glass-epoxy, respectively. The results obtained from the present model are compared with the experimental results from Highsmith and Reifsnider (1982) for the glass-epoxy laminate. For the graphite-epoxy laminate the experimental work of Groves (1986) is used. The material properties for the two composite laminates are listed in Table 5.1. Though the elastic moduli of the two composite materials are very different, the present model shows good correlation in both cases. This is in contrast to other models whose accuracy depends upon the type of composite laminate examined.

Due to a lack of sufficient experimental data on the effects of bending in the literature, ANSYS finite element models are used for validation. Finite element modeling of a cracked structure is difficult to accomplish effectively and efficiently, thus motivating the current research. Individual matrix cracks are spaced apart by a distance on the order of one or two ply

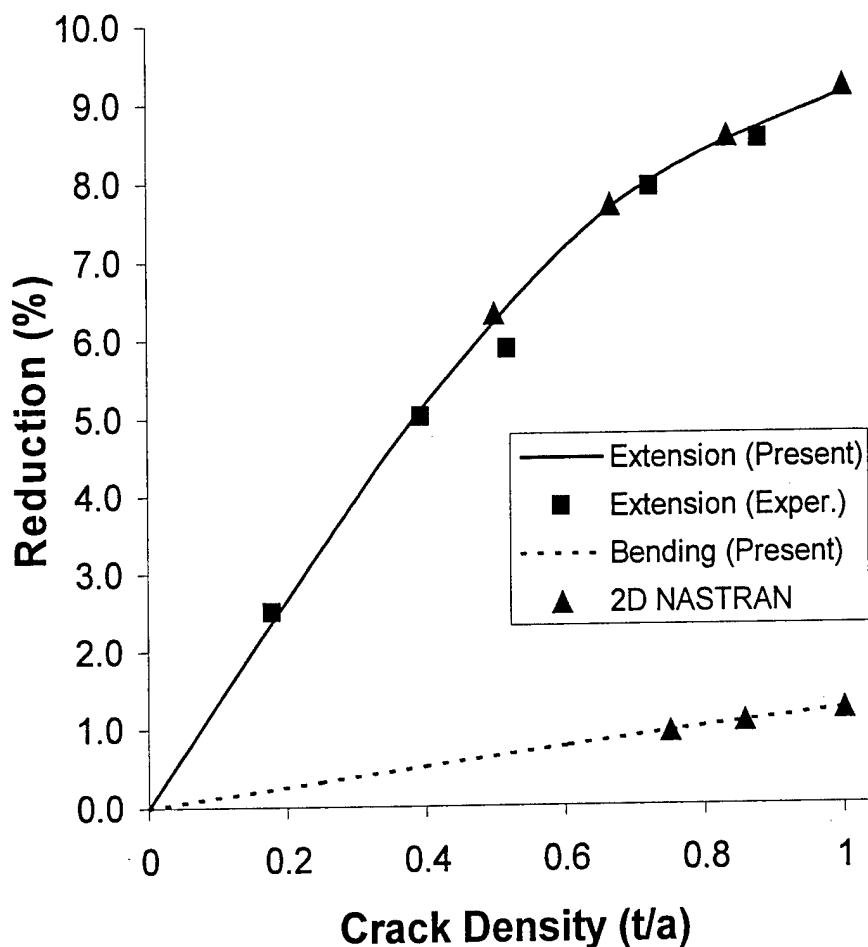


Fig. 5.9. Stiffness loss of graphite-epoxy $[0,90_2]_s$ laminate.

thicknesses, thus a single composite specimen will likely have hundreds of matrix cracks. The desire for accurate results motivates the modeler to use a fairly large number of elements in the vicinity of each crack and particularly near the tips. The geometry of the crack and the variety of loading possibilities motivates the use of a 3D analysis. Such a model would result in a very large number of degrees of freedom. Thus for verification two slightly simplified NASTRAN and ANSYS models are used. The first is a 2D plane-strain NASTRAN model of the cross section of a composite laminate containing a small number of matrix cracks. The spacing of the cracks is varied slightly to reflect a realistic distribution. The plate model is then loaded and the average strains are compared to the results from an uncracked model of the same composite cross

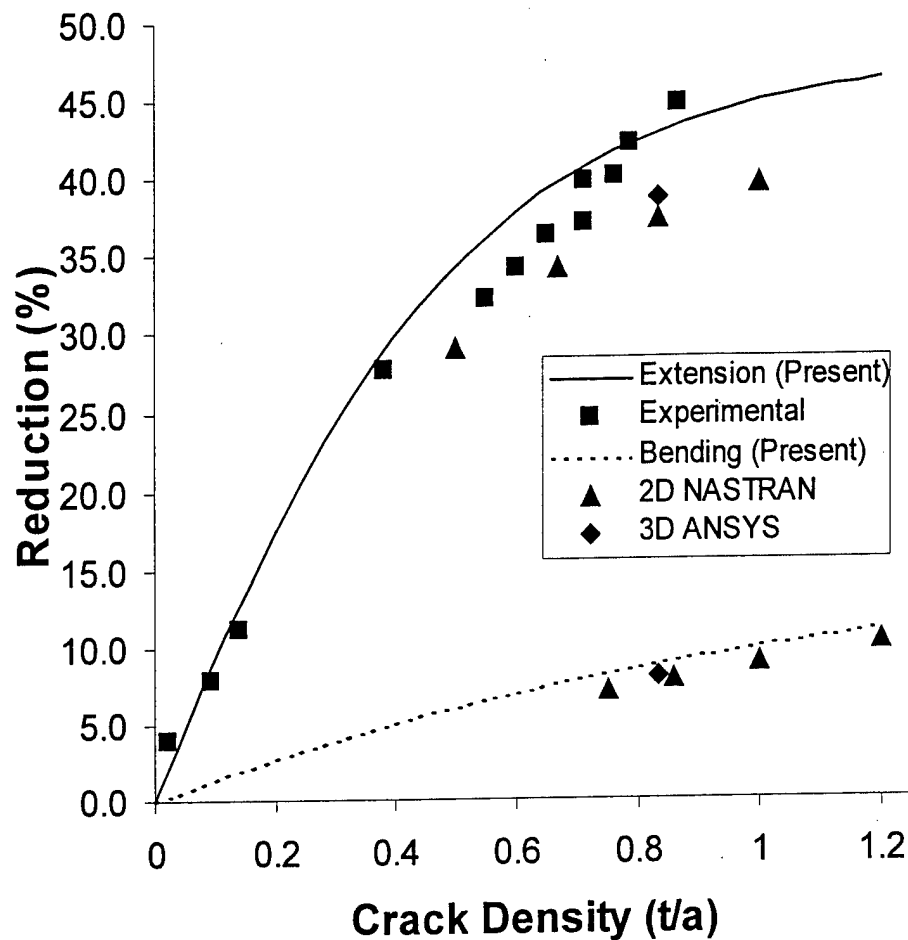


Fig. 5.10. Stiffness loss of glass-epoxy $[0,90]_s$ laminate.

section. The second model is a 3D ANSYS mesh of a single representative crack. The rationale behind this model is a comparison versus the plane strain assumption. The size of this model is considerably larger in spite of modeling a single crack, and enforcement of the boundary conditions involved significant effort. The reduction in bending stiffness is significantly smaller compared to the reduction in extensional stiffness, due to the fact that matrix crack opening is much smaller during bending than it is during extension. Due to this reason, models that are designed for predicting extensional stiffness should not be used to determine bending stiffness.

Figure 5.11 presents a comparison of the present model with the experimental results from Highsmith and Reifsnider (1982), as well as with the other available techniques. These

techniques include the work by Allen and Lee (1991), Hashin (1986) and Adolfsson and Gudmundson (1997). The present model correlates well with the experimental results and asymptotically approaches the ply discount method. Unlike Hashin's method, which can only be used to study a few specialized cross-ply laminates, the present approach is applicable to any laminate configuration.

The results shown thus far have all examined the extensional stiffness of cross-ply laminates. Matrix cracking also affects the shear stiffness of the laminate. This affect can be seen by not only looking at the shear stiffness of cross-ply laminates, but also by examining the extensional stiffness of angle ply laminates. Figure 5.12 shows the reduction in stiffness for a $[0, \pm 45]_s$ glass-epoxy laminate. In this case, the crack occurs only in the angle ply layers and both

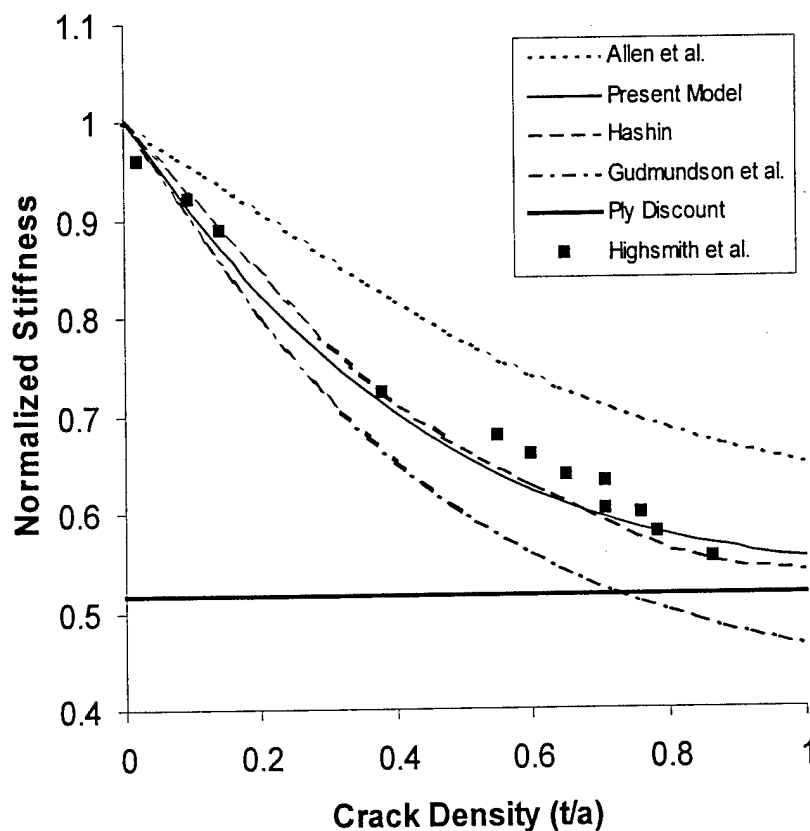


Fig. 5.11. Normalized extensional stiffness of glass-epoxy $[0,90]_s$ laminate.

the $+45^\circ$ and -45° layers are assumed to have equal crack densities. Again the current model has good agreement with the experimental data (Highsmith, et al., 1981), even in the presence of increased in-plane shear forces due to the angle plies. Figure 5.13 presents the reduction in the shear modulus for a $[0,90_2]_s$ graphite-epoxy cross-ply laminate with cracking in the inner layer as compared to the experimental data of Tsai and Daniel (1992). This is the only experimental data available in the literature on the affect on matrix cracking on shear stiffness. Again the developed model shows good correlation with the experimental results. There is a more noticeable difference between the model and experiments than seen in previous results. This is most likely due to the difficulty in accurately measuring shear the modulus of composite laminates and it should be noted that the experimental results do not seem to converge to zero reduction for zero crack density.

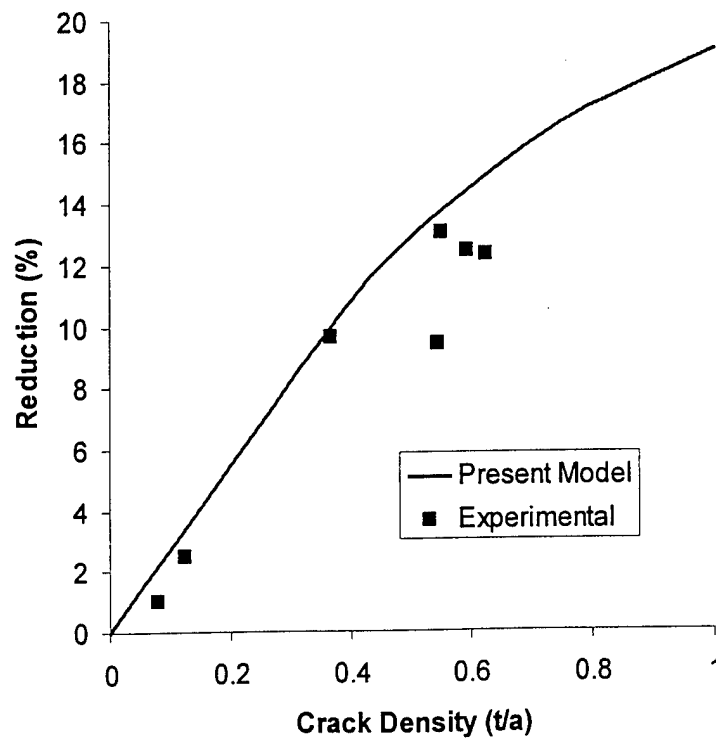


Fig. 5.12. Extensional stiffness loss of $[0,\pm 45]_s$ glass-epoxy laminate.

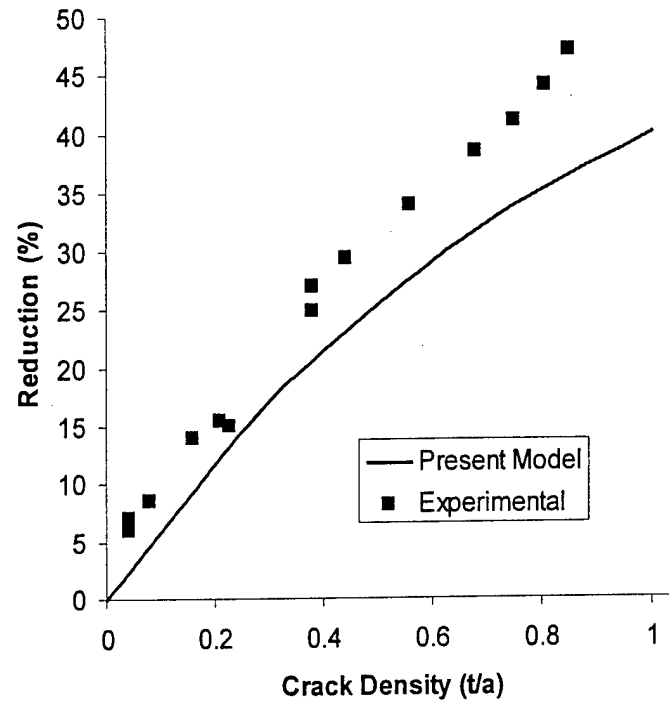


Fig. 5.13. Reduction in shear modulus of $[0,90_2]_s$ graphite-epoxy laminate.

5.3.2. Plate Vibration with Matrix Cracking

Figure 5.14 shows the effect of matrix crack density on natural frequency for the same $[0,90_2]_s$ glass-epoxy cantilever plate discussed above. The first case is for cracking only in the upper 90° layer and the second case is for cracking in all 90° layers. The asymmetric amount of cracking in case 1 results in differing frequencies for each half-cycle (ω_1 and ω_2 in Fig. 5.14). This effect is most apparent for mode 1, where all of the cracks are closed during the upward deflection, ω_1 . Since the cracks close, their only effect is on transverse shear, and they have little effect on natural frequency. During the downward deflection, ω_2 , all of the cracks open causing a significant loss in stiffness, thus reducing the natural frequency. For case 2, since the cracking is symmetric, the upward and downward deflections have the same behavior, and the half-cycles do not have different frequencies. For the higher modes, the upward and downward deflections

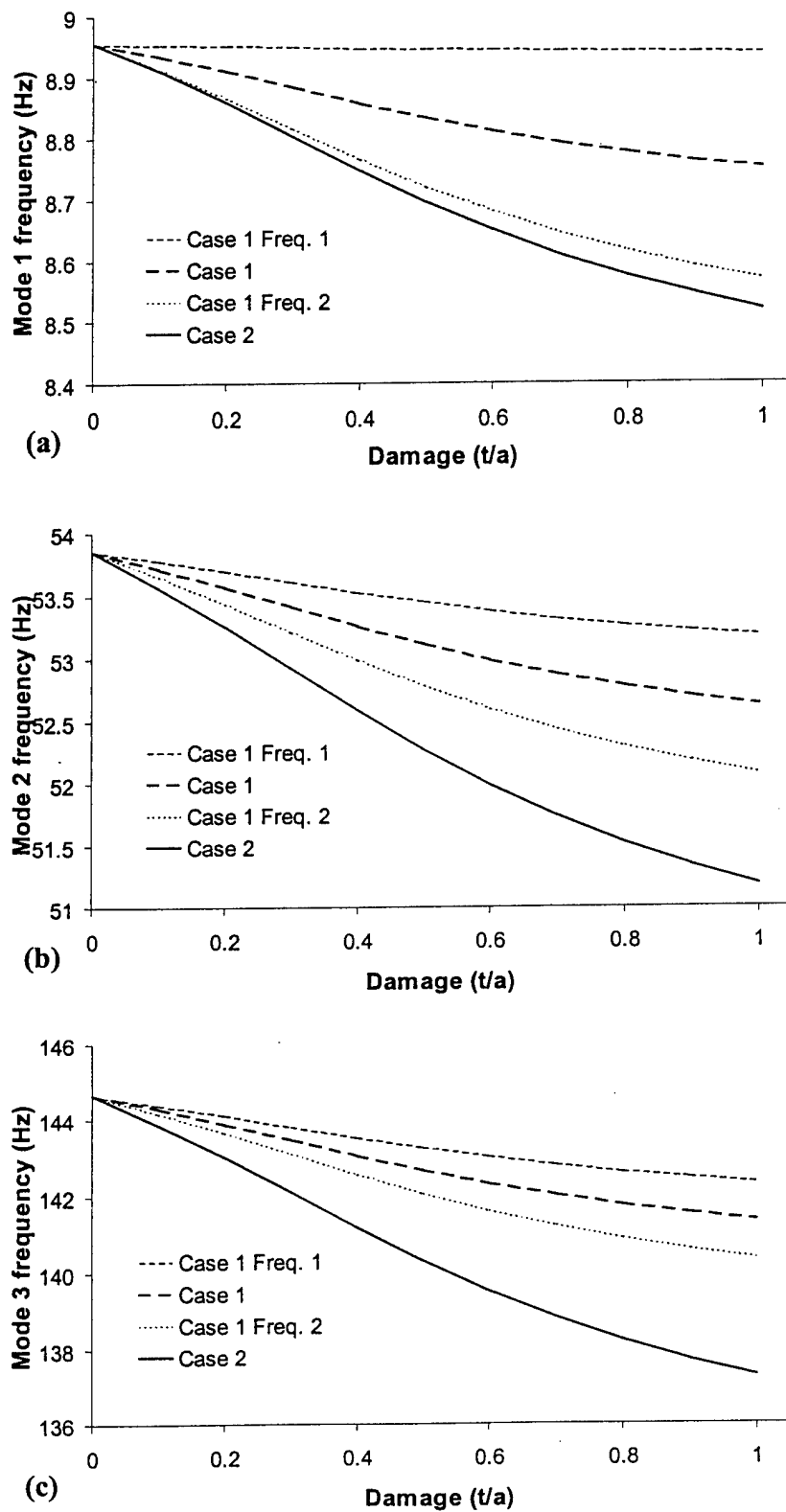


Fig. 5.14.(a), (b), (c) Effect of matrix cracking on natural frequencies for a $[0,90_2]_{2s}$ glass-epoxy cantilever plate.

create both areas with closed cracks and areas with open cracks, thus decreasing the difference in the two half-cycle frequencies.

Next, results are presented for cases where matrix cracks are accompanied by delamination. Figure 5.15 shows an example of how matrix cracking can have significant effect on structural behavior that is often not considered. Shown in this figure is the effect of delamination in a $[0,90]_{2s}$ graphite-epoxy cantilever plate, as measured by Shen and Grady (1992). The example shown is for a through the width delamination between the first 90° layer and the second 0° layer. Results are shown for the case of no matrix cracks and the case of cracking in all 90° layers ($\rho=1.0$). The present theory uses a finite element mesh with 40 elements and 504 degrees of freedom. It can be seen that the effect of matrix cracking is comparable in magnitude to the effect of the delamination. Also, delamination area increases the effect of matrix cracking, as seen by a larger reduction in natural frequency at high delamination

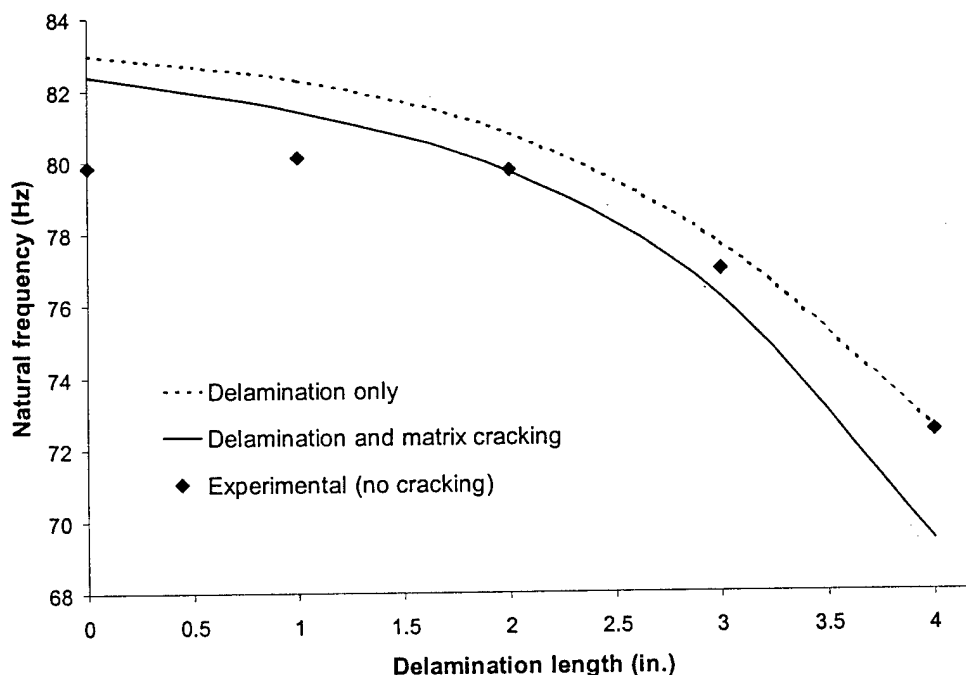


Fig. 5.15. Natural frequency of a delaminated graphite-epoxy $[0,90]_{2s}$ cantilever plate.

lengths. This is due to the fact that the delamination creates a new surface within the laminate and cracks originally internal to the laminate are now on the surface, which dramatically increases their effect on stiffness. This example shows that matrix cracking and delamination need to be addressed simultaneously when studying the effect of damage on composite laminates.

6. Adaptive Structure Optimization

Having modeled the adaptive structural system, the next consideration is how to optimize that system for maximum performance. Optimization of adaptive structures is a popular area of study, but only a limited amount of work has been done on simultaneously optimizing both structural and electrical aspects of a system. A common application of the electrical interaction with the structural deformation is in the design of passive electrical damping systems. Work has been done on defining optimal electrical parameters for the damping circuit, but, in general, very simple structural models were used that do not take into account the complex state of strain that may exist in the piezoelectric patches. In addition, the placement of the piezoelectric patch has not been considered concurrently with the design of the electrical system.

In this chapter it is demonstrated how multidisciplinary optimization (MDO) techniques can be utilized to optimize both structural and electrical aspects of an adaptive structural system. To simultaneously optimize multiple performance requirements, the Kreisselmeier-Steinhauser (K-S) function approach (Wren, 1989; Sethi and Striz, 1997) is used. This technique combines all the objective functions and the constraints to form a single unconstrained composite function to be minimized. Then an unconstrained solver is used to locate the minimum of the composite function. Optimization of an integrated structural and electrical system involves both discrete and continuous variables. The optimization method used in this work is very similar to the hybrid method of Seeley, Chattopadhyay and Brei (1996), with the major difference being that the discrete search and the gradient based search are more independent due to the nature of this particular problem. Since, the present model assumes that only the electrical components to be continuous parameters the gradient based search essentially amounts to finding the optimal set of electrical components for a give structural configuration. Composite plates of varying stacking sequence, boundary conditions and surface bonded actuators are considered.

6.1. Problem Formulation / Description

The objective of the optimization procedure is to minimize the peak response of a composite plate with piezoelectric patches connected to a passive electrical damping circuit. The optimization procedure must determine the optimal combination of plate geometry and electrical components that will result in a tuned damping circuit with the minimum response for a given set of modes. The passive electrical damping circuit is assumed to be composed of linear inductors, resistors and capacitors with values that are determined during the optimization process. Note that the optimization procedure only determines the optimal values for the components and not the configuration of the damping circuit. Other nonlinear electrical components could be used and optimized, but a corresponding increase in computational effort would be expected. The optimization procedure must also take into account location and orientation of the piezoelectric patches on the plate and determine the location that provides for maximum damping.

The mathematical optimization problem is stated as follows

$$\text{Min } f(\phi) \quad (6.1)$$

where

$$\phi = \begin{bmatrix} XC_h \\ YC_h \\ ANG_h \\ R_i \\ L_j \\ C_k \end{bmatrix} \quad \begin{matrix} h = 1 \dots N_a \\ i = 1 \dots N_r \\ j = 1 \dots N_i \\ k = 1 \dots N_c \end{matrix} \quad (6.2)$$

subject to the constraints

$$\begin{aligned} R_i &\geq 0 \\ L_j &\geq 0 \\ C_k &\geq 0 \\ \phi_L &\leq \phi \leq \phi_U \end{aligned} \quad (6.3)$$

where $f(\phi)$ is the objective function representing the peak response of the system for a set of vibrational modes, ϕ is the vector of design variables, N_a is the number of actuators and N_r , N_i , and N_c are the numbers of resistors, inductors and capacitors to be optimized. The design variables include the x- coordinate (XC), the y- coordinate (YC) and the orientation angle (ANG) for each actuator and the resistance (R), inductance (L) and the capacitance values for each electrical component. It is also possible to include ply orientation angles as design variables. Geometric constraints are imposed so that the electrical components maintain positive values in order to represent physical hardware.

6.2. Optimization Technique

The model for piezoelectric system developed in previous chapters is used to model the structural system. For this analysis the structural design variables (XC, YC, ANG) are all chosen to be discrete variables, while the electrical design variables (R, L, C) are all continuous. The x- and y- coordinates of the piezoelectric patch are chosen as discrete variables based on the finite element model of the plate structure. The plate is meshed with a uniform grid of elements and the piezoelectric patches are required to have locations that align the PZT with the mesh. This procedure is used to avoid remeshing of the plate during every optimization iteration. The small numerical variations that result from changing the mesh in a finite element analysis can introduce errors that may lead to sub-optimal designs. Thus, it is more efficient to use a uniform mesh and restrict the PZTs to discrete locations. The analysis can start with a relatively coarse mesh to determine the general coordinates of the optimum location, and then if further accuracy is desired, the process can be repeated using a more refined mesh and the previous optimum solution as a starting point. The orientation angles are included to allow modeling of piezoelectric patches that are not isotropic within the plane of the patch and exert an actuation force in a preferential

direction. These include inter-digitated electrode (IDE) piezoelectric patches (Rodgers, Bent and Hagood, 1996) which are very powerful since they make use of d_{33} actuation.

The optimization formulation is based on the Kreisselmeier-Steinhauser (K-S) function approach. In this technique the multiple objective functions are first transformed into reduced objective functions, which can be expressed as follows

$$\hat{f}_i = (F_i(\phi)/F_{i0}) - 1 - g_{\max} \leq 0 \quad i = 1 \dots \text{number of objective functions} \quad (6.4)$$

where F_{i0} represents the original value of the i th objective function, F_i is its value based on the current design variables and g_{\max} is the largest value of the original constraint vector. These normalized objective functions are now analogous to constraints and are combined into a single vector, $f_m(\phi)$; $m=1,2,\dots,M$, with M being the sum of the number of constraints and the number of objective functions. The constraints and objective functions are then combined into a single composite objective function, $F_{KS}(\phi)$, defined as

$$F_{KS}(\phi) = f_{\max} + \frac{1}{\rho} \ln \sum_{m=1}^M e^{\rho(f_m(\phi) - f_{\max})} \quad (6.5)$$

where f_{\max} is the largest constraint corresponding to the new constraint vector $f_m(\phi)$. The parameter ρ acts as a draw-down factor controlling the distance from the surface of the K-S envelope to the surface of the maximum constraint function.

The optimization algorithm consists of a hybrid scheme that uses simulated annealing to optimize the discrete variables and a continuous search procedure to optimize the continuous variables. Because the K-S function approach reduces the problem to an unconstrained one, any unconstrained gradient based technique can be used for the continuous variables. A modified Newton method is used for the unconstrained. A finite difference scheme is used to calculate the gradient and the Hessian matrix, necessary for determining the search direction. The

computational cost associated with the second-order search is mostly overcome by convergence in significantly fewer iterations compared to other first and zero order search techniques.

The optimization algorithm begins with the simulated annealing procedure and a user defined initial point. The simulated annealing procedure controls the values of the discrete variables only, and attempts to minimize the objective function using a probabilistic approach. Whenever the value of the objective function is requested by the simulated annealing algorithm, the current values of the discrete variables are used to calculate the open circuit eigen values and eigen vectors of the plate. Then an unconstrained search procedure is invoked to minimize the objective function at that point by varying the continuous design variables. Since the continuous variables are the electrical components, the procedure can be described as determining the optimum passive damping circuit for a particular set of PZT locations and orientations. The objective function value returned to the simulated annealing search is the minimum achievable K-S function value determined by the unconstrained search.

When the value of the objective function is required by the unconstrained search, the current values for the continuous variables are used to construct the linear electrical matrices. These are then combined with the reduced structural matrices based on the eigen values and vectors. These equations are then solved to obtain the system response for any disturbance frequency. Next, the frequency response curves are calculated and the maximum response peak is computed at each mode to be minimized. These parameters are then used to calculate the K-S function value.

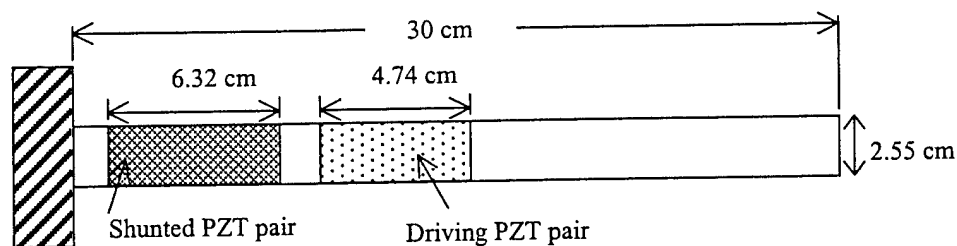


Fig. 6.1. Configuration for the cantilevered plate prior to optimization.

6.3. Results for optimal passive damping systems

The developed optimization procedure is demonstrated first through the integrated design of a cantilevered plate with a single actuator connected to a passive shunt circuit. The cantilevered plate has been studied extensively in the literature related to passive damping and therefor is a good example for benchmarking the developed optimization algorithm. This is due to the fact that for all bending modes, the root is subjected to maximum strain, thus making it the optimal location for a piezoelectric actuator to generate the maximum possibly polarization energy and thereby controlling vibration.

The plate is assumed to be made of 3.17mm thick aluminum and the detailed dimensions are shown in Figure 6.1. A single piezoelectric actuator is placed on one side to induce vibration and a single actuator is placed on the opposite side and is connected to the shunt circuit. The plate is modeled with a 19x3 element finite element mesh and the system is reduced using the first twelve modes. Optimization is performed to minimize the vibratory response associated with the first mode. The design variables include location of the piezoelectric patch and the electrical parameters governing the inductor and the resistor in the passive shunt. In the initial design, the patch is assumed to be at the center of the plate. Results are presented for two configurations, one with the inductor and resistor in series and the other in parallel.

The frequency response curves before and after optimization are shown in Figure 6.2. It can be seen that the optimization algorithm is able to reduce the peak response of the first mode by over an order of magnitude in both cases. The optimum location for the piezoelectric patch is determined by the algorithm to be at the root of the plate, as was expected for a cantilevered plate. The optimum values calculated for the inductor and resistor in series are 422.032 henries and

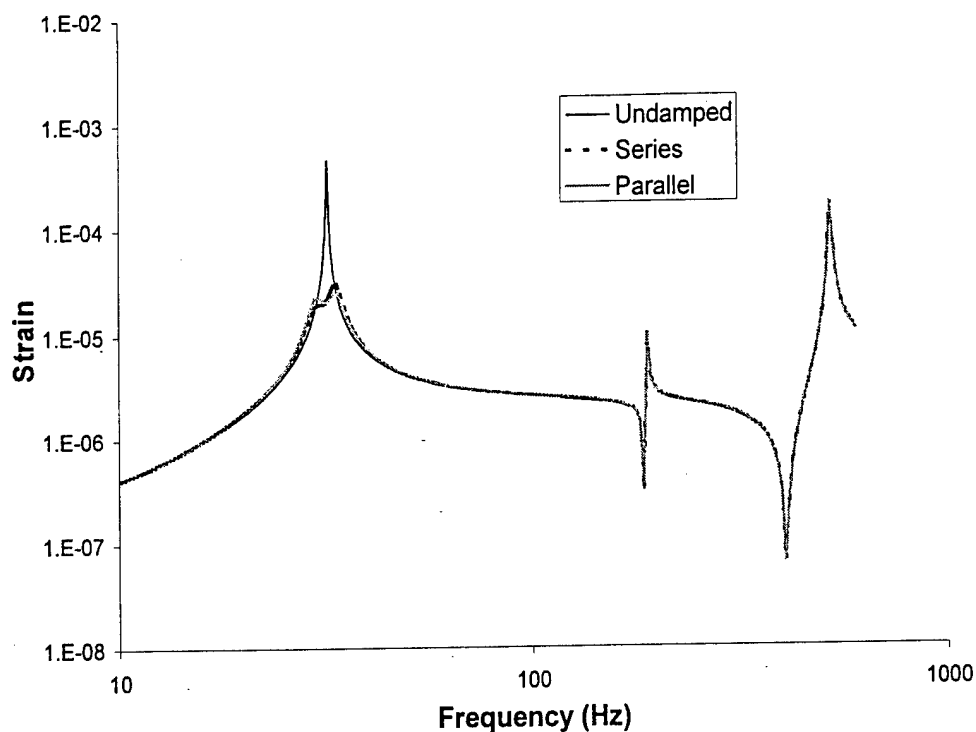


Fig. 6.2. Frequency response curves for a cantilever plate with and without passive damping circuits.

14406 ohms, respectively. For the case with the inductor and resistor in parallel, the corresponding values are 417.927 henries and 489630 ohms.

Next a carbon fiber-epoxy composite plate simply supported on all four sides is considered. This example provides a more interesting design challenge due to the complexity of the mode shapes, which are associated with different locations and orientations of maximum strain. In such cases, it is possible that locations and orientations that are optimal for a particular mode may fall on the inflection lines where strain is minimal for the other modes. In such a case the piezoelectric actuator would not generate any polarization energy during vibration that excites that particular mode, making passive damping of that mode impossible. The piezoelectric actuators used in this example are Active-Fiber Composite (AFC) (Rodgers, Bent and Hagood, 1996) actuators to allow orientation angle of the actuators to be included as design variables. The plate dimensions are 32cm by 32cm with 1.6mm thickness. The initial lay-up for the plate is

eight laminae in $[0,90]_{2s}$ configuration. Vibration is induced by a 2cmx2cm piezoelectric actuator located on the backside of the plate. The plate is modeled with a 16x16 finite element mesh with a single 4cmx4cm AFC actuator located in the center of the plate at zero orientation angle as an initial design.

First, the AFC patch is modeled with a parallel shunt circuit containing one inductor and one resistor in parallel. The system is then optimized to reduce the response peak for each of the first four vibrational modes. The frequency response curves associated with the initial and the optimum configurations are presented in Figures 6.3-6. In each case the targeted mode is reduced by more than a factor of ten, showing the effectiveness of the developed optimization algorithm in damping each of the individual modes. The optimized location of the piezoelectric patch, for the first mode, is the corner of the plate, as illustrated in Figure 6.7. The optimized orientation angle for the AFC patch is 45° and the inductor and resistor assumes values of 110.645 henries and 558307 ohms, respectively. For the second and third modes, the optimal location is predicted to be a quarter of the way inwards from the center of one side. These locations coincide with the center of the maximum out-of-plane deflection as shown in Figures 6.8 and 6.9. For the second mode the optimal actuator angle is 90° , and the inductor and resistor have values of 20.8077 henries and 177846 ohms, respectively. For the third mode the optimal actuator angle is 0° , and the inductor and resistor have values of 12.2968 henries and 138118 ohms, respectively. The optimal location for the forth mode predicted by the optimization algorithm is shown in Figure 6.10. The optimal angle for the actuator is 60° , and the inductor and resistor have values of 7.2863 henries and 192467 ohms, respectively. This location is not intuitively obvious to be the optimal location for the forth mode. However, convergence to this solution was obtained irrespective of the initial design. This particular case further illustrates the necessity of using formal optimization techniques in the design of structures with complex mode shapes.

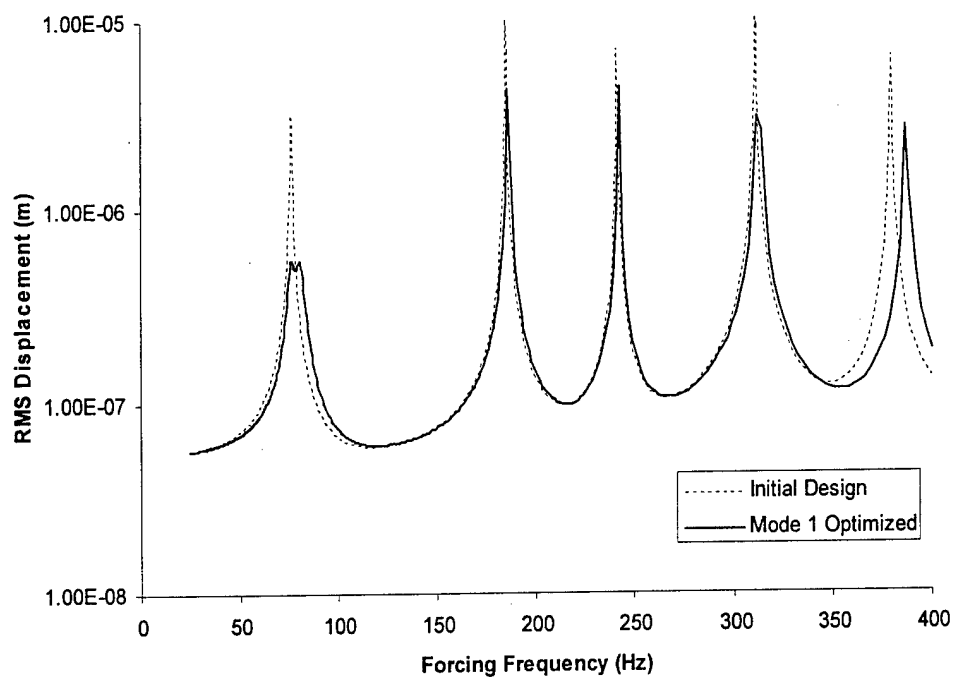


Fig. 6.3. Frequency response curve for the optimal passive damping design using mode 1.

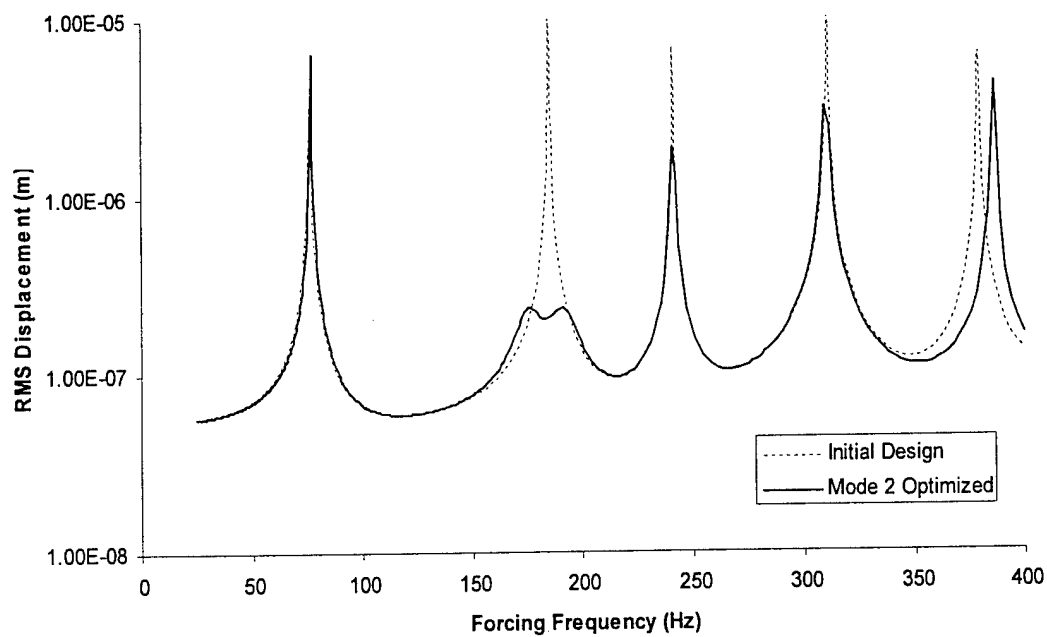


Fig. 6.4. Frequency response curve for the optimal passive damping design using mode 2.

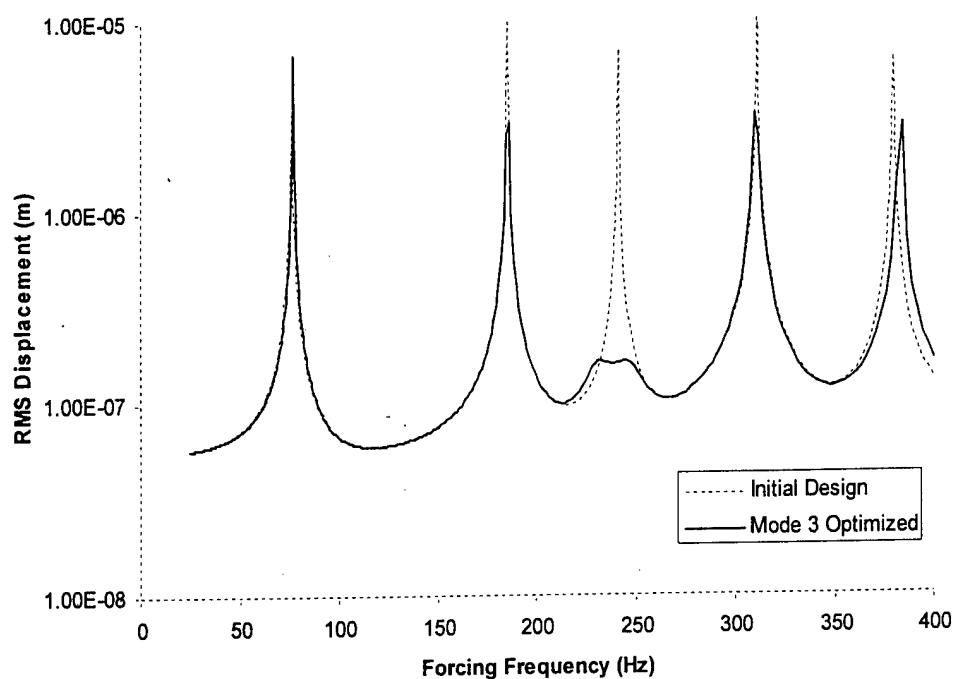


Fig. 6.5. Frequency response curve for the optimal passive damping design using mode 3.

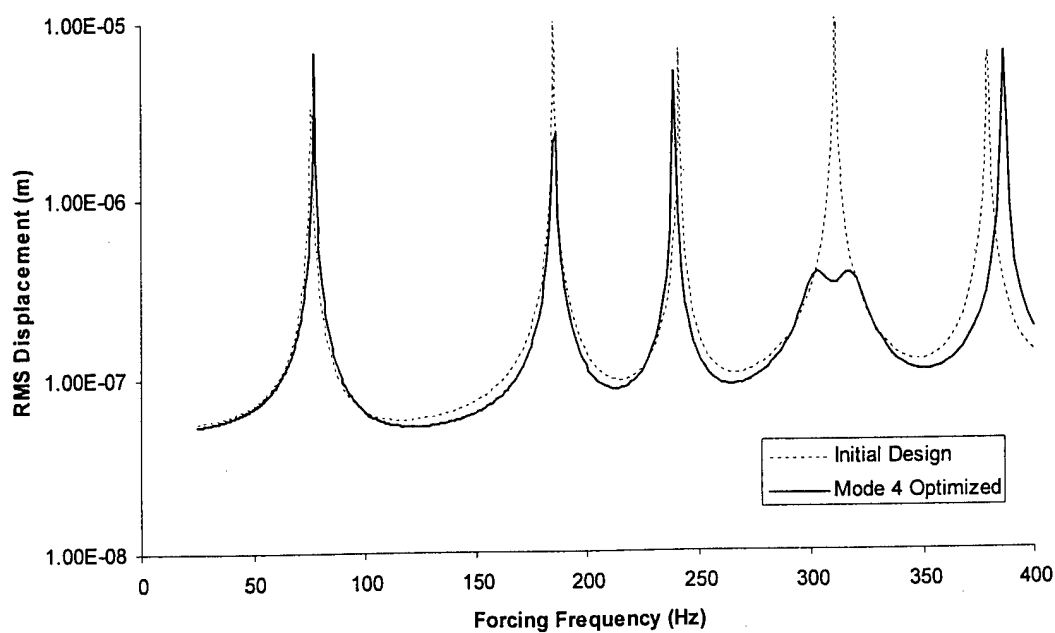


Fig. 6.6. Frequency response curve for the optimal passive damping design using mode 4.

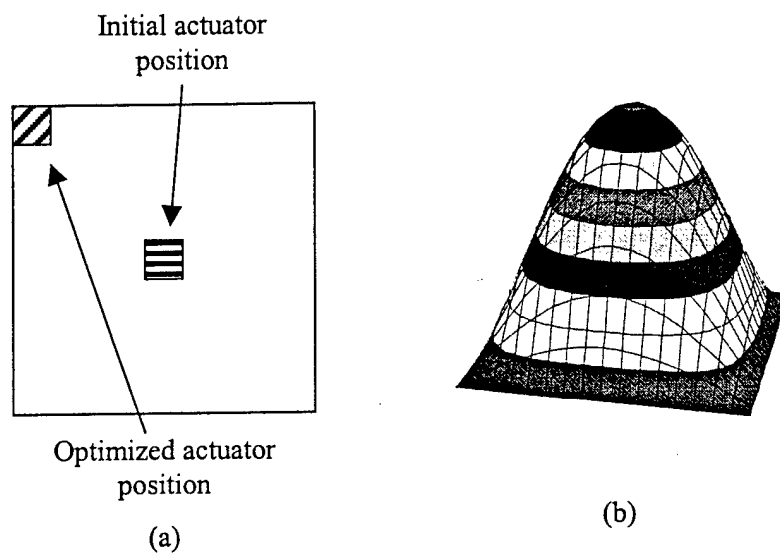


Fig. 6.7. Optimized actuator location, (a), for passive damping of the first vibration mode, (b).

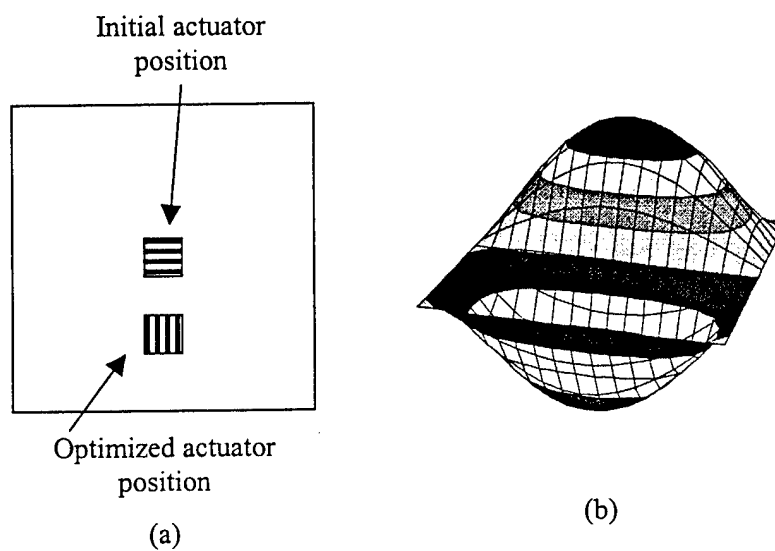
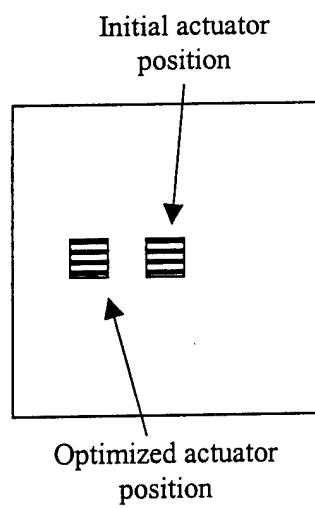
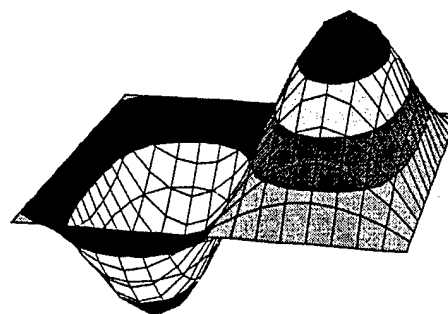


Fig. 6.8. Optimized actuator location, (a), for passive damping of the second vibration mode, (b).

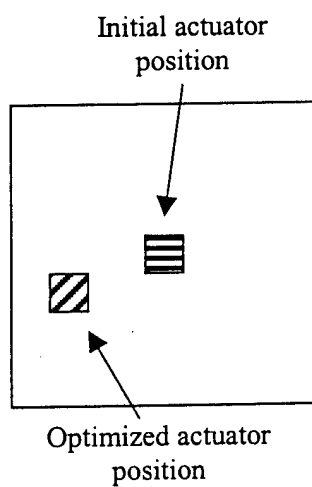


(a)

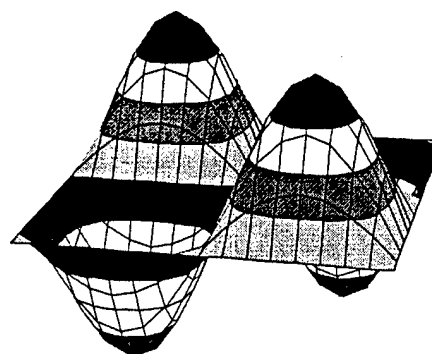


(b)

Fig. 6.9. Optimized actuator location, (a), for passive damping of the third vibration mode, (b).



(a)



(b)

Fig. 6.10. Optimized actuator location, (a), for passive damping of the fourth vibration mode, (b).

The optimum orientation angles of the AFC, for each case studied, are different. This is because, in each case, the piezoelectric fibers of the AFC actuators align with the direction of maximum strain. The results obtained demonstrate the benefit of including both structural and electrical parameters simultaneously in the optimization procedure. In the numerical examples shown, optimal designs are obtained by not only varying the parameters of the passive shunt circuit, but by also tailoring the mechanical stiffness of the piezoelectric patch. The location of the piezoelectric patch not only affects the passive damping capability, it also changes the dynamic response of the system causing natural frequencies to shift. This may or may not be desirable for a particular problem. In such cases the natural frequencies can be included as additional objective functions using the K-S function approach.

Next the same plate is optimized with two 2cmx4cm AFC actuators. Each actuator is connected to a single parallel shunt circuit. In this example the objective is the minimization of the first three vibrational modes. This method is very different from the multi-mode damping circuit proposed by Wu (1998) which uses three different circuits connected to a single

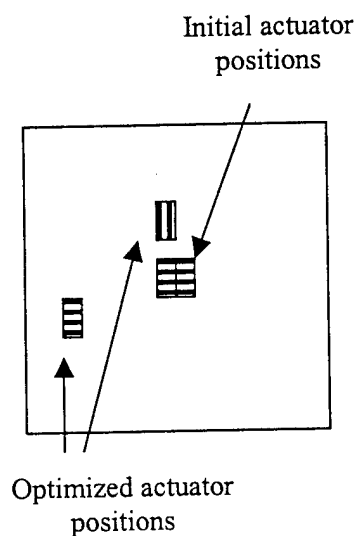


Fig. 6.11. Position of the actuators on the simply supported plate before and after optimization for two actuators and three modes.

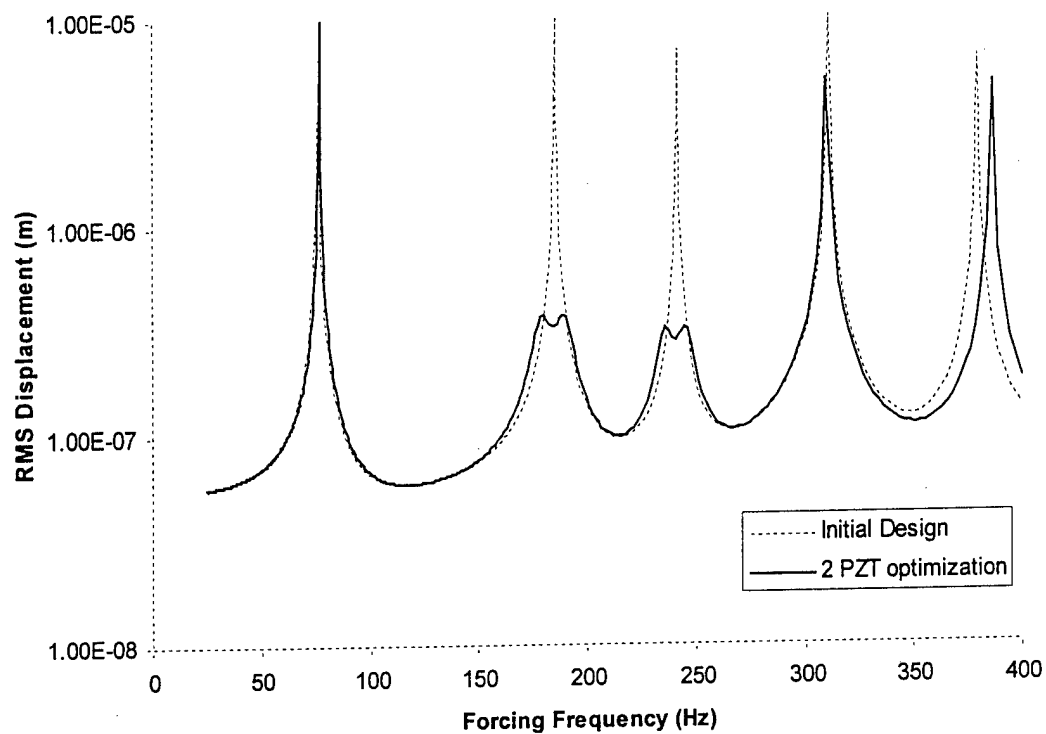


Fig. 6.12. Frequency response curves for a simply supported plate both undamped and with two actuators.

piezoelectric actuator in order to damp the three modes. The method developed by Wu would be less effective in this case since the optimal locations for each mode are different and the use of a single actuator would require compromises in the placement on the plate. The optimized results of the circuit are shown in Figures 6.11 and 6.12. The piezoelectric patches move to locations corresponding to 5cmx12cm and 15cmx22cm, with orientations of 0° and 75° respectively, as seen in Figure 6.11. The inductor and resistor assume values of 24.2490 henries and 620624 ohms for the first actuator and 41.5787 henries and 531028 ohms for the second actuator, after optimization. The resulting frequency response curve is presented in Figure 6.12. It can be seen that this damping circuit affects only the second and third vibration modes. This is because circuits with a single inductor and a single resistor are effective over a narrow range of frequencies. Thus, in this case, two actuators with single circuits cannot damp out more than two

of the first three modes. The optimal values of the design variables also roughly correspond to the locations and angles predicted for the second and third modes presented in the single actuator case.

In the final case studied, the effect of composite tailoring is investigated by including the ply orientations of the plate as additional design variables. The same plate with two 2cmx4cm AFC actuators is considered. The composite laminae are allowed to be oriented at even multiples of 15° , but symmetry is enforced to reduce the number of design variables. Thus, only four additional design variables are introduced. The optimized results are shown in Figures 6.13 and 6.14. The piezoelectric patches move to locations corresponding to 15cmx10cm and 21cmx12cm, with orientations of 75° and 15° respectively, as seen in Figure 6.13. The inductor and resistor have values of 38.828 henries and 559984 ohms for the first actuator and 211.850 henries and 230981 ohms for the second actuator. The final ply lay-up for the composite laminate is $[-15^\circ, 75^\circ, 15^\circ, -15^\circ]_s$. The resulting frequency response curve is shown in Figure 6.14 along with the response curve for the initial cross-ply design. It can be seen that the

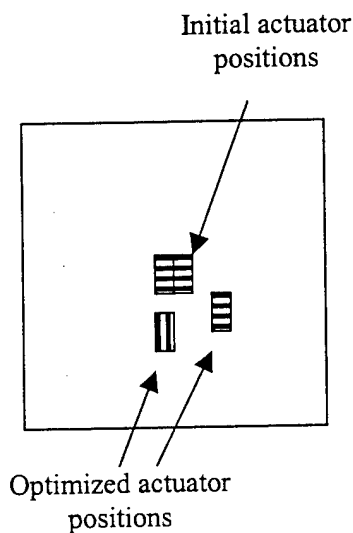


Fig. 6.13. Position of the actuators on the simply supported plate before and after optimization for two actuators and three modes, including optimization of ply orientation.

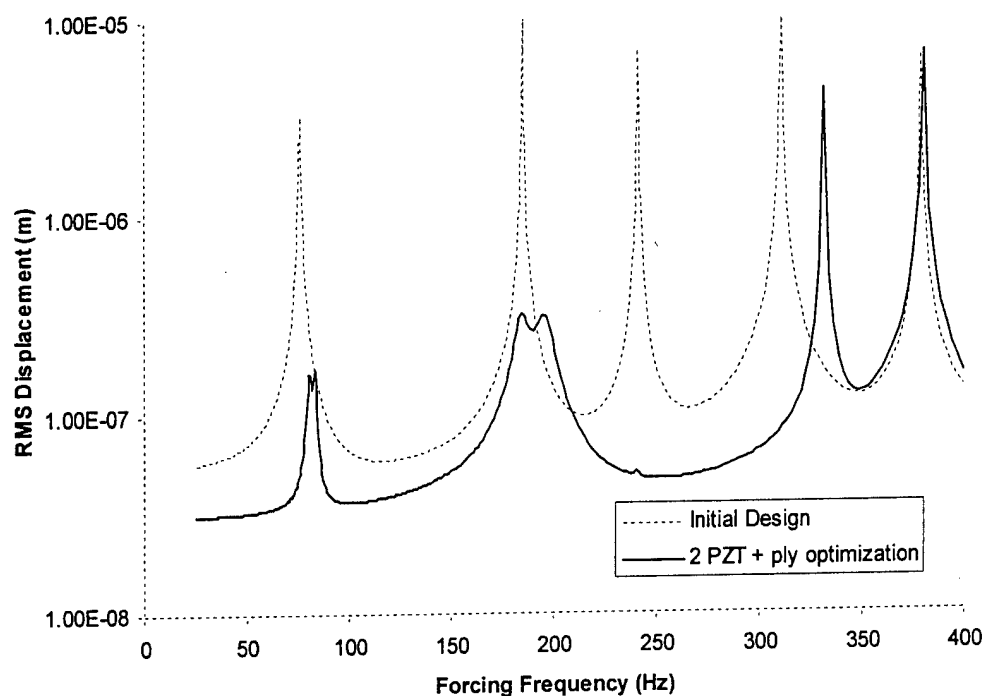


Fig. 6.14. Frequency response curves for the undamped initial design of a simply supported plate and the optimal design including two actuators and optimized ply orientations.

inclusion of the ply angles are effective in reducing the overall response across the frequency spectrum thus aiding the passive damping actuators which are effective at specific frequencies.

The numerical examples presented demonstrate the potential of using MDO techniques for designing integrated adaptive structural systems. For passive damping circuits, optimization determines best possible values of both structural and electrical components and can be used to design systems for damping of multiple modes. But greater value lies in the potential of designing systems with synergistic characteristics, where careful combinations of actuators and circuits provide significant damping with little or no power consumption. Also, this technique can model the behavior of real electrical components as opposed to the ideal components considered thus far. Factors, such as the internal resistance of inductors, can be included in the model without having to reformulate the optimization algorithm.

7. Concluding Remarks

A smart structural model has been developed to analytically determine the response of arbitrary structures with piezoelectric materials and attached electrical circuitry. The developed model includes the effects of composite damage in the form of delamination and matrix cracking. The mathematical model uses a coupled piezoelectric-mechanical theory that accurately captures both electrical and mechanical characteristics of adaptive structures. Parametric studies were performed to assess the difference in results predicted between the refined higher order laminate theory and the classical plate theory, as well as between the coupled and uncoupled piezoelectric models. The effect of matrix cracking is included as a reduction in laminate stiffness calculated using a separate finite element procedure. Delaminated plates are modeled as a collection of sublaminates and contact between the sublaminates is modeled using a discontinuous time integration method. A robust multi-objective optimization procedure was developed to optimally determine both the placement of piezoelectric actuators and parameters describing associated electrical components in a passively damped structure. The following conclusions were made from the present study

1. The developed finite element model gives accurate results for the response of adaptive composite laminates with piezoelectric devices.
2. The model is able to model the interaction between a structure and attached electrical circuitry, and good correlation is observed with experimental data for passive electrical damping circuits.
3. For thin plates, the differences in mechanical displacements predicted by the higher order and the classical plate theories are significant only when the time step is sufficiently small to capture very high frequency modes. The differences in sensor output are more significant in all cases.

4. For thicker plates, significant differences exist in both mechanical displacements and sensor output predicted by the higher order and the classical plate theories during all analyses.
5. The assumption of constant electric field over the entire PZT area in the uncoupled theory leads to inaccuracies in modeling the effect of high frequency vibrations that create both areas of local compression and local tension within the PZT patch.
6. The natural frequencies for the low frequency modes are, in general, accurately estimated using eigen values without contact effects. However, contact between the sublaminates becomes more important in the presence of higher frequency vibrations.
7. Delamination embedded closer to the midplane of the laminate shows greater affect on the natural frequencies, but is less affected by contact between the sublaminates.
8. The crack tip singularity of a delamination does not significantly affect the global response of the structure.
9. The method used to model matrix cracking is able to accurately predict the loss of stiffness for a variety of laminate materials and ply layups, based on good correlation with experimental data for the change in extensional and shear stiffness.
10. Matrix cracking introduces nonlinearity into a structure due to crack closure under compression. This effect can be modeled using techniques for bimodular materials.
11. The developed method is capable of optimizing passive damping parameters in various electrical configurations, as demonstrated by optimization of both parallel and series configurations.
12. The optimized locations of the piezoelectric actuators correspond to the locations of maximum strain for the mode being optimized, and the fibers of Active Fiber Composites are oriented so that the fibers are parallel to the principle strain.

REFERENCES

- Aboudi, J., 1987. Stiffness reduction of cracked solids. *Engineering Fracture Mechanics* 26(5), 637-650.
- Adolfsson, E., Gudmundson, P., 1995. Matrix crack induced stiffness reductions in $[0_m, 90_m, +\theta_p, -\theta_q]_s$ composite laminates. *Composite Engineering* 5(1), 107-123.
- Adolfsson, E., Gudmundson, P., 1997. Thermoplastic properties in combined bending and extension of thin composite laminates with transverse matrix cracks. *International Journal of Solids and Structures* 34 (16), 2035-2060.
- Agnes, G.S., 1994. Active/passive piezoelectric vibration suppression. *Proceedings of the International Society for Optical Engineering*, Vol. 2193, pp.24-34.
- Allen, D.H., Harris, C.E., Groves, S.E., 1987a. A thermomechanical constitutive theory for elastic composites with distributed damage - part I: theoretical development. *International Journal of Solids and Structures* 23(9), 1301-1318.
- Allen, D.H., Harris, C.E., Groves, S.E., 1987a. A thermomechanical constitutive theory for elastic composites with distributed damage - part II: application to matrix cracking in laminated composites. *International Journal of Solids and Structures* 23(9), 1319-1338.
- Allen, D.H., Harris, C.E., Groves, S.E., Norvell, R.G. 1988. Characterization of stiffness loss in crossply laminates with curved matrix cracks. *Journal of Composite Materials* 22, 71-80.
- Allen, D.H., Lee, J.W., 1990. Matrix cracking in laminated composites under monotonic and cyclic loadings. *ASME, AMD*, Vol. 111, pp. 65-75.
- Allen, D.H., Lo, D.C., 1991. A model for the progressive failure of laminated composite structural components. *Enhancing Analysis Techniques for Composite Materials*, ASME, Vol. 10, 125-131.
- Allen, D.H., Lo, D.C., Zocher, M.A., 1997. Modeling of damage evolution in laminated viscoelastic composites. *International Journal of Damage Mechanics* 6(1), 5-22.
- Anderson, E.H., Hagood, N.W., 1994. Simultaneous piezoelectric sensing/actuation: analysis and application to controlled structures. *Journal of Sound and Vibration* 174 (5), 617-639.
- Argyris, J., Mlejnek, H.P., 1991. *Dynamics of Structures. Text on Computational Mechanics*, V5, Elsevier Sci. Publishers.
- Barbero, E.J., Reddy, J.N., 1991. Modeling of delamination in composite laminates using a layer-wise plate theory. *International Journal of Solids and Structures* 28 (3), 373-388.
- Bathe, K.J., 1996. *Finite Element Procedures*. Prentice Hall, Englewood Cliffs, NJ.
- Belegundu, A.D., Chandrupatla, T.R., 1999. *Optimization concepts and applications in engineering*. Prentice Hall, Upper Saddle River, New Jersey.

- Bert, C.W., Reddy, J.N., Chao, W.C., Reddy, V.S., 1981. Vibration of thick rectangular plates of bimodulus composite material. *Journal of Applied Mechanics* 48, 371-376.
- Campanelli, R.W., Engblom, J.J., 1995. The effect of delaminations in graphite/PEEK composite plate on modal dynamic characteristics. *Composite Structures* 31, 195-202.
- Cao, A., Gabbert, U., Poetzsch, R., 1998. Delamination modeling and analysis of adaptive composites. *Proceedings of the 39th AIAA/ASME/ASCE/AHS/ASC Structures, Structural Dynamics and Materials Conference*, Vol. 4, pp. 2911-2916.
- Chatterjee, S.N., Ramnath, V., 1988. Modeling laminated composite structures as assemblage of sublaminae. *International Journal of Solids and Structures* 24 (5), 439-458.
- Chattopadhyay, A., Gu, H., 1994. New higher order plate theory in modeling delamination buckling of composite laminates. *AIAA Journal* 32 (8), 1709-1718.
- Chattopadhyay, A., Gu, H., 1997. Three-dimensional elasticity approach for delamination buckling of composite plates. *Proceedings of 38th AIAA/ASME/ASCE/AHS/ASC Structures, Structural Dynamics and Materials Conference*, Vol. 4, 2629-2638.
- Chattopadhyay, A., Gu, H., 1999. An experimental investigation of delamination buckling and postbuckling of composite laminates. *Composites Science and Technology* 59, 903-910.
- Chattopadhyay, A., Li, J., Gu, H., 1999. A coupled thermo-piezoelectric-mechanical model for smart composite laminates. *AIAA Journal* 37 (12), 1633-1638.
- Chattopadhyay, A., Nam, C., Dragomir-Daescu, D., 1999. Delamination modeling and detection in smart composite plates. *Journal of Reinforced Plastics and Composites* 18 (17), 1557-1572.
- Chattopadhyay, A., Dragomir-Daescu, D., Gu, H., 1999. Dynamics of delaminated smart composite cross-ply beams. *Smart Materials and Structures* 8, 92-99.
- Chattopadhyay, A., Gu, H., Liu, Q., 1999. Modeling of smart composite box beams with nonlinear induced strain. *Composites: Part B* 30 (6), 603-612.
- Chattopadhyay, A., Seeley, C.E., 1997. A higher order theory for modeling composite laminates with induced strain actuators. *Composites: Part B Engineering* 28B(3), 243-252.
- Chen, H.P., Tracy, J.J., Nonato, R., 1995. Vibration analysis of delaminated composite laminates in prebuckled states based on a new constrained model. *Journal of Composite Materials* 29 (2), 229-256.
- Cho, J.Y., Kim, S.J., 1999a. Discontinuous time-integration method for dynamic contact/impact problems. *AIAA Journal* 37 (7), 874-880.
- Cho, J.Y., Kim, S.J., 1999b. An explicit solution procedure of discontinuous time integration method for dynamic contact/impact problems. *Proceedings of the 40th AIAA/ASME/ASCE/AHS/ASC Structures, Structural Dynamics and Materials Conference*, Vol. 1, pp. 428-438.

- Cho, M., Parmerter, R.R., 1993. Efficient higher order composite plate theory for general lamination configurations. *AIAA Journal* 31 (7), 1299-1306.
- Cook, R.D., Malkus, D.S., Plesha, M.E., 1989. Concepts and applications of finite element analysis. 3rd Edition, John Wiley, NY.
- Crawley, E.F., de Luis, J., 1987. Use of piezoelectric actuators as elements of intelligent structures. *AIAA Journal* 25 (10), 1373-1385.
- Crawley, E.F., Anderson, E., 1989. Detailed models of piezoceramic actuation of beams. Proceedings of the 30th AIAA/ASME/ASCE/AHS/ASC Structures, Structural Dynamics and Materials Conference, pp. 2000-2010.
- Crawley, E.F., Lazarus, K.B., 1991. Induced strain actuation of isotropic and anisotropic plates. *AIAA Journal* 29 (6), 944-951.
- Detwiler, D.T., Shen, M.H., Venkayya, V.B., 1995. Finite element analysis of laminated composite structures containing distributed piezoelectric actuators and sensors. *Finite Elements in Analysis and Design* 20 (2), 87-100.
- Dvorak, G.J., 1985. Analysis of progressive matrix cracking in composite laminates. AFOSR-82-0308, Rensselaer Polytechnic Institute.
- Grady, J.E., Meyn, E.H., 1989. Vibration testing of impact damaged composite laminates. Proceedings of the 30th AIAA/ASME/ASCE/AHS/ASC Structures, Structural Dynamics and Materials Conference, pp. 2186-2193.
- Groves, S.E., 1986. A study of damage mechanics in continuous fiber composite laminates with matrix cracking and interply delaminations. Ph.D. Dissertation, Aerospace Engineering Dept., Texas A&M University, College Station, Texas 77843.
- Gudmundson, P., Zang, W., 1993. An analytical model for thermoplastic properties of composite laminates containing transverse matrix cracks. *International Journal of Solids and Structures* 30 (23), 3211-3231.
- Hagood, N.W., Chung, W.H., Flotow, A.V., 1990. Modeling of piezoelectric actuator dynamics for active structural control. Proceedings of the 31st AIAA/ASME/ASCE/AHS/ASC Structures, Structural Dynamics and Materials Conference, Vol. 4, 2242-2256.
- Hagood, N.W., Crawley, E.F., 1991. Experimental investigation of passive enhancement of damping for space structures. *Journal of Guidance, Control and Dynamics* 14 (6), 1100-1109.
- Hagood, N.W., Flotow, A.V., 1991. Damping of structural vibrations with piezoelectric materials and passive electrical networks. *Journal of Sound and Vibration* 146 (2), 243-268.
- Hashin, Z., 1985. Analysis of cracked laminates: a variational approach. *Mechanics of Materials* 4, North Holland, 121-136.

- Hashin, Z., 1986. Analysis of stiffness reduction of cracked cross-ply laminates. *Engineering Fracture Mechanics* 25 (5/6), 771-778.
- Hashin, Z., 1987. Analysis of orthogonally cracked laminates under tension. *Journal of Applied Mechanics* 54, 872-879.
- Herakovitch, C.T., Aboudi, J., Lee, S.W., Strauss, E.A., 1988. Damage in composite laminates: effects of transverse cracks. *Mechanics of Materials* 7, 91-107.
- Highsmith, A.L., Stinchcomb, W.W., Reifsnider, K.L., 1981. Stiffness reduction resulting from transverse matrix cracking in fiber-reinforced composite laminates. ESM Dept. Report, VPI & State University.
- Highsmith, A.L., Reifsnider, K.L., 1982. Stiffness reduction mechanisms in composite laminates. *Damage in Composite Materials ASTM STP 775*, K.L. Reifsnider Ed., American Society for Testing and Materials, pp.103-117.
- Hou, J.P., Jeronimidis, G., 1999. Vibration of delaminated thin composite plates. *Composites: Part A* 30, 989-995.
- Hughes, T.J.R., Taylor, R.L., Sackman, J.L., Curnier, A., Kanoknukulchai, W., 1976. A finite element method for a class of contact-impact problems. *Computer Methods in Applied Mechanics and Engineering* 8(3), 249-276.
- IEEE, 1987. IEEE standard on piezoelectricity. ANSI / IEEE Std 176-1987, The Institute of Electrical and Electronics Engineers, Inc., New York, New York.
- Ju, F., Lee, H.P., Lee, K.H., 1994. Free-vibration analysis of composite beams with multiple delaminations. *Composites Engineering* 4 (7), 715-730.
- Kahn, S.P., Wang, K.W., 1994. Structural vibration controls via piezoelectric materials with active-passive hybrid networks. *Proceedings of the ASME IMECE*, DE-75, pp.187-194.
- Kardomateas, G.A., Schmueser, D.W., 1988. Buckling and postbuckling of delaminated composites under compressive loads including transverse shear effects. *AIAA Journal* 26 (3), 337-343.
- Kim, T., Atluri, S.N., Loewy, R.G., 1998. Modeling of microcrack damaged composite plates undergoing nonlinear bimodular flutter oscillations. *AIAA Journal* 36(4), 598-606.
- Kwon, Y.W., Aygunes, H., 1996. Dynamic finite element analysis of laminated beams with delamination cracks using contact-impact conditions. *Computers and Structures* 58 (6), 1161-1169.
- Laws, N., Dvorak, G.J., Hejazi, M., 1983. Stiffness changes in unidirectional composites caused by crack systems. *Mechanics of Materials* 2, North Holland, 123-137.
- Lee, B.T., Sun, C.T., Liu, D., 1987, An assessment of damping measurement in the evaluation of integrity of composite beams. *Journal of Reinforced Plastics and Composites* 6, 114-125.

- Lee, C.K., 1990. Theory of laminated piezoelectric plates for the design of distributed sensors/actuators. Part I: governing equations and reciprocal relationships. *Journal of the Acoustical Society of America* 87 (3), 1144-1158.
- Lee, J.W., Allen, D.H., 1989. Internal state variable approach for predicting stiffness reductions in fibrous laminated composites with matrix cracks. *Journal of Composite Materials* 23(12), 1273-1291.
- Lee, J.W., Allen, D.H., Harris, C.E., 1991. The upper bounds of reduced axial and shear moduli in cross-ply laminates with matrix cracks. *Composite Materials: Fatigue and Fracture*, ASTM Vol. 1110, 56-69.
- Lee, K., 1994. A numerical solution for dynamic contact problems satisfying the velocity and acceleration compatibilities on the contact surface. *Computational Mechanics* 15, 189-200.
- Lim S.G., Hong, C.H., 1989. Prediction of transverse cracking and stiffness reduction in cross-ply laminated composites. *Journal of Composite Materials* 23, 695-713.
- Lu, X., Lestari, W., Hanagud, S., 2001. Nonlinear vibrations of a delaminated beam. *Journal of Vibration and Control* 7 (6), 803-831.
- McCarthy, T. R and Chattopadhyay, A. 1997. A refined higher order composite box beam theory. *Composites Part B: Engineering* 28B, 523-534.
- Makins, R.K., Adali, S., 1991. Bending of cross-ply delaminated plates with matrix cracks. *Journal of Strain Analysis for Engineering Design* 26 (4), 253-257.
- Mitchell, J.A., Reddy, J.N., 1995. A refined hybrid plate theory for composite laminates with piezoelectric laminae. *International Journal of Solids Structure* 32 (16), 2345-2367.
- Mujumdar, P.M., Suryanarayan, S., 1988. Flexural vibrations of beams with delaminations. *Journal of Sound and Vibration* 125 (3), 441-461.
- Park, C., Wlaz, C., Chopra, I., 1996. Bending and torsion models of beams with induced-strain actuators. *Smart Materials and Structures* 5 (1), 98-113.
- Pavier, M.J., Clarke, M.P., 1996. A specialized composite plate element for problems of delamination buckling and growth. *Composite Structures* 35, 45-53.
- Point, N., Sacco, E., 1996. A delamination model For laminated composites. *International Journal of Solids and Structures* 33 (4), 483-509.
- Radu, A.G., Chattopadhyay, A., 2000. Stability of delaminated composite plates using a higher order theory. *Proceedings of the 41st AIAA/ASME/ASCE Structures, Structural Dynamics and Materials Conference*, Vol. 1, pp.519-528.
- Rajadas, J.N., Jury, R.A., Chattopadhyay, A., 2000. Enhanced multiobjective optimization technique for multidisciplinary design. *Engineering Optimization* 33, 113-133.

- Ramkumar, R.L., Kulkarni, S.V., Pipes, R.B., 1979. Free vibration frequencies of a delaminated beam. Proceedings of the 34th Annual Technical Conference, Reinforced Composites Institute, Society of Plastics Industry Inc., Sec. 22-E, pp. 1-5.
- Reddy, J.N., 1982. Transient response of laminated, bimodular-material, composite rectangular plates. *Journal of Composite Materials* 16, 139-152.
- Reddy, J.N., 1984a. A simple higher-order theory for laminated composite plates. *Journal of Applied Mechanics* 51, 745-5.
- Reddy, J.N., 1984b. *Energy and Variational Methods in Applied Mechanics*. John Wiley and Sons Inc., New York.
- Reddy, J.N., 1997. *Mechanics of Laminated Composite Plates: Theory and Analysis*. Boca Raton, Florida, CRC Press.
- Richard, C., Guyomar, D., Audigier, D., Ching, G., 1999. Semi-passive damping using continuous switching of a piezoelectric device. Proceedings of the International Society for Optical Engineering, Vol. 3672, pp.104-11.
- Rodgers, J.P., Bent, A.A., Hagood, N.W., 1996. Characterization of interdigitated electrode piezoelectric fiber composites under high electrical and mechanical loading. Proceedings of the International Society for Optical Engineering, Vol. 2717, pp.642-59.
- Saravanos, D.A., Hopkins, D.A., 1996. The effects of delaminations on the damped dynamic characteristics of composite laminates: analysis and experiments. *Journal of Sound and Vibration* 192 (5), 977-993.
- Seeley, C.E., Chattopadhyay, A., Brei, D., 1996. Development of a polymeric piezoelectric C-block actuator using a hybrid optimization procedure. *AIAA Journal* 34 (1), 123-128.
- Sethi, S.S., Striz, A.G., 1997. On using the kreisselmeier-steinhauser function in simultaneous analysis and design. Proceedings of the 38th AIAA/ASME/ASCE Structures, Structural Dynamics and Materials Conference, pp.1357-1365.
- Shen, M.H.H., Grady, J.E., 1992. Free vibrations of delaminated beams. *AIAA Journal* 30 (5), 1361-1370.
- Smith, P.A., Wood, J.R., 1990. Poisson's ratio as a damage parameter in the static tensile loading of simple cross-ply laminates. *Composite Science and Technology* 38, 85-93.
- Smith, P.A., Ogin, S.L., 1999. On transverse matrix cracking in cross-ply laminates loaded in simple bending. *Composites: Part A* 30 (8), 1003-1008.
- Srinivas, S., Rao, C.V.J., Rao A.K., 1970. Some results from an exact analysis of thick laminates in vibration and buckling. *Journal of Applied Mechanics* 37 (3), 868-870.
- Talreja, R., 1985. Transverse cracking and stiffness reduction in composite laminates. *Journal of Composite Materials* 19, 355-375.

- Talreja, R., 1986. Stiffness properties of composite laminates with matrix cracking and interior delamination. *Engineering Fracture Mechanics* 25(5/6), 751-762.
- Talreja, R., 1989. Damage development in composites: mechanisms and modeling. *Journal of Strain Analysis* 24(4), 215-222.
- Talreja, R., Yalvac, S., Yats, L.D., Wetters, D.G., 1992. Transverse cracking and stiffness reduction in cross-ply laminates of different matrix toughness. *Journal of Composite Materials* 26(11), 1644-1663.
- Thornburgh, R.P., Chattopadhyay, A., 2001. Electrical-mechanical coupling effects on the dynamic response of smart composite structures. *Proceedings of the International Society for Optical Engineering*, Vol. 4327, pp. 413-424.
- Tiersten, H.F., 1967. Hamilton's principle for linear piezoelectric media. *IEEE Proceedings* 55 (8), 1523-1524.
- Tiersten, H.F., 1969. *Linear Piezoelectric Plate Vibrations*. Plenum, New York.
- Tiersten, H.F., 1993. Electroelastic equations for electroded thin plates subject to large driving voltages. *Journal of Applied Physics* 74 (5), 3389-3393.
- Tracy, J.J., Pardo, G.C., 1989. Effect of delamination on the natural frequencies of composite laminates. *Journal of Composite Materials* 23, 1200-1215.
- Tsai, C.-L., Daniel, I.M., 1992. The behavior of cracked cross-ply composite laminates under shear loading. *International Journal of Solids and Structures* 29 (24), 3251-3267.
- Tsai, M.S., Wang, K.W., 1996. Control of a ring structure with multiple active-passive hybrid networks. *Journal of Smart Materials and Structures* 5, 695-703.
- Tsai, M.S., Wang, K.W., 1999. On the structural damping characteristics of active piezoelectric actuators with passive shunt. *Journal of Sound and Vibration* 221 (1), 1-22.
- Tseng, Y.P., Bai, K.P., 1993. Bending analysis of bimodular laminates using a higher-order plate theory with the finite element technique. *Computers and Structures* 47 (3), 487-494.
- Vakulenko, A.A., Kachanov, M.L., 1971. Continuum theory of a medium with cracks. *Izv. AN SSSR, Mekhanika Tverdogo Tela* 6, 159-166.
- Wang, B.T., Rogers, C.A., 1991. Laminate plate theory for spatially distributed induced strain actuators. *Journal of Composite Materials* 25 (4), 433-452.
- Wang, J.T.-S., Liu, Y.Y., Gibby, J.A., 1982. Vibration of split beams. *Journal of Sound and Vibration* 84 (4), 491-502.
- Wang, J.T.-S., Lin, C.-C., 1995. Vibration of beam-plates having multiple delaminations. *Proceedings of AIAA/ASME/ASCE/AHS/ASC 36th Structures, Structural Dynamics, and Materials Conference*, Vol. 5, pp. 3126-3133.

- Williams, T.O., Addessio, F.L., 1997. A general theory for laminated plates with delaminations. *International Journal of Solids and Structures* 34 (16), 2003-2024.
- Williams, T.O., Addessio, F.L., 1998. A dynamics model for laminated plates with delaminations. *International Journal of Solids and Structures* 35 (1-2), 83-106.
- Wrenn, G.A., 1989. An indirect method for numerical optimization using the Kreisselmeier-Steinhauser function. NASA Contractor Report 4220.
- Wu, J.S., Jing, H.S., Cheng, C.R., 1989. Free-vibration analysis of single-layer and two-layer bimodular beams. *International Journal for Numerical Methods in Engineering* 28, 955-965.
- Wu, S.Y., 1996. Piezoelectric shunts with a parallel R-L circuit for structural damping and vibration control. *Proceedings of the International Society for Optical Engineering*, Vol. 2720, pp.259-69.
- Wu, S.Y., Bicos, A.S., 1997. Structural vibration damping experiments using improved piezoelectric shunts. *Proceedings of the International Society for Optical Engineering*, Vol. 3045, pp.40-50.
- Wu, S.Y., 1998. Method for multiple mode shunt damping of structural vibration using a single PZT transducer. *Proceedings of the International Society for Optical Engineering*, Vol. 3327, pp.112-122.
- Yang, H.T.Y., He, C.C., 1994. Three-dimensional finite element analysis of free edge stresses and delamination of composite laminates. *Journal of Composite Materials* 28 (15), 1394-1412.
- Yeh, M.K., Fang, L.B., Kao, M.H., 1997. Bending behavior of delaminated composite plates with contact effects. *Composite Structures* 39 (3-4), 347-356.
- Yin, W.L., Jane, K.C., 1988. Vibration of a delaminated beam-plate relative to buckled states. *Proceedings of AIAA/ASME/ASCE/AHS/ASC 29th Structures, Structural Dynamics, and Materials Conference*, Vol. 2, pp. 860-870.
- Zak, A., Krawczuk, M., Ostachowicz, 2000. Numerical and experimental investigation of free vibration of multilayer delaminated composite beams and plates. *Computational Mechanics*. 26, 309-315.
- Zhou, X., Chattopadhyay, A., Gu, H., 2000. Dynamic response of smart composites using a coupled thermo-piezoelectric-mechanical model. *AIAA Journal* 38 (10), 1939-1948.